SEARCH FOR THE ONSET OF COLOR TRANSPARENCY THROUGH ρ^0 ELECTROPRODUCTION ON NUCLEI

BY

LORENZO ZANA

B.S. Physics, University of Turin (2002)

DISSERTATION

Submitted to the University of New Hampshire

in Partial Fulfillment of

the Requirements for the Degree of

Doctor of Philosophy

in

Physics

May, 2010

This dissertation has been examined and approved.

_____

Thesis Director, Maurik Holtrop

Associate Professor, Department of Physics

_____

John Calarco

Professor, Department of Physics

_____

John Dawson

Emeritus Professor, Department of Physics

_____

Hovanes Egiyan

Research Scientist, Department of Physics

_____

Richard Kaufmann

Emeritus Professor, Department of Physics

_____

Date

DEDICATION

To my present, past and future family.

ACKNOWLEDGMENTS

TABLE OF CONTENTS

LIST OF TABLES

LIST OF FIGURES

ABSTRACT

SEARCH FOR THE ONSET OF COLOR TRANSPARENCY
THROUGH ρ^0 ELECTROPRODUCTION ON NUCLEI

by

Lorenzo Zana

University of New Hampshire, May, 2010

Color Transparency is a QCD phenomenon which predicts a reduced level of interaction for reactions where the particle state is produced in a point-like configuration. In this talk I will present the analysis of the search for the onset of Color Transparency in ρ^0 electroproduction with the CLAS detector at Thomas Jefferson Laboratory. This experiment used two different targets simultaneously to reduce the systematic error and achieve a more precise measurement.The Nuclear Transparency was measured as a function of Q^2 and Coherence Length (l_c), and was found to be independent of the (l_c on the range scanned in the experiment. The increase in Nuclear Transparency observed with an increase in Q^2 signify the onset of the Color Transparency effect

Chapter 1

MOTIVATIONS

The nuclear transparency for the coherent production of ρ^0 mesons was measured on ^{2}H, ^{12}C and ^{56}Fe in the Q^2 range of 1.-2.5 GeV^2/c^2 with the Continuous Electron Beam Accelerator Facility [CLAS] detector at Jefferson Laboratory. The nuclear transparency is extracted for a number of bins in Q^2 as the ratio of ρ_0 production on a nuclear target over the production on deuterium. Systematic errors were reduced by measuring on these two targets simultaneously. A rise in the nuclear transparency for increasing Q^2 would indicate the onset of Color Transparency [CT]. We will discuss the theoretical background, the experimental setup, the data analysis and the outlook for this experiment.

In this chapter I will start giving a theoretical introduction to this experiment. First I will introduce the Glauber model, which interprets the interaction with matter using a hadronic description in quantum mechanics. Then I will present the Color Transparency concept as was firstly developed using perturbative Quantum ChromoDynamics [pQCD] and will show an example of how this description leads to a lower interaction of quark systems with nuclear matter. Consequently I will present two different models which attempts to translate the concept of Color Transparency in perturbative QCD to the case of lower energy. In the last section, I will briefly describe different experiments that have searched for the Color Transparency effect in nuclear matter.

1.1 Introduction

Twenty years of experiments have confirmed that perturbative QCD describes high momentum transfer reactions in nuclear physics accurately. From another view, processes such as

confinement, and the physics of spontaneously broken chiral symmetry, are yet to be understood. Studies of coherent phenomenas (to be distinguished from coherence length effects, as will be explained in detail later in this chapter) are important in order to understand confinement and spontaneously broken chiral symmetry. Here, the field theory properties of QCD play an important role in testing different ideas and models. For example, if one has an high momentum color neutral system of closely separated quarks and gluons produced in a collision, one can assume that this configuration will interact with the remaining nucleons target with the emission of long wavelengths gluons. The leading term of the interaction, which is like a "color monopole" term, will not give any contribution since the system is color neutral. The next to leading order contribution is given by a "color dipole" term. If the size of the system is small enough respect to the distance that characterizes the interaction with the nucleons, we can assume that also the dipole effects will be suppressed. The interaction will be defined in this case as "color screened" and the suppression of the "dipole" term will be called Color Transparency.

If the momentum is high enough, the configuration of this particular system of quarks and gluons, called a Point Like Configuration [PLC], will maintain its size through the nuclear target. At lower momentum this Point Like Configuration object will have sufficient time to evolve to its full hadron size. Experiments at this energies will be able to observe the process of formation of an hadron and the consequent mechanisms of restoration of color and pion fields.

In this experiment, we chose to use the rho-zero [ρ^0] vector meson in order study the evolution of a Point Like Configuration and Color Transparency. In a 1960s paper [20], Sakurai proposed that the photon interacts with nuclear matter through its hadronic fluctuations. This is now expressed with the vector meson dominant model, where the hadronic components of the photon consist of the lightest vector mesons, namely rho (ρ), omega (ω) and phi (ϕ). The process of creation of vector mesons through the fluctuation of a virtual photon in a $q\bar{q}$ system, as well as its size dependence on the mass of the virtual photon, are well understood (see [21]). The other advantage of studying the ρ^0 comes from theoretical

predictions which suggest that the effects of Color Transparency will become important at lower energies for a $q\,\bar{q}$ system, such as the ρ^0, compared to hadrons consisting of 3 quarks. This is simply due to the fact that quark-antiquark systems can be smaller in physical size than three quark systems at the same energy.

1.2 Notation and conventions

This document will use natural units:

$$\hbar = 1 \qquad c = 1$$

Two different metric will be used, focusing on the one that will give an easier interpretation of the physical behavior of the system. The theory chapter will mainly use Light Cone coordinates (see [22] and [23] for physical background) with the metric given by:

$$g^{\mu\nu} = \begin{pmatrix} 0 & 1 & 0 & 0 \\ 1 & 0 & 0 & 0 \\ 0 & 0 & -1 & 0 \\ 0 & 0 & 0 & -1 \end{pmatrix}$$

where

$$x^+ = \frac{x_0 + x_1}{\sqrt{2}} \ , \ x^- = \frac{x_0 - x_1}{\sqrt{2}}$$

and the coordinate x_2 and x_3 will be referred to as Transverse coordinate $\vec{x}_T$ to the light cone direction, given in this case by x_1. In the other section the more standard metric will be used

$$g^{\mu\nu} = \begin{pmatrix} 1 & & 0 & 0 \\ 0 & -1 & 0 & 0 \\ 0 & 0 & -1 & 0 \\ 0 & 0 & 0 & -1 \end{pmatrix}$$

The kinematic variables used for describing the reaction are (see figure 1-1):
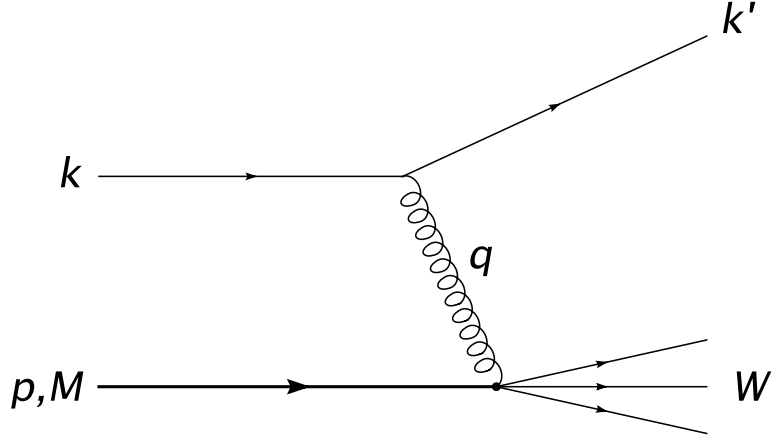
Figure 1-1: Kinematic quantities used in this analysis. k and k' describe the 4-momentum of the incoming and scattered electron, p and M are the momentum and Mass of the incoming nucleon and W is the mass of the recoiling system

- $Q^2 = -q^2$, momentum transfer squared

- $\nu = E_k - E_{k'}$ is the electron energy loss in the nucleon rest frame

- $W^2 = (p+q)^2$ is the mass squared of the system recoiling against the scattered electron

An important quantity used in the search of Color Transparency is the Nuclear Transparency T_A. It is measured by taking the ratio of the nuclear per-nucleon cross section (σ_A/A) with the free nucleon cross section (σ_N).

$$T_A \frac{\sigma_A}{A\,\sigma_N} \tag{1.1}$$

1.3 Theoretical Background

Color Transparency [24] could be considered as the effect of two distinct phenomena that select a particular configuration of the quark pair generated by the scattering process.

- The first selection is done by the kinematics of the reaction, that in our case will be driven by Q^2. This selection, as one can picture from considerations of Heisenberg's Principle, will choose quark configurations with a separation tuned by Q^2.

4

- From this ensemble of configurations, Nuclear filtering will select only the one configuration with small transverse distance between the quarks.

1.3.1 Glauber Model

For a better explaination of the theory of Color Transparency, I will start introducing the Glauber Model [25] that, starting from an hadronic picture, develops the description of the interaction with matter using collision theory from Quantum mechanics. If we start describing the asymptotic picture of scattering of an incoming particle with momentum $\vec{k}$ through a target situated for simplicity at $r = 0$, we can describe this system using a Schrodinger picture:

$$\psi(\vec{r}) \sim \overbrace{e^{i\vec{k}\cdot\vec{r}}}^{(a)} + \overbrace{f(\theta)\frac{e^{ikr}}{r}}^{(b)} \tag{1.2}$$

where in equation 1.2 (a) refers to the incoming particle, (b) is connected to the outgoing wave, scattered from the center of the axis and $f(\theta)$ is directly connected to the cross section of the interaction.

$$f(\theta) = f(\vec{k}, \vec{k'}) \sim \int e^{i(\vec{k}-\vec{k'})\cdot\vec{r}} V(\vec{r}) d\vec{r} \tag{1.3}$$

here $\vec{k}$ is the momentum of the incoming particle and $\vec{k'}$ is the scattered one. If one can assume cylindrical symmetry of the interacting potential over the axis of the incoming particle, the only dependence of $V(\vec{r})$ will be of the impact parameter $\vec{b}$ (see figure 1-3)which allows $f(\vec{k}, \vec{k'})$ to be expanded

$$f(\vec{k}, \vec{k'}) = \frac{ik}{2\pi} \int e^{i(\vec{k}-\vec{k'})\cdot\vec{b}} e^{i(\vec{k}-\vec{k'})\cdot\hat{z}z} \Gamma(\vec{b}) d^2b\, dz = \tag{1.4}$$

$$= -\frac{ik}{2\pi} \int e^{i(\vec{k}-\vec{k'})\cdot\vec{b}} e^{i(\vec{k}-\vec{k'})\cdot\hat{z}z} (e^{i\chi(\vec{b})} - 1) d^2b\, dz \tag{1.5}$$

Equations 1.4 and 1.5 define $\Gamma(\vec{b})$ and $\chi(\vec{b})$ which give 2 complementary descriptions of the interaction.

An important behavior of vector meson photoproduction, which can be interpreted using the Glauber model, is the Coherence Length effect. The next part of this section follows the study from Hufner et al. in Ref.[17]. In the study of photo-production of vector meson
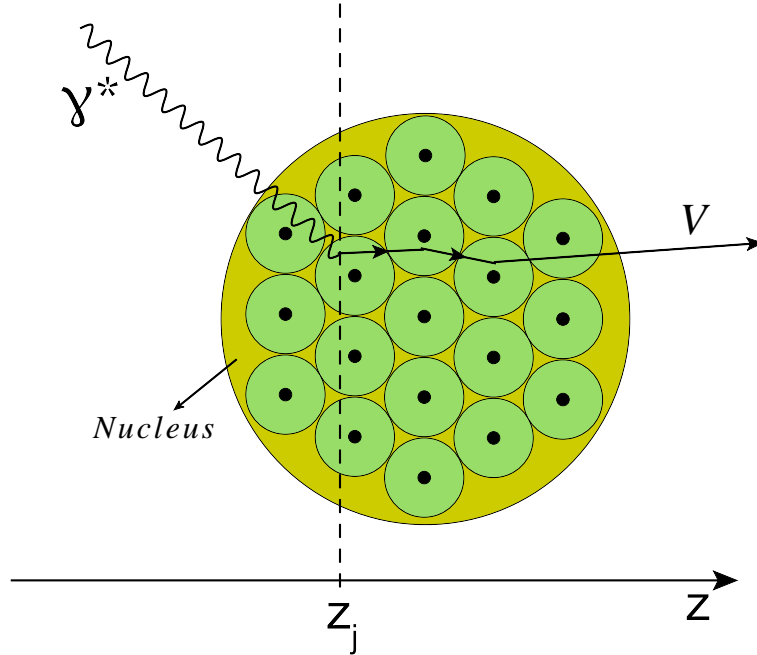
Figure 1-2: Schematic of Vector Meson photoproduction in an atom using the Glauber approximation. Highlighted is also the z coordinate respect to the symmetry axis.

V off nucleus A, schematically $\gamma^* A \to V X$, one can imagine the interaction on the target as the product of different combinations of:

1. vector meson photo-production on the nucleus

2. multiple elastic rescattering of the vector meson produced in step 1 with the other nuclei of the material

One condition of the Glauber model is the small cone of possible directions of the scattered particle respective to the incident beam's direction. Due to this requirement, the trajectory of the produced vector meson will not change direction significantly (will keep "moving forward"), giving a restriction to the possible combinations of elastic rescattering, depending on the place of photo-production in the atom, as shown in figure 1-3 . The vector meson photo-production amplitude of the incident γ^* on a nucleus A will be given in eikonal

6

Figure 1-3: Schematic of the interaction in an atom using the Glauber approximation: On red are outlined the region where the nuclei will contribute with elastic scattering depending on their local impact parameter; $\vec{b}$ will describe the transverse coordinate (respect to the symmetry axis z) of the incoming γ^* ; $\vec{s_j}$ will describe the transverse coordinate of the nucleus j; $(\vec{b} - \vec{s_j})$ will describe the impact parameter of the γ^* respect to the nucleus j

form as:

$$
\Gamma_A^{\gamma^* V}(\vec{b}) = \sum_{j=1}^{A} \overbrace{\Gamma_N^{\gamma^* V}(\vec{b} - \vec{s_j})}^{(a)} \overbrace{e^{i q_L z_j}}^{(b)} \overbrace{\prod_{k\,(\neq j)}^{A} \left[1 - \Gamma_N^{VV}(\vec{b} - \vec{s_k})\, \theta(z_k - z_j) \right]}^{(c)}
\tag{1.6}
$$

where (a) describes the vector meson photo-production amplitude and (c), if expanded, expresses all the possible combinations of elastic scattering in the region $z > z_j$. One of the key factors for interpreting the Coherence Length effect is the phase factor (b) . q_L represents the Longitudinal part (z direction) of the difference $(\vec{k} - \vec{k'})$ of the momenta of both the photon and of the vector meson:

$$
q_L = p^{\gamma^*} - p_L^V = \frac{Q^2 + M_V^2}{2\nu} \implies l_c = \frac{1}{q_L} = \frac{2\nu}{Q^2 + M_V^2}
\tag{1.7}
$$

The inverse of q_L represents the Coherence Length l_c , because in the sum of different terms in Equation 1.6, for the region where $(z_{j^1} - z_{j^2}) < l_c$ (where j^1 and j^2 represent two indices in the sum) the production amplitudes will add coherently. Otherwise there will be destructive interference. Considering that during the interaction the nuclear state will change from $|0>$, the ground state to $|f>$, the final state (different from the starting one), one can define

$$
\frac{d\sigma_{inc}^{\gamma^* V}}{d^2 p_T^V} = \left| \int \frac{d^2 b}{2\pi} e^{-i\vec{p_T^V}\cdot\vec{b}} \langle f | \Gamma_A^{\gamma^* V}(\vec{b}) | 0 \rangle \right|^2
\tag{1.8}
$$

Integrating over p_T^V and summing over the final states (where one will consider the completeness of the final states), one obtains

$$\sigma_{inc}^{\gamma^*V} = \int \frac{d^2 p_T^V}{2\pi} \int d^2 b \int d^2 b' e^{i \vec{p}_T^V (\vec{b} - \vec{b'})} \left(\langle 0| \Gamma_A^{\gamma^*V*}(\vec{b'}) \, \Gamma_A^{\gamma^*V}(\vec{b}) |0\rangle - \langle 0|\Gamma_A^{\gamma^*V*}(\vec{b'})|0\rangle \, \langle 0|\Gamma_A^{\gamma^*V}(\vec{b})|0\rangle \right)$$

(1.9)

where one uses the fact that in the final states the ground state is missing from the complete set of states. Using one of the representations of the delta function

$$\delta^2(\vec{b} - \vec{b'}) = \int \frac{d^2 p_T^V}{2\pi} e^{i \vec{p}_T^V (\vec{b} - \vec{b'})}$$

one can simplify the equation into

$$\sigma_{inc}^{\gamma^*V} = \int d^2 b \left[\langle 0| \left| \Gamma_A^{\gamma^*V}(\vec{b}) \right|^2 |0\rangle - \left| \langle 0|\Gamma_A^{\gamma^*V}(\vec{b})|0\rangle \right|^2 \right]$$

(1.10)

As is shown in [17] , different $q_L(Q^2)$ in Equation1.6 will lead to different contributions from the $\Gamma_A^{\gamma^*V}(\vec{b})$ to the cross section, thus creating a Q^2 dependence in the Glauber model as well (see figure 1-4) .

The Glauber model [25], which gives a Quantum mechanical description of the interaction with matter, does not mention whether the particles considered have a composite system of quarks. For this reason the Transparency factor will be independent of the Q^2 transferred by the incoming beam and its value will be constant if one subtract or otherwise controls the Q^2 dependence due to Coherence Length effects.

1.3.2 pQCD description of Color Transparency

In a hadron in high momentum transfer exclusive reactions, the fundamental part which controls the valence quarks is called quark distribution amplitude [26]. In free space exclusive processes we can express the distribution amplitude using in light cone coordinate:

$$\phi_0(x_i, Q^2) = \int^Q d^2 k_T \psi_0(x_i, \vec{k}_T^2)$$

(1.11)

where x_i is the fraction of the longitudinal momentum carried by the i-quark so that $(1 - x_i)p = |\vec{k}_T|$ (where p is the momentum of the quark). The next example will describe

8
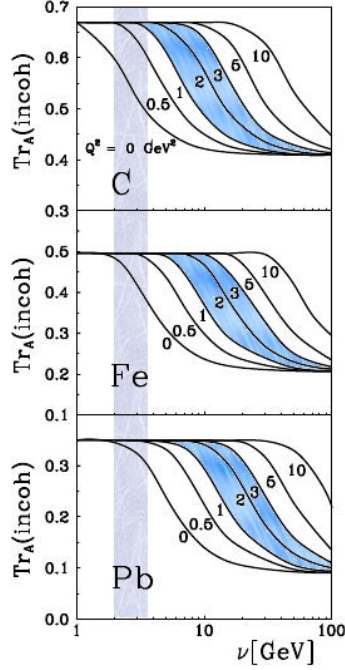
Figure 1-4: Nuclear Transparency as a function of Q^2 and ν for different target material. Highlighted in color is the kinematical region investigated by the EG2 experiment (see figure 1-5 on the right)
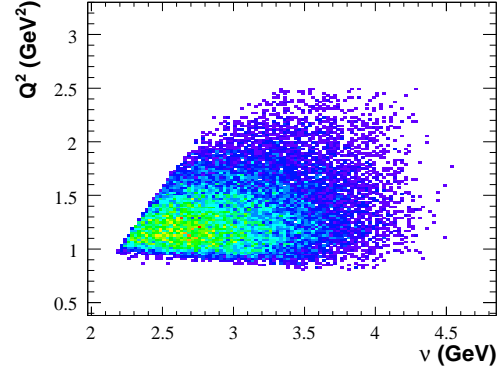
Figure 1-5: EG2 experiment kinematical range: $0.9 GeV^2 < Q^2 < 2 GeV^2$ and $2.2 GeV < \nu < 3.5 GeV$

how a pQCD analysis of CT can be done. We will consider the pion knockout reaction $\pi A \to \pi'\pi''A$ (see figure 1-6) (see Ref. [27]). This process describes some properties of CT well, and can be decomposed as the sum of a soft Collision (G) with an hard scattering kernel (H) (see figure 1-6 , part (a) and equation 1.12). The hard scattering part will be independent of the nuclear number A and of the location of the interaction inside the nuclei. The amplitude M is given by [27]

$$M = \int \prod_i dl_i \int \prod_j dk_j \, G(l_i, k_j) \, H(k_j, Q^2)$$

(1.12)

where

k_j = active parton momentum

l_i = loop momentum interaction with the participating quark spectators.

9

The first step is normally defined as "factorization". In this stage we separate the soft and the initial part of the interaction from $H(k_j, Q^2)$. The distribution amplitude of an hadron that has interacted with a nucleus A (in the following I will refer to wave functions which describe hadrons that have interacted with a nucleus with a label A, characteristic of the nucleus) will be given by [27]:

$$\phi_A(x, Q^2) = \int^Q d^2 k_T \psi_A(x, \vec{k}_T^2) \tag{1.13}$$

Using this formalism we can rewrite the expression of M as

$$M = \int \prod_j dk_j \, H(k_j, Q^2) \, \psi_A(k_1) \psi_A(k_2) \psi_A(k') \psi_A(k'') \tag{1.14}$$

This transformation in M is shown schematically with the passage from diagram (a) to diagram (b) in figure 1-6. In part (b) of this picture the S blobs represent soft interactions between the hadrons. These will be suppressed with respect to the other interactions, because they will be the product of the coupling of these hadrons, which are color singlets.

Anti-transforming in $\vec{k}_T$ the quantity ψ_A in Eq1.13 , we can express it as a function of the impact parameter $\vec{b}_T$

$$\int d^2 k_T \, \psi_A(x, \vec{k}_T^2) e^{-i \vec{b}_T \cdot \vec{k}_T} = \tilde{\psi}_A(x, \vec{b}_T^2) = \tilde{\psi}_A(x, b) = \tilde{f}_A(s, b^2) \, \tilde{\psi}_0(x, b) \tag{1.15}$$

where $\sim$ denotes the function in coordinate space and $\tilde{f}_A(s, b^2)$ is the nuclear filtering amplitude for an interacting quark in target A of energy s and impact parameter b

$$\tilde{f}_A = 1 - \tilde{F}_A \qquad \text{(where } \tilde{F}_A \text{ is the scattering amplitude)} \tag{1.16}$$

Thus the transmitted wave is the original wave minus the scattered wave. We now have for Eq1.13

$$\phi_A(x, Q^2) = \int^Q d^2 k_T \int d^2 b_T \, e^{i \vec{b}_T \cdot \vec{k}_T} \tilde{f}_A(s, b^2) \tilde{\psi}_0(x, b) =$$
$$= (2\pi)^2 Q \int_0^\infty db \, J_1(Qb) \tilde{f}_A(s, b^2) \tilde{\psi}_0(x, b) \tag{1.17}$$

10
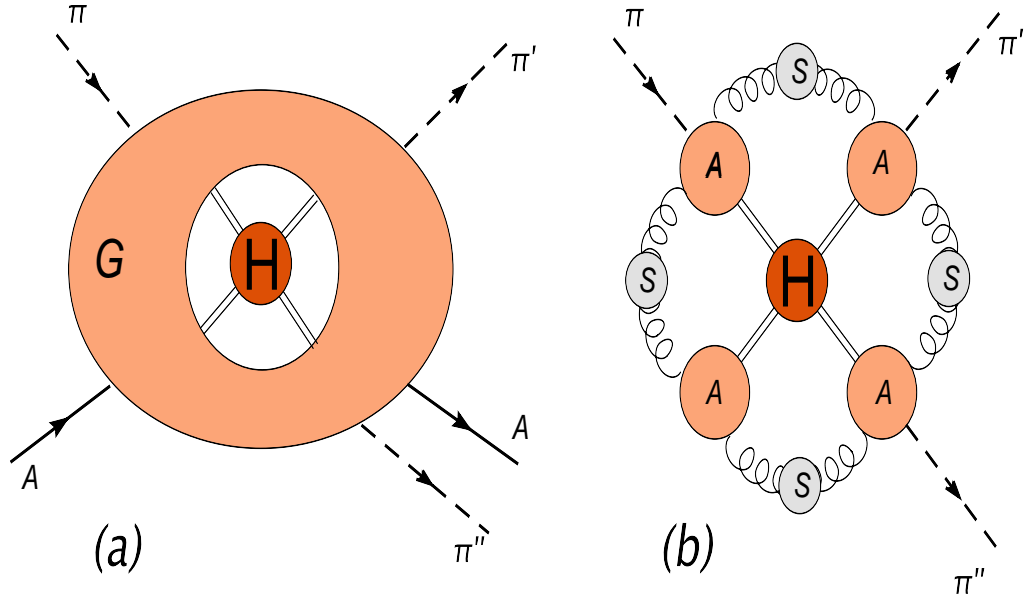
Figure 1-6: Reaction under study.

Where we have used the cylindrical symmetry around $\vec{b}_T$ and $\vec{k}_T$ and the definition of the integral representation of the Bessel function.

$$J_0(z) = \frac{1}{2\pi} \int_0^{2\pi} e^{iz\cos\theta} d\theta \quad ; \quad \int_0^u z\, J_0(z) dz = u\, J_1(u) \qquad (1.18)$$

The full Q dependence of this formula is given by the term $QJ_1(Qb)$, that comes only from imposing the upper limit on $\vec{k}_T$. The behavior of this function is shown in figure 1-7 . The nuclear dependence of the reaction is now entirely carried by $\tilde{f}_A(s, b^2)$. Even assuming a complicated functional behavior, that will depend on the model considered, we can still expand $\tilde{f}_A(s, b^2)$ around a known value of b. Because at $b = 0$ the color dipole moment of the singlet mini-hadron will be null, it is assumed that

$$\tilde{f}_A(s, b^2)\Big|_{b=0} = 1 \quad \Rightarrow \quad \tilde{f}_A(s, b^2) \sim 1 - A^{1/3} n b^2 \sigma'_{eff} + ... \qquad (1.19)$$

where $b^2 \sigma'_{eff}$, by definition, is the effective cross section and n is the average nuclear density. Due to the selection driven by higher Q values (see figure 1-7) the only part that will count
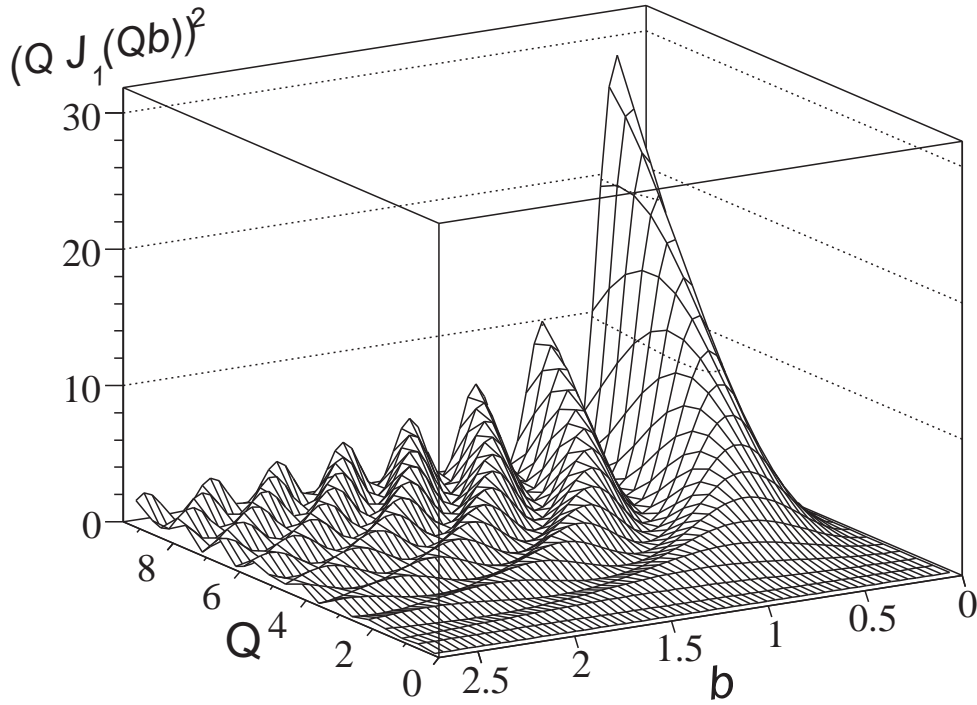
Figure 1-7: The dependence of $|\phi_A|^2$ with respect to Q and b is proportional to $(QJ_1(Qb))^2$ (here plotted). High Q will select configuration of the wave function of the quark $\tilde{\psi}_0(x,b)$ which will be characterized by low b

of $\tilde{f}_A(s,b^2)$ will be the one at $b \to 0$. So for high enough values of Q we can directly see how we can "turn off" the soft part of the interaction. Not considering normalization factors,

$$\lim_{Q \to \infty} \phi_A(x,Q^2) = \int^Q d^2k_T \psi_A(x,\vec{k}_T^2) = \phi_0(x,Q^2) \tag{1.20}$$

The distribution amplitude of an hadron which has interacted with a nucleus $\phi_A(x,Q^2)$ for high enough Q is the same one as in free space. The only ingredients for finding this result (which states that for high enough Q^2 the nuclear medium has no action on the wave particle) were:

- factorization,

- including filtering in the nucleus,

- Imposing cylindrical symmetry around $\vec{k}_T \Leftrightarrow \vec{b}_T$.

From figure 1-7 is also possible to understand the concept of nuclear filtering: The interaction favors high Q^2, selecting quark's configurations characterized by small transverse separation. Short distance is then a statement about a dominant integration region.

Easy interaction model
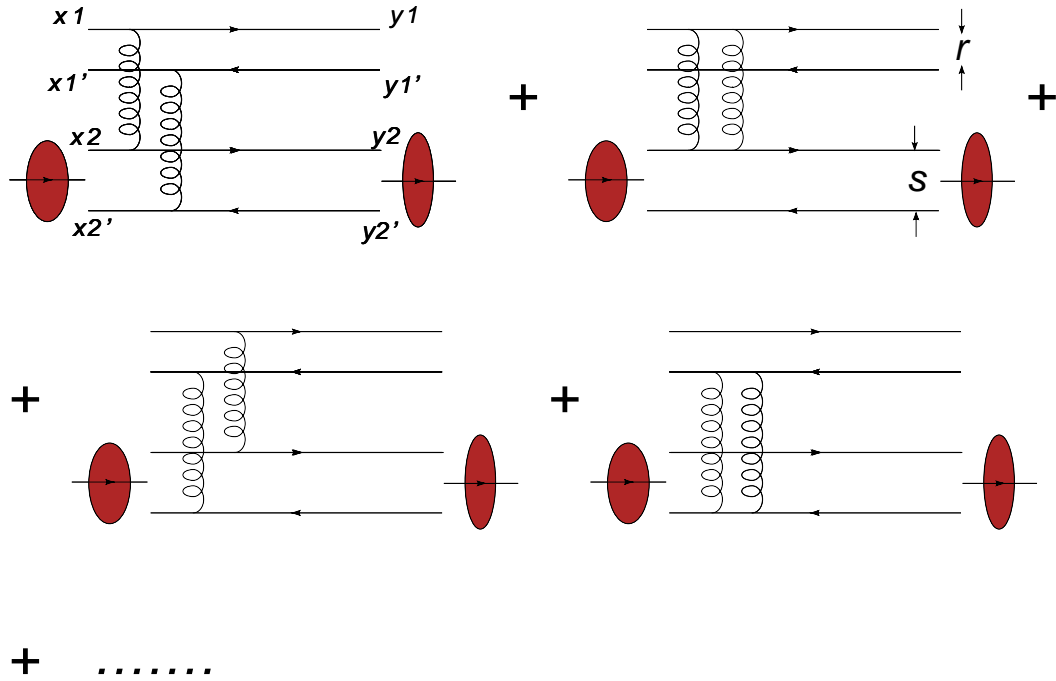
Figure 1-8: Diagram expansion of the interaction of a quark pair (1) with spectator nucleons, in this picture schematized as a dual quark object also (2).

One can see the simplified scheme for an example of the behavior of a quark pair's interaction in a nucleus in figure 1-8. The kernel of the interaction can be expanded as a single interaction contributions between the quarks. Considering that there will be a relative minus sign for interactions of quarks with opposite and like color charges, the kernel will

have the form:

$$K(x_i, x_j') = V(x_1 - x_2)[V(x_1 - x_2) - V(x_1 - x_2') + V(x_1' - x_2') - V(x_1' - x_2)]+$$

$$- V(x_1' - x_2)[V(x_1 - x_2) - V(x_1 - x_2') + V(x_1' - x_2') - V(x_1' - x_2)] + ... =$$

$$(1.21)$$

$$= \{-[V(x_1' - x_2) - V(x_1 - x_2)] + V(x_1' - x_2') - V(x_1 - x_2')\}^2$$

Because we are interested in the short distance region, selected by the high Q^2 of the reaction, we can expand the kernel in Equation 1.21 for $r = |x_1' - x_1| \to 0$, giving:

$$K(x_i, x_j') \sim \{r \cdot \nabla[V(x_1 - x_2') - V(x_1 - x_2)]\}^2 \qquad (1.22)$$

This shows that the interaction is proportional to r^2 for $r \to 0$. So, a more and more Point Like Configuration ($r \to 0$), tuned by Q^2, will select the quark configuration that will have a little interaction in a nucleus, giving the quark pair the possibility to pass trough many fermis of matter, in other words Color Transparency. We will see that a more detailed analysis using pQCD, will express the matter more rigorously.

1.3.3 Kopeliovic model

As indicated by Feinberg and Pomeranchuk [28] and by Good and Walker [29] , more that theirs own energy and mass, one quantity that will affect the single particle states time evolution of quarks' combinations is the energy difference of states with the same momentum P_z. In the ultra-relativistic limit (considered in the z direction),

$$\left.\begin{array}{l} E_1 = \sqrt{m_1^2 + p^2} \sim p_z\sqrt{1 + \frac{m_1^2}{p_z^2}} \sim p_z(1 + \frac{1}{2}\frac{m_1^2}{p_z^2}) \\[2em] E_2 = \sqrt{m_2^2 + p^2} \sim p_z\sqrt{1 + \frac{m_2^2}{p_z^2}} \sim p_z(1 + \frac{1}{2}\frac{m_2^2}{p_z^2}) \end{array}\right\} \; E_1 - E_2 \sim \frac{m_1^2 - m_2^2}{2\,p_z} \qquad (1.23)$$

In defining consistently the Transparency phenomena it is important to define rigorously the time evolution of the quark pair that will compose the virtual meson in the final state. As shown by Kopeliovic and others in [30] [31] [32] [33] in the interaction of a virtual photon in a nucleus one could discern between

14
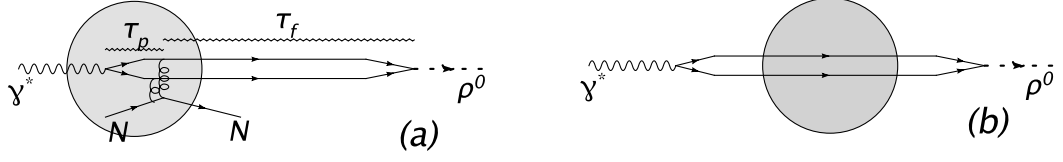
Figure 1-9: Space-time schematic of the production of a ρ^0 from the interaction of a $\gamma*$ with a nucleus. The process can be described in 2 different ways: (a) The creation time (τ_p) is much smaller than the interaction distance (the circular blob) ; (b) it exceed the nuclear radius. This difference leads to a different description of the transparency factor

- Production time, the time in which the γ^* will oscillate creating a quark-antiquark pair that will interact with the nucleons,

- Formation time, the time it takes the quark pair, after the nuclear interaction, to reach a stable hadronic condition.

The Transparency factor, as shown in figure 1-9, will depend on the characteristics of the virtual photon, giving its ability to trigger different time scales for the spectator target. If the production time (τ_p) is smaller than the nuclear radius, the transverse (respect to the direction of the $q\bar{q}$ system) evolution of the pair will have similar time scale to the nuclear target, and so will be influenced from it. Changing phase space, also its transverse momentum will be affected by it. In the opposite case of $\tau_p >> R_{Nucleus}$, the transverse property of the $q\bar{q}$ will be mostly "frozen" during the passage in the nucleus, and so the effect of the medium will be only a simple attenuation factor. If one is using a functional integral representation, the evolution operator of the $q\bar{q}$ system can be schematized as an attenuation factor of the form [30]

$$\exp\left\{-\frac{1}{2}\int dl\,\sigma(\tau_T)\,\rho_A(\vec{r})\right\} \tag{1.24}$$

where τ_T represent the transverse distance between the quarks of the virtual meson traveling into the nucleus. The evolution operator, calculated in the Laboratory Frame, will be of the form [30]:

$$U = \int D^3\tau\,exp\left\{i\int dt\,L_{eff}(\tau,\dot{\tau},t)\right\} \tag{1.25}$$

where L_{eff} is the effective Lagrangian and will be defined as:

$$L_{eff}(\tau, \dot{\tau}, t) = L(\tau, \dot{\tau}) + i\frac{\gamma v}{2}\sigma(\tau_T))\rho_A(\vec{r(t)}) \tag{1.26}$$

The Lagrangian of the quark, anti-quark is then close to the one of an harmonic oscillator

$$L(\tau, \dot{\tau}) = \frac{\mu\dot{\tau}^2}{2} - \frac{\mu\omega^2\tau^2}{2} \tag{1.27}$$

that is driven in this model by the interaction in the nuclei using the second term in Equation1.26. μ is the reduced mass of the system and ω is connected to the formation time of the virtual meson. Using some approximation, valid for $\tau_T << 1$, one can approximate the cross section $\sigma(\tau_T)$ to a term proportional to τ^2, so that it can be absorbed in the frequency term.

$$\omega_T = \left[\omega^2 - i\delta(\vec{r})\right]^{\frac{1}{2}} \tag{1.28}$$

If one considers the nuclear density as a multistep function, the value of $\delta(\vec{r})$ is "frozen" at every step to the value assumed at a certain time. One can then reconstruct the evolution operator from the multistep function.

$$U(t_{n+1}) = U(t_{n+1} - t_n)U(t_n) \tag{1.29}$$

In this way the problem simplifies because at every single step the evolution operator corresponds to the one of an harmonic oscillator at constant frequency (see for example [34])

$$< y|U(t)|x > = \left[\frac{\mu\omega}{2\pi i \ sin(\omega t)}\right]^{\frac{1}{2}} \exp\left\{\frac{i\mu\omega}{2 \ sin(\omega t)}[(y^2 + x^2)cos(\omega t) - 2xy]\right\} \tag{1.30}$$

One can thus completely determine the evolution operator, solving the multistep system obtained from Equation 1.29 , using the completeness relation $1 = \sum_z |z > < z|$ and doing the integral

$$< y|U(t_{n+1})|x > = \int dz \ < y|U(t_{n+1} - t_n)|z > < z|U(t_n)|x > \tag{1.31}$$

1.3.4   L. Frankfurt, G.A. Miller, M. Strikman Model

Another approach used for testing the Color Transparency effect is a model developed by L.Frankfurt, G.A.Miller, M.Strikman [2], that, from a basis created using the Glauber picture, adds the interaction particular of quarks in a Point Like Configuration. With this

approach the physical hadron limit, well described by the Glauber model, comes straight-forward. First we separate the two contributions to the total scattering (see figure 1-2 and 1-3):

- ρ^0 meson photoproduction from a single nucleon (where $t = -q^2$ is the momentum transfer with the nucleon and t_0 is the minimum possible value assumed by t for this reaction. For the definition of t see equation 3.11 and 58)

$$\frac{d\sigma^{\gamma^* V}}{dt} = \left[\frac{d\sigma^{\gamma^* V}}{dt}\right]_{t=t_0} e^{(-B_1 q^2)} \tag{1.32}$$

- Elastic rescattering of the already created vector meson

$$\frac{d\sigma^{VV}}{dt} = \left[\frac{d\sigma^{VV}}{dt}\right]_{t=0} e^{(-B_2 q_\perp^2)} = \frac{\sigma_{tot}^2}{16\pi}(1+\alpha^2)e^{(-B_2 q_\perp^2)} \tag{1.33}$$

This parametrization is useful because it enhances the role of the cross section dependence on the momentum transfer with the target. We can now assume that the full cross section will be given by the sum of all the possible different number of elastic rescattering (n in equation 1.34). from this will follow the definition of the nuclear transparency T_A in this description:

$$\frac{d\sigma}{dt} = \sum_{n=0}^{\infty} \frac{d\sigma_n}{dt} \implies T_A = \frac{\frac{d\sigma}{dt}}{A\frac{d\sigma^{\gamma^* V}}{dt}} = \sum_{n=0}^{\infty} \frac{\frac{d\sigma_n}{dt}}{A\frac{d\sigma^{\gamma^* V}}{dt}} = \sum_{n=0}^{\infty} T_n \tag{1.34}$$

Glauber picture

The starting picture of this model is based on the Glauber theory. If one considers the contribution with no elastic rescattering to the cross section one find

$$\frac{d\sigma_0}{dt} = A\overbrace{\frac{d\sigma^{\gamma^* V}}{dt} \int d^2b \int_{-\infty}^{\infty} dz\, \rho(b,z)}^{(a)} \overbrace{(1 - \sigma_{tot} T(b,z))^{A-1}}^{(b)} \tag{1.35}$$

$$T(b,z) = \int_z^{\infty} dz'\rho(b,z') \text{ ,where } \rho(b,z) = \frac{\rho_0}{1 + e^{\frac{\sqrt{b^2+z^2}-R}{a}}} \text{ and } \int d^2 b\, T(b,-\infty) = 1. \tag{1.36}$$

In equation 1.35 the part (a) represents the sum of all the possible contributions for scattering a Vector meson from a γ^* in a target with density given by $\rho(b, z')$ (where, in equation 1.36, $R = 1.1A^{\frac{1}{3}}$ is the nuclear radius); part (b) refers to the probability of not having an elastic rescattering $(1 - \sigma_{tot}T(b, z))$ from all the remaining nucleons $(A - 1)$ starting from the point of the vector meson's creation z.

If one considers now the case where a single elastic rescattering occurs, one obtains:

$$\frac{d\sigma_1}{dt} = A \overbrace{\left[\frac{d\sigma^{\gamma^* V}}{dt}\right]_{t=t_0}}^{(a)} \overbrace{(A-1)\left[\frac{d\sigma^{VV}}{dt}\right]_{t=0}}^{(b)} \overbrace{\int d^2 b \int_{-\infty}^{\infty} dz\, \rho(b, z)}^{(a)} \overbrace{T(b, z)}^{(b)} \overbrace{(1 - \sigma_{tot}T(b, z))^{A-2}}^{(c)} \times$$

$$\times \overbrace{\int \frac{d^2 q_1}{\pi} \frac{d^2 q_2}{\pi} \delta^2(\vec{q_1} + \vec{q_2} - \vec{q})}^{(d)} \overbrace{e^{-B_1 q_1^2}}^{(a)} \overbrace{e^{-B_2 q_2^2}}^{(b)} \qquad (1.37)$$

In equation 1.37:

(a) Refers to the production of the Vector meson;

(b) Is related to all the possible $(A - 1)$ single elastic rescattering from the point z of creation of the meson ρ^0;

(c) Describes the probability that no other elastic rescattering occurs;

(d) Integrates over all possible perpendicular momentum transfers between the two processes that gives the same total momentum transfer with the nucleus $\vec{q} = \vec{q_1} + \vec{q_2}$ (where $|\vec{q}|^2 = -t$).

In order to understand the momentum constraint in (d), we need to see how we experimentally determine t in the reaction under study (see figure 3-1 at page 48 and equation 3.11). In the first order approximation at the kinematical energies used in the EG2 experiment, t describes the interaction with a nucleon N as showed in figure 3-1 (designed with the term $d\sigma_0/dt$ in equation 1.35). The terms with elastic rescattering $(d\sigma_1/dt, d\sigma_2/dt, \cdots)$ enter into the correction to the Transparency (see figure 1-10). Considering that t is derived from the difference of the detected ρ^0's momentum (after it passes through the nucleus) with the momentum of the virtual photon, t will carry the information of all the interactions with the target (creation of the vector meson and all the possible elastic combinations).
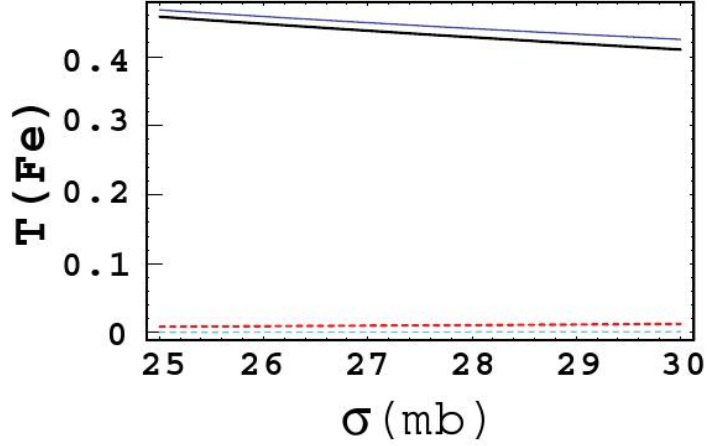
Figure 1-10: Glauber model calculation as a function of $\sigma_{tot} = \sigma$ for the different contribution to the Nuclear Transparency T_A as defined in equation 1.34 [2]. In black is shown the contribution due to T_0 (equation 1.35); Dashed in red is the one from T_1 (equation 1.37); Dashed in chan is T_2. The solid blue line on the top represent the sum of the 3 terms $T = T_0 + T_1 + T_2$. T_0, the contribution to the Nuclear Transparency due to the possibility of no elastic rescattering, is the leading term at these energies.

Treatment of the ρ^0 decay

This model was also implemented with the effects of ρ^0 decay inside the nucleus into a π^+, π^- pair: This will modify the second step of the interaction with the target when, after being created, the vector meson propagates through the nucleus. For this reason, in this step, the cross section σ_{tot} needs to be replaced:

$$\sigma_{tot}T(b,z) \rightarrow \int_z^\infty dz' \, \rho(b,z') \, \hat{\sigma}(z'-z) \tag{1.38}$$

where :

$$\hat{\sigma}(z'-z) = \sigma_{tot} \exp\left(-\frac{\Gamma_{\rho^0} m_{\rho^0}}{\sqrt{\nu^2 - m_{\rho^0}^2}}(z'-z)\right) + 2\sigma_{\pi N}\left(1 - \exp\left(-\frac{\Gamma_{\rho^0} m_{\rho^0}}{\sqrt{\nu^2 - m_{\rho^0}^2}}(z'-z)\right)\right) \tag{1.39}$$

In equation 1.39 the cross section is divided in two parts, both weighted with the decay rate for the ρ_0 boosted in its system frame, $(\Gamma_{\rho^0} m_{\rho^0}/\sqrt{\nu^2 - m_{\rho^0}^2})$: Both the decay rate and so the cross section for the produced $\pi^+ \pi^-$, are proportional to the distance traveled from the creation of the vector meson $(z'-z)$. This effect produces a rise in the measured Nuclear

19

Transparency that at its maximum is $\sim 5\%$ for low ρ^0 meson energies. It is then important to include this calculation in the theoretical prediction of this data-set.

Implementation with Color transparency

From this Glauber model developed as a basis, One needs to add the effects due to Color Transparency. One will expect two different effects if one checks the structure of the cross section (see equation 1.34).

- The contribution in the first term in the sum $(d\sigma_0/dt)$ will be enhanced. This part takes into account all the processes characterized by the creation of the vector meson without any elastic rescattering.

- In correspondence to a reduced interaction with the rest of the nucleus, the values of the higher order terms (in n^{th} ρ^0 rescattering) are expected to shift to the lower order.

This approach, developed by Frankfurt and Strikman, adds two other steps to the picture of equation 1.39. The cross section σ_{tot} of the created vector meson will be substituted by an effective cross section σ_{eff}. If one also considers the effects due to the ρ^0 meson's decay (where for simplicity it is assumed that the momentum of the vector meson will be equally divided between its decay's products) one has

$$
\sigma_{eff}^D(z'-z, p_{\rho^0}) = \sigma_{tot}(p_{\rho^0}) \left[\left(\frac{n^2 <k_T^2>}{Q^2} + \frac{z}{l_h}(1 - \frac{n^2 <k_T^2>}{Q^2}) \right) \theta(l_h - (z'-z)) \right]
$$
$$
+ \sigma_{tot}(p_{\rho^0}) \left[\theta((z'-z) - l_h) \exp\left(-\frac{\Gamma_{\rho^0}}{\gamma_{p_{\rho^0}}}(z'-z) \right) \right]
$$
$$
+ 2\sigma_{\pi N}(\frac{p_{\rho^0}}{2}) \left[\theta((z'-z) - l_h) \left(1 - \exp\left(-\frac{\Gamma_{\rho^0}}{\gamma_{p_{\rho^0}}}(z'-z) \right) \right) \right]. \quad (1.40)
$$

In equation 1.40 $l_h = 2p_{\rho^0}/\Delta M^2$ sets the time scale of the evolution of the created Point Like Configuration to the final Vector meson. Schematically, one can explain this equation with the following sequence:

1. A Point Like Configuration is created with cross section $\sigma_{PLC} = \sigma_{tot}(p_{\rho^0}) \frac{n^2 <k_T^2>}{Q^2}$ (where $n = 2$ is the number of quarks involved and $<k_T^2>^{1/2} \simeq 0.35\,GeV$). This will be altered by the Q^2 of the reaction.

2. The quark pair evolves linearly from the starting low interaction state to the full vector meson in a time/space scale determined by l_h (and so does the cross section, see figure 1-11). All this happens in the shell described by the relation $(z' - z) < l_h$.

3. Outside this shell ($\theta((z' - z) - l_h)$) the vector meson will start to decay and the cross section will be described with the sum of both the ρ^0 part and the two pion part (which for simplicity has been taken with the same momentum fraction $p_{\rho^0}/2$).
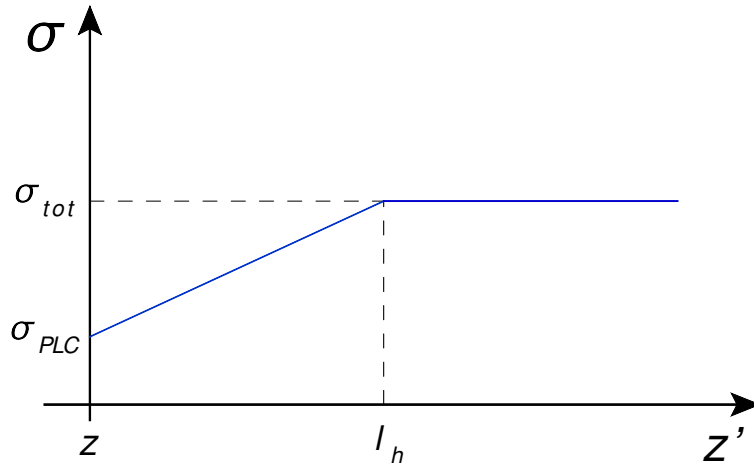
Figure 1-11: Cross section evolution in space from the creation of a Point Like Configuration (σ_{PLC}) to the creation of the final vector meson as described in equation 1.40

1.4 Previous data

For more than 20 years many experiments have been searching for the detection of the Color Transparency effect. The first experiment searching for Color Transparency was performed at BNL [3] (see figure 1-12). The Transparency factor defined for this experiment increased as expected with the beam momentum, following the theoretical prediction of Color Transparency. After a peak for effective proton's momentum around $10 GeV/c$, it started to decrease to values comparable to those of the Glauber Model. This behavior was explained by J.P. Ralston and B. Pire [6], interpreting the proton-proton elastic scattering

in a nuclear target as an interference between two perturbative processes: The one giving rise to Color Transparency and the contributions of Landshoff-type diagrams [35] (which dominate at high energy).
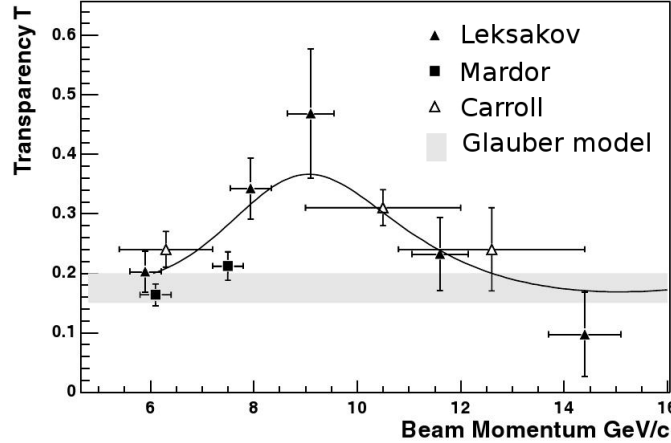
Figure 1-12: Large angle Quasielastic proton-proton scattering from different nuclear targets is compared to proton-proton scattering in hydrogen at 3 different proton momenta $(6, 10, 12 GeV/c)$ [3]. The Nuclear Transparency increases untill the effective beam momentum energy of $10 GeV/c$ and then decreased. This behavior raised some question about the quality of the event selection (the measurement involved momentum analysis of only one of the two final-state protons), but was later confirmed by two different measurements by Mardor [4] and Leksakov [5] using the EVA detector at the Brookhaven AGS. Was then explained by J.P. Ralston and B. Pire [6]

To avoid this problem of interference between the Color Transparency phenomena and other processes, many experiments have been done studying a quasi-free e, e', p reaction (at Bates [7], at SLAC [8] [9] and at Jefferson Lab [10] [11], see figure 1-13). All these experiments seem to follow the Glauber description of the interaction with matter, failing to find a hint for Color Transparency.

The first experiment that showed a clear signal of Color Transparency was performed at FNAL [36] where the relative cross sections for diffractive dissociations into dijets of $500 GeV/c$ pions scattering from carbon and platinum was measured. The cross section, if parametrized as $\sigma = \sigma_0 A^{\alpha}$, gives a result of $\alpha \sim 1.6$. The observed A dependence is
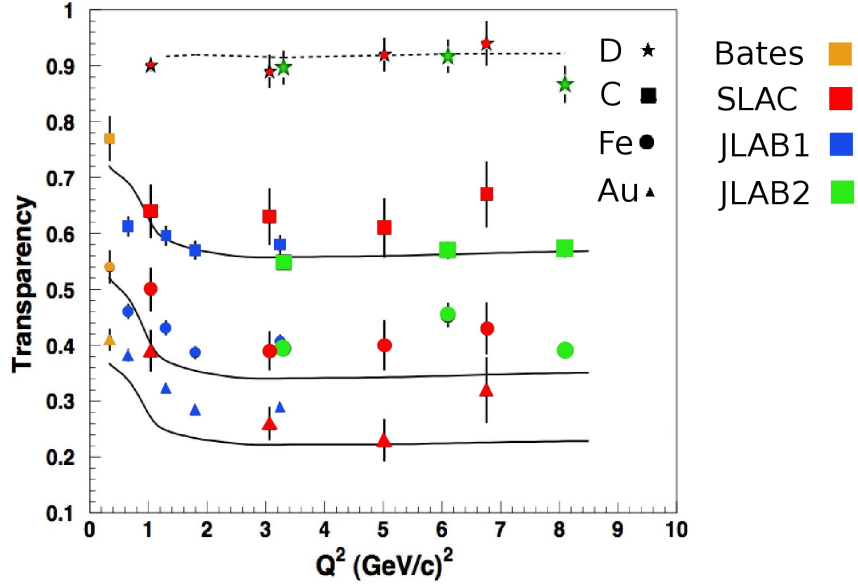
Figure 1-13: The quasi-free e, e', p reaction has been studied at several facilities with a Q^2 range of $0 - 9(GeV/c)^2$. Here are the results from Bates (for this experiment the data points refer from top to bottom respectively to Carbon, Nickel and Tantalum), [7],from SLAC [8] [9] and from Jefferson Lab ([10] (1)) ([11] (2)). The theoretical curves using Glauber calculations (solid curves from [12], dashed curve from [13]) predicts the experimental behavior well, indicating that all these experiments lack the expected increase due to Color Transparency

consistent with calculations with Color Transparency models and is very different from the one expected from inclusive $\pi - nucleus$ scattering ($\sigma \propto A^{2/3}$). This implies that the coherent scattering of the $q\bar{q}$ PLC as predicted by Color Transparency was observed .

Another experiment that showed results consistent with the Glauber calculations which include Color Transparency was performed at the Thomas Jefferson Laboratory facility (in Hall A [14], see figure 1-14 and 1-15). This experiment used pion photoproduction to study the process $^4He, (\gamma n \rightarrow p \pi^-)$ at $\theta^\pi_{cm} = 70°$ and $90°$. It showed an increase in the transparency with a corresponding increase in the squared momentum transfer $|t|$: This result is more evident with the data with $\theta^\pi_{cm} = 90°$, because it targets higher $|t|$ (see figure 1-15).

Also using the high intensity electron beam of the Jefferson Laboratory facility (but this time
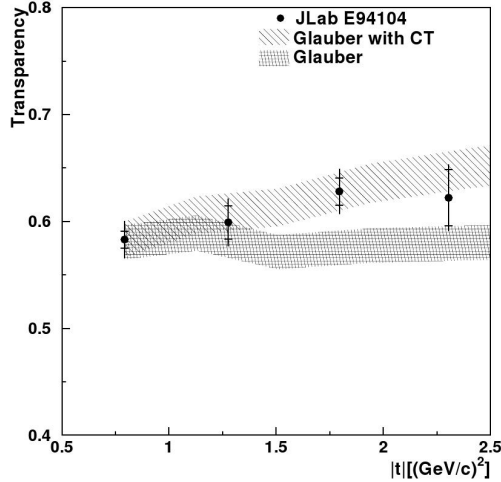
Figure 1-14: Nuclear Transparency for ^4He [14] as a function of the momentum transfer square $|t|$ for $\theta_{cm}^{\pi} = 70°$. Theoretical prediction of a Glauber model calculation and a Glauber model with CT are also shown.
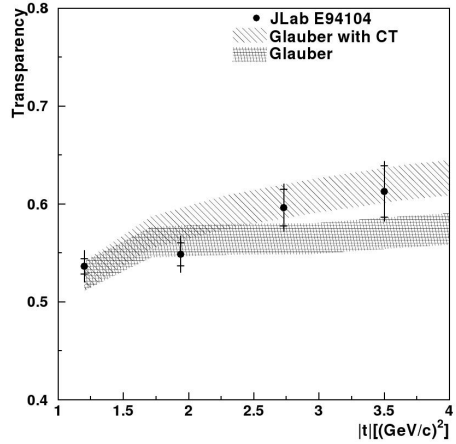
Figure 1-15: Nuclear Transparency for ^4He [14] as a function of the momentum transfer square $|t|$ for $\theta_{cm}^{\pi} = 90°$. The shaded regions show predictions from a Glauber model with and without CT effect.

in Hall-C) another experiment used Pion electroproduction for studying Color Transparency [15]. The reaction $(\gamma^* p \rightarrow n \pi^+)$ was investigated on $^2H, ^{12}C, ^{27}Al, ^{63}Cu$ and ^{197}Au over a Q^2 range of 1.1 to $4.7 (GeV/c)^2$. The Nuclear Transparency and the parameter α (that is also dependent on A) were then plotted as a function of Q^2 and compared to different theoretical models (see figure 1-16 and 1-17).

1.4.1 Exclusive ρ^0 production

Exclusive electroproduction of vector mesons such as the ρ^0 was suggested as a bench test for finding Color Transparency. The size of the vector meson, controlled by the virtuality of the photon, could also reach values below the normal hadron for modest Q^2 values: In fact, the transverse separation of the $q\bar{q}$ pair $(\sim 2\hbar c/Q)$ at a $Q^2 \sim 2GeV^2$ is calculated to be around $0.3fm$, much smaller than its normal size $(\sim 1fm)$ [16]. The first experiment to study the Color Transparency effect in exclusive ρ^0 electroproduction was an experiment using the Fermilab Tevatron muon beam at the energy of $470GeV$ [16] (see figure 1-18 and 1-19). The rise of the Nuclear Transparency with Q^2 did not have the statistical precision
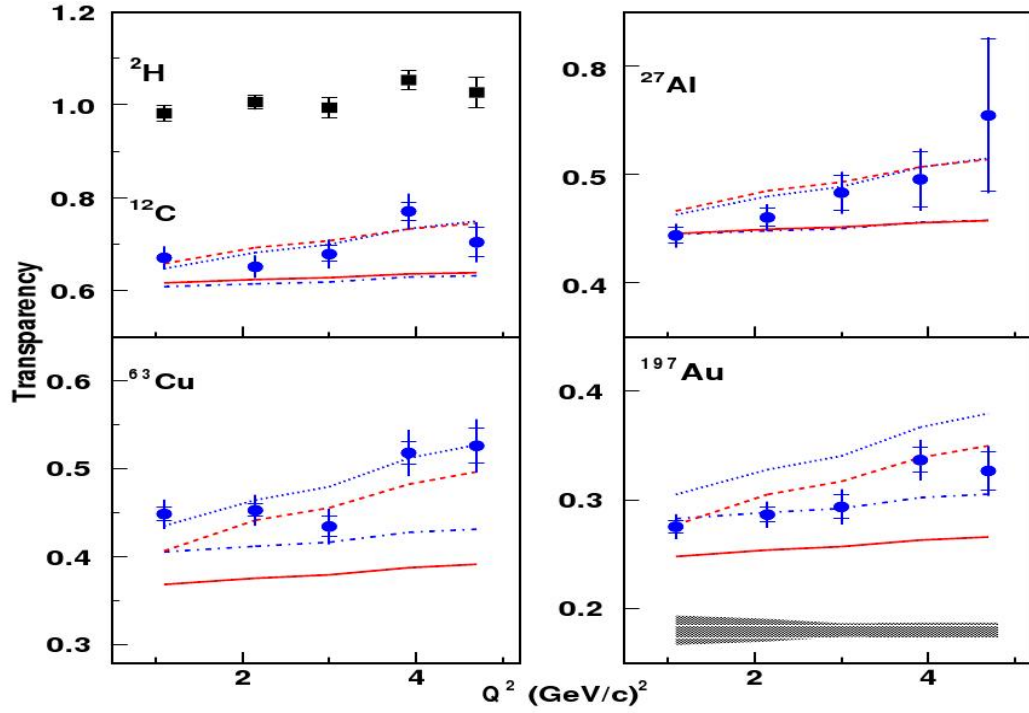
Figure 1-16: Nuclear Transparency T is defined as $(\frac{\bar{Y}}{Y_{MC}})_A/(\frac{\bar{Y}}{Y_{MC}})_H$ vs Q^2 for different target combinations[15]. The model used for interpreting the data are: Glauber model (solid red line), Glauber model + CT (dashed red line), Glauber model including Short Range Correlations (blue dot-dash line), Glauber model including SRC + CT (blue dotted line). The dark band in the bottom right panel represents the model uncertainties and is common to all targets.

needed to fully determine the experimental sight of Color Transparency.

Another data-set that used exclusive incoherent ρ^0 production was the HERMES experiment, which used the $27.5 GeV$ HERA positron storage ring at DESY [37] with ^1H and ^{14}N targets. The kinematical range of the virtual photon ($0.8 GeV^2 < Q^2 < 4.5 GeV^2$ and $5 GeV < \nu < 24 GeV$) was such to trigger coherence length effects, as shown in figure 1-4 and figure 1-20. The coherence length is defined as $l_c = (2\nu)/(M_{\rho^0}^2 + Q^2)$ and this experiment covers a range from $l_c \sim 1 fm$ to $6 fm$. To disentangle the coherence length signal from the one of Color Transparency, coherence length bins of $0.1 fm$ were used [19]. The Transparency is defined as the ratio of the nuclear cross section per nucleon to that on the proton, $T = \sigma_A/(A\sigma_p)$. The results are shown in figure 1-21. An increase in the
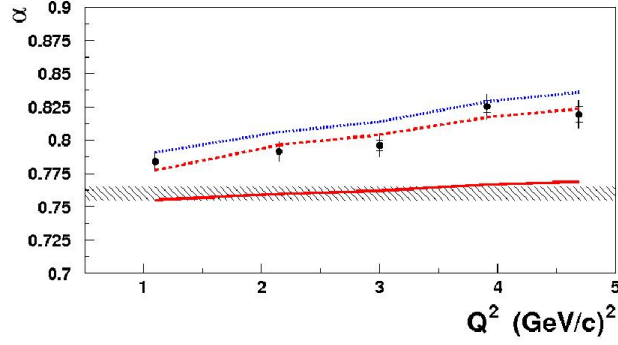
Figure 1-17: The value of α obtained from $T = A^{\alpha-1}$ is plotted here vs Q^2[15]. The red solid curve represents the theoretical calculation of the Glauber model, the dashed red one Glauber represents + CT, the blue dotted one represents Glauber + CT + Short Range Correlations. The value of α obtained from pions nucleons scattering data is $\alpha \sim 0.76$ and is plotted as the gray hatched band.

Transparency T_A with an increase in Q^2 for each of the coherence length bins will be a signal of Color Transparency. For this reason T_A was parametrized as a linear function in Q^2, $T_A = P_0 + P_1 Q^2$. A fit was done in each l_c bin, the parameter P_1 being common to all the bins. The results shows $P_1 = (0.089 \pm 0.046 \pm 0.020) GeV^{-2}$.
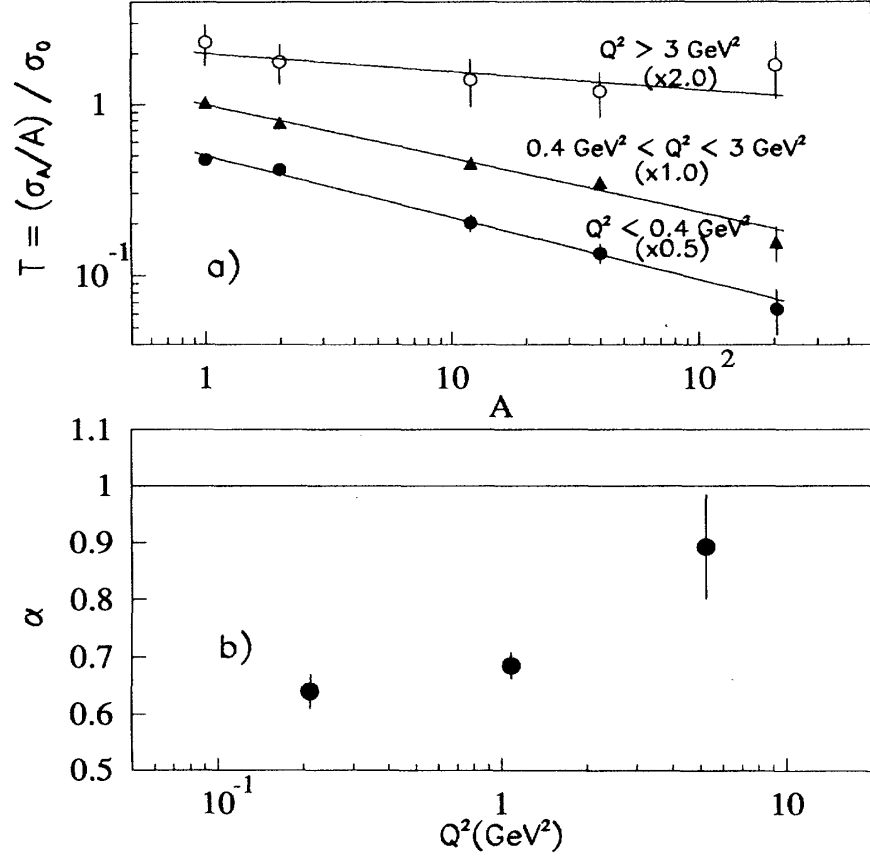
Figure 1-18: The Transparencies $T = \sigma_A/A\sigma_0$ (where $\sigma_A = \sigma_0 A^\alpha$) for the experiment $E665$ at Fermilab [16]: Here the data respectively of ρ^0 electroproduction off hydrogen, deuterium, Carbon, Calcium and Lead is plotted versus A for three different bins in Q^2. The three sets of points have been multiplied by $\times 2.0$ ($Q^2 > 3 GeV^2$), $\times 1.0$ ($0.4 GeV^2 < Q^2 < 3 GeV^2$), $\times 0.5$ ($Q^2 < 0.4 GeV^2$). The α found in the fit is then plotted in the lower picture as a function of Q^2(A value of $\alpha = 1$ will indicate full transparency) : Color Transparency will imply a Q^2 dependence for the parameter α in kinematical range of this experiment. The error here are just statistical.

27
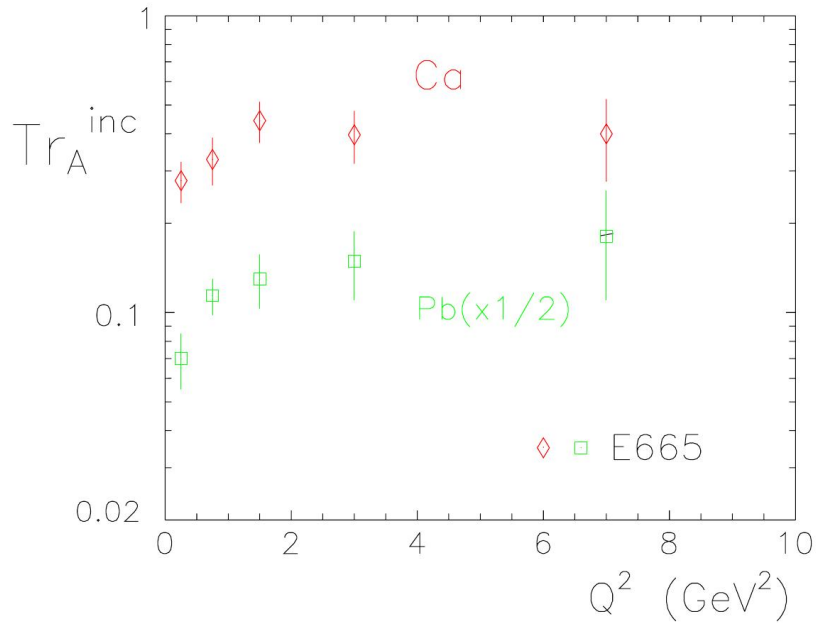
Figure 1-19: Nuclear Transparency ratio for incoherent ρ^0 muon-production vs. Q^2 [16].
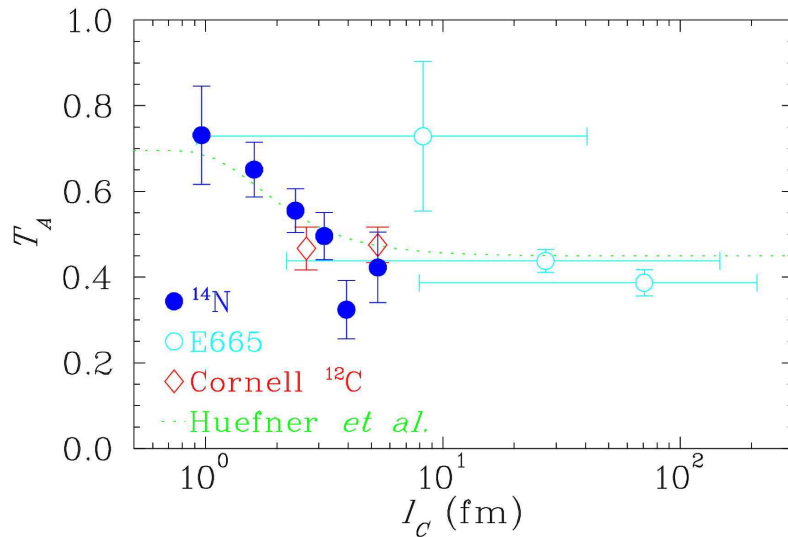
Figure 1-20: The Transparency T_A is plotted here as a function of l_c. The data in blue refers to the HERMES data-set and shows how this experiment was right on the kinematical range where the Coherence Length effect is more important. The dashed line is the theoretical prediction using a Glauber model from Hufner et al. [17] and interprets the physical behavior well. This plot also shows a comparison with previous measurements with photon (red diamonds) [18] and muon beam (the Fermilab experiment E665, pictured with cyan circles).
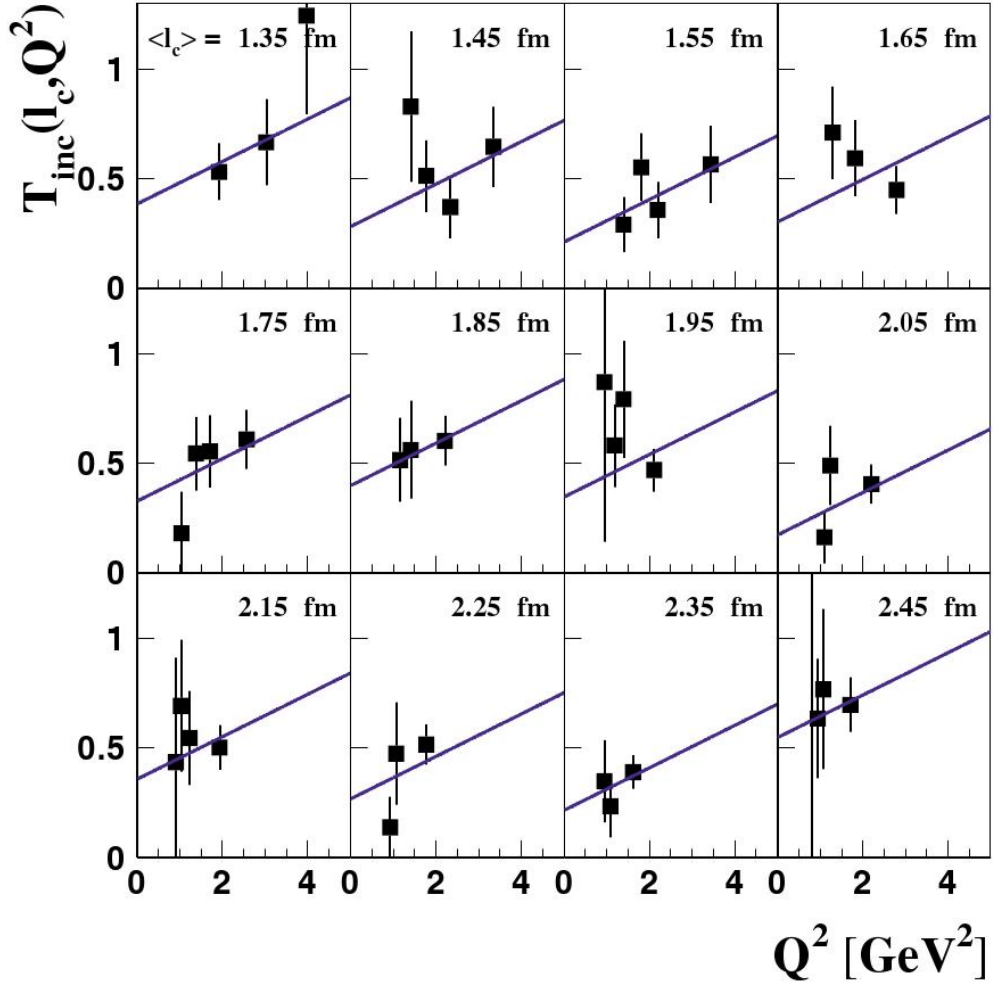
Figure 1-21: Nuclear Transparency as a function of Q^2 in different coherence length bins of $0.1 fm$ for incoherent ρ^0 electroproduction on Nitrogen [19]. A fit $T_A = P_0 + P_1 Q^2$ was used in each l_c bin, the parameter P_1 being common to all the bins. This permitted a better definition of the slope of the Transparency vs Q^2, phenomena that is due to Color Transparency. The slope was found to be $P_1 = (0.089 \pm 0.046 \pm 0.020) GeV^{-2}$

Chapter 2

EXPERIMENTAL APPARATUS

AND DATA ENSEMBLE

The Thomas Jefferson Accelerator Facility (TJNAF) is the site of a recirculating linear electron accelerator, capable of delivering beams to three experimental Halls simultaneously. These three Halls are designed to target different physics. While Hall A and Hall C have high resolution spectrometers that are able to determine the momentum of a particle with an accuracy of $\sim 10^{-4}$, Hall B uses a Large Acceptance Spectrometer that has a very wide solid angle range, but is characterized by a lower resolution ($\sim 5 - 10 \times 10^{-3}$).

2.1 Continuous Electron Beam Facility (CEBAF)

The Jefferson's Laboratory's CEBAF (Continuous Electron Beam Accelerator Facility) is a pair of antiparallel superconducting radio-frequency linacs (see figure 2-1) joined by two 180° arcs with a radius of 80 meters [38]. The linacs consist of 320 superconducting radio-frequency cavities that boost the beam with radio-frequency waves (see figure 2-2). The recirculating arcs are composed of five separate beam line sections, which permit the beam to recirculate in both linacs up to 5 times. For each linac the gain in energy varies between $0.4GeV$ to $0.6GeV$, giving a final pick energy that could reach $\sim 6GeV$.
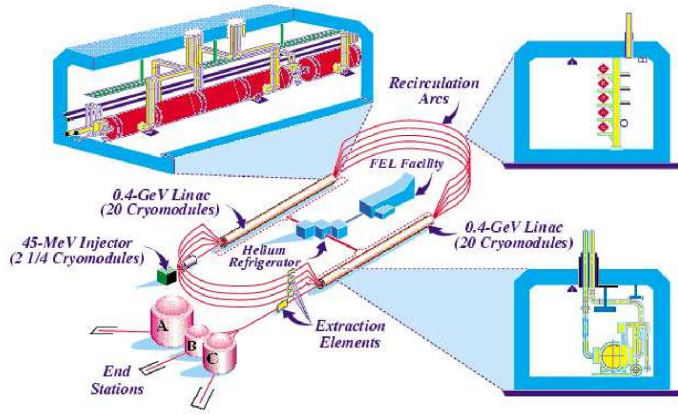
Figure 2-1: TJNAF Accelerator configuration
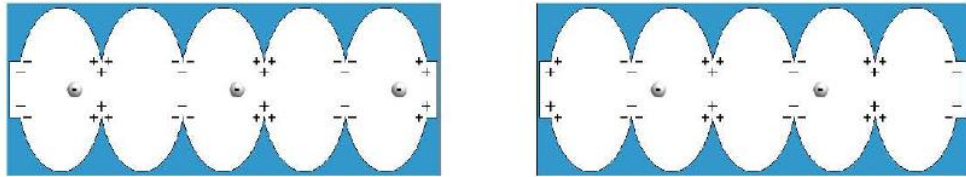
Figure 2-2: Schematic of a superconducting radio-frequency cavity: As the electron moves in the right direction the field's induced charge on the surface of the cavity change so that the moving particle sees an electric field that keeps on accelerating it

2.2 The CLAS detector

CLAS detector has solid angle coverage of near 4π and is capable of detecting charged particles with polar angles from $8°$ to $140°$. Because it requires different detectors combinations, the coverage for neutral particles is from $\theta = 8°$ to $75°$. CLAS is well suited for experiments that require the detection of two or more particles in the final state, because it connects the polar angle range with the full azimuthal coverage. Detectors stability and data acquisition limit the luminosity up to values typical of the configuration of the experiment. For Hall B and the CLAS detector, the electron beam can reach currents in the order of few nA, which corresponds to luminosity $\sim 10^{34} cm^{-2} s^{-1}$. CLAS in composed of several sets of detectors (see figure 2-3), and is designed to accurately measure the momentum, time-of-flight and

trajectory of particles from a reaction target. These measurements allow the identification of the mass, charge and momentum of each particle.
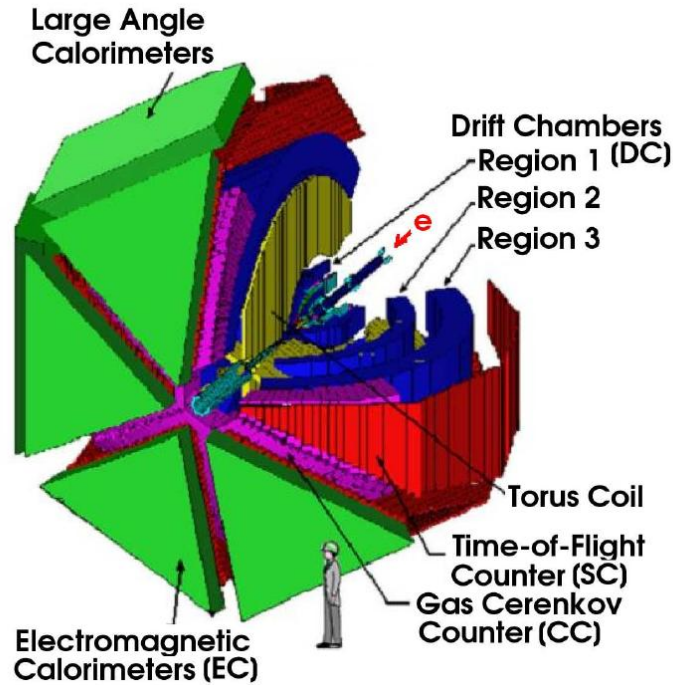
Figure 2-3: The CLAS detector and its components

2.2.1 Main Torus and Mini Torus Magnets

The Main Torus Magnet consists of six superconducting coils positioned in a toroidal geometry (see figure 2-4). The coils are placed perpendicular to the incoming electron beam and they separate the CLAS detector into six parts, described as sectors. The coils create a toroidal magnetic field that is mostly constant around the ϕ-direction, giving an azimuthal symmetry to the CLAS detector. The magnetic field induces for charged particles a curvature in the θ direction (see figure 2-6 and 2-7). This curvature, analyzed with the information given by other detectors, enables us to determine the momentum and mass of a particle.
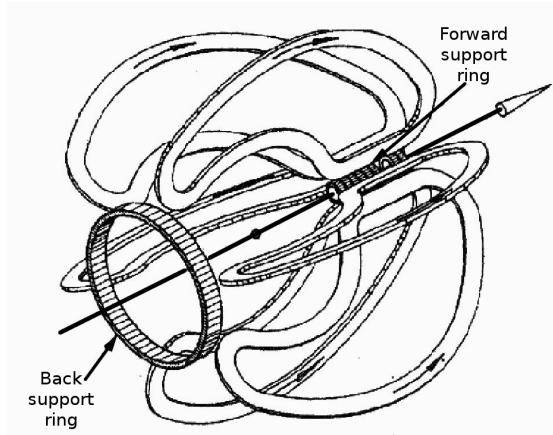
Figure 2-4: The Torus magnet. One can see a picture of one of the coils during construction on figure 2-5

Figure 2-5: Construction of the coils of the Torus magnet

The field's geometry is specifically designed to provide good momentum resolution for charged particles emitted with high energies and small scattering angles, and for particles emitted at lower energies and large scattering angles.

The magnet is ∼5 m in diameter and 5 m in length (see figure 2-5). The coils consist of 4 layers of 54 turns of aluminum-stabilized NbTi/Cu conductor. To keep the coils at a superconducting temperature ($\sim 4.5K$), cooling tubes with recirculating liquid helium surrounds the magnet. The field created reaches $2.5 Tm$ at a current of 3860 A , in the forward direction, and drops to 0.6 Tm at scattering angle of 90°. However, routine operation has limited operation to 87% of the maximum current (3375 A) to keep internal mechanical stresses within safe limits. The direction of the current in the coils can be inverted, causing also a reversal in magnetic field. This permits to have a choice on which ensamble of particles (positives or negatives) will have curvature in-bending or out-bending (respect to the incoming beam direction, axis of symmetry of CLAS).

The Mini Torus is another magnet used in CLAS (see figure 2-8). Placed, between the targets and the first region of Drift Chambers, reduces the background produced by scattered Möller electrons.

Figure 2-7: Magnetic field intensity distribution

Figure 2-6: The Torus magnetic field inside the CLAS detector

2.2.2 Drift Chambers

The Drift Chambers (DC) [39] are the first detector elements encountered by the particles after scattering from the designed target. The Drift Chambers, as part of CLAS is divided in six sectors. Each of the six sectors has three drift chambers at increasingly larger radial distances from the center of CLAS , for a total of 18 separate drift chambers. The DC can track particles with a range in $\theta = 8° - 142°$ with a precision of $2\,mrad$ and determine their momentum if $> 200\,MeV/c$ with an a resolution of 0.5%.

Region 1 (R1) (see figure 2-3) is the closest to the target and is characterized by the smallest magnetic field (see figure 2-6). Moving forward from the center of CLAS we found Region 2 (R2) which, being in the middle of the coils, is characterized by the highest magnetic field. Outside the torus magnet is positioned the last part of the DC , Region 3 (R3).

The tracks are measured with an accuracy of $100\mu m$ in the bend plane (containing the beam line) and $1mm$ in the direction perpendicular to the bend plane. In order to obtain track redundancy and increase pattern recognition each of the chambers is divided into two superlayers. The difference between the two superlayers is that one has wires axial to the

34
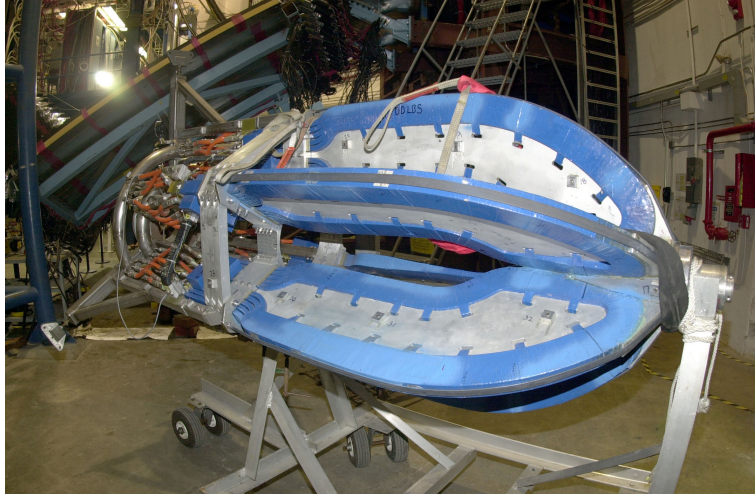
Figure 2-8: Mini Torus magnet in CLAS

magnetic field and the other has its wires tilted of 6° . Each superlayer is composed by six layers of drift cells (R1, being the smallest one, is constituted only of four layers). In total the number of cells that compose the DC detector is 35,000. Figure 2-9 shows a typical track pattern. The shape of each cell is the one of an exagon. A signal wire lies at their midpoint and field wires are positioned at the verteces. There are guard wires at the edges of the chambers held at a high voltage intended to mimic an infinite grid of drift cells. The drift chambers are filled with a typical ionization detector gas mixture of $Argon - CO^2$ in a 9:1 ratio that provides a saturated drift velocity of $4cm/\mu s$. In order to full determine the position in the Drift Chambers and so improving their resolution, the drift time for each channel must be known. This value will need to be determine each time the environmental conditions (such atmospheric pressure, humidity, etc.) in the experimental hall will change because this will influence the Drift Chamber's gas properties. The signal in the Drift Chambers also depends on the particles entrance angle and velocity and the local magnetic field. The drift time to drift distance function for a given entrance angle is parametrized using:

$$x(t) = v_0 t + \eta \left(\frac{t}{t_{max}} \right)^q + k \left(\frac{t}{t_{max}} \right)^p \qquad (2.1)$$
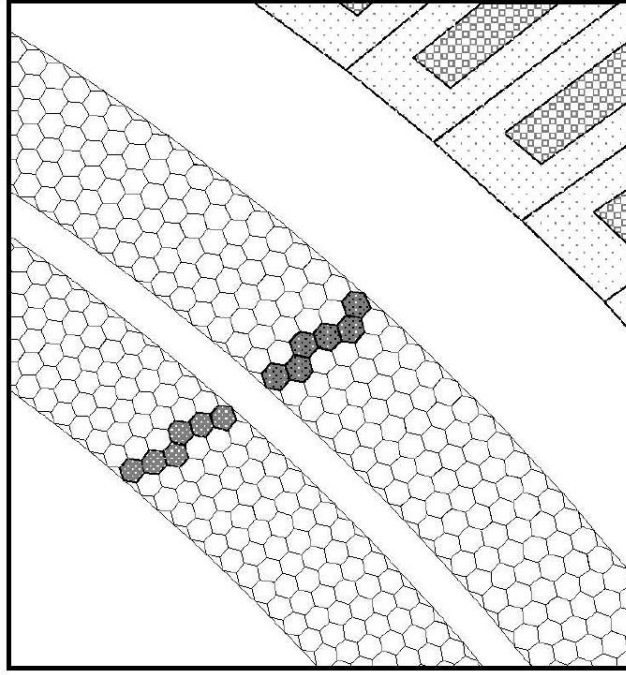
Figure 2-9: Drift chambers track

where t_{max} is the maximum drift time and v_0 is the value for the saturated drift velocity near $t = 0$. The remaining parameter will be determined using a minimization process on

$$\chi^2 = \frac{|x(t) - x_{path}|^2}{\sigma_{path}^2} \qquad (2.2)$$

where x_{path} represents the Distance Of Closest Approach (DOCA) from the sense wire along the path and σ_{path} is its error. Another quantity used to monitor the calibration of the Drift Chambers detector is the residual, defined as

$$|x(t) - x_{path}| \qquad (2.3)$$

For a better result and so testing that the minimization procedure found the right answer in this nonlinear fit, it is still important to control the physical behavior of all these variables (An example of the values measured for σ_{path} can be found in figure 2-10). The CLAS Drift Chambers Region 3 were also pulled out for maintenance during the experiment running time. This required an alignment of this Region with the rest of the detector. Straight

36
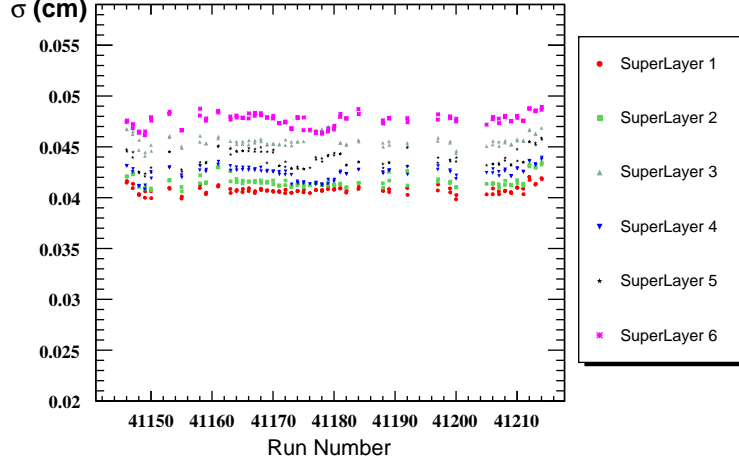
Figure 2-10: DC σ_{path} for different Superlayers for the azimuthal angle which characterizes sector 1. The cell size of the Drift Chambers is increasing with the Superlayer, giving also an increase in the expected value of σ_{path} (as also seen in this plot).

track electrons were taken (where the main Torus current was set to $0A$) and a previous procedure [40] was used to find the final desired alignment (see figure 2-11).

2.2.3 Forward Electromagnetic Shower Calorimeter

The forward electromagnetic shower calorimeter of CLAS (EC) has scattering angles which range from $\theta = 8°$ to $\theta = 45°$ with the corresponding azimuthal coverage of the Drift Chambers (see figure 2-13) [41]. For angles $50° < \theta < 75°$, there is a second detector, called Large Angle Calorimeter, that is constituted of 2 modules (for its description see [42]). The main functions of the EC in CLAS are:

- electron and photon energy resolution $\frac{\sigma}{E} \leq \frac{0.1}{\sqrt{E}}$ where (E is expressed in GeV)

- position resolution $\delta r \approx 2cm$ at $1GeV$

- pion electron rejection greater than 99% for $E \leq 1GeV$

- fast ($< 100ns$) total energy sum for events trigger

- mass resolution for two photon decays $\frac{\delta m}{m} \leq 0.15$

37
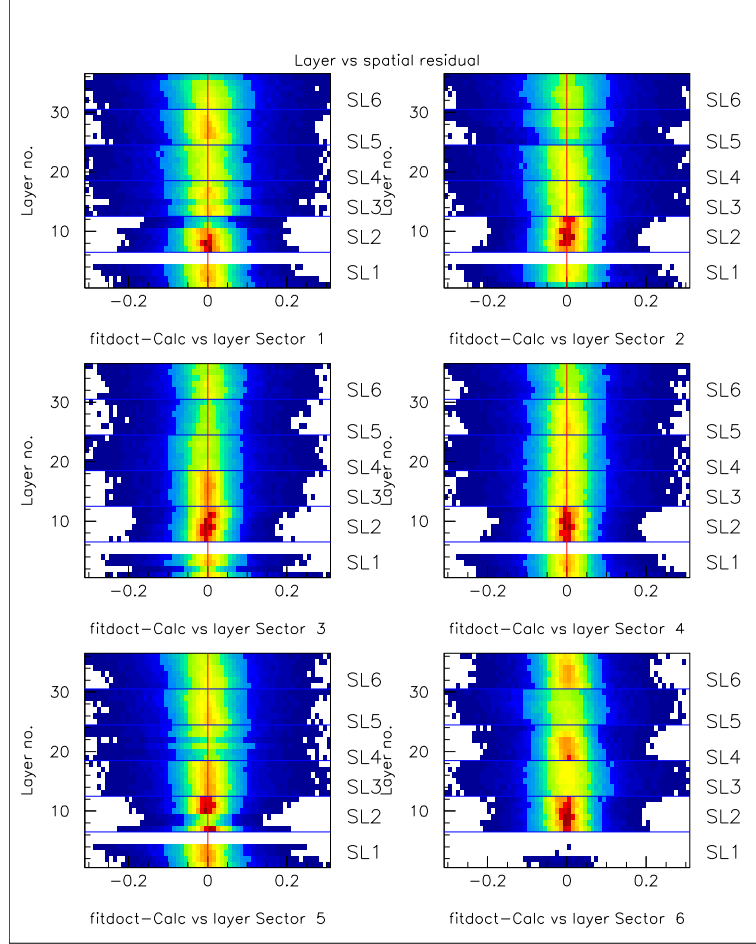
Figure 2-11: Final alignment for the Drift Chambers Region 3. Here Is plotted the residual (X) as a function of the layers in the Drift Chambers(Y) integrated in all the CLAS angle.

- neutron detection efficiency $> 50\%$ for neutron with energy $> 0.5 GeV$

- time of flight resolution $\approx 1 ns$.

For energies in the GeV range, photons lose the main part of their energies in e^+, e^- pair production. Unlike them, electrons and positrons lose it emitting bremstrahlung radiation while changing their momentum. Both these processes create photons that will cause an electromagnetic shower which will be detected using scintillators. Heavier particles (such as pions), due to their bigger inertia, will lose the main part of their momentum by ionization (for particle's energies at which CLAS operates). This signal is distinctly different respect to the electromagnetic shower given by γ, e^+ and e^-. This feature becomes very important

for high energy pions, because if their momentum is $> 2.5 GeV$ the use of the Cerenkov detector for discriminating pions and electrons becomes more challenging (pions start also to emit light in the Cerenkov detector). For better match the hexagonal geometry of CLAS the electromagnetic shower calorimeter is made of alternating layers of scintillators and lead sheets with the shape of an equilateral triangle. Each scintillator layer is made of 36 strips parallel to one of the sides of the triangle. Moving one after another in the following scintillator layers, the strips will rotate $120°$ each time , mapping the charge deposited distribution in the three dimensions. The three different orientations of views parallel to each side of the EC triangle (see figure 2-13), define 3 planes labeled u,v,w. The total number of layers is 13 and they are divided in two groups of 5 layers (inner) and 8 layers (outer) for giving also longitudinal information of the energy deposited by the particle.
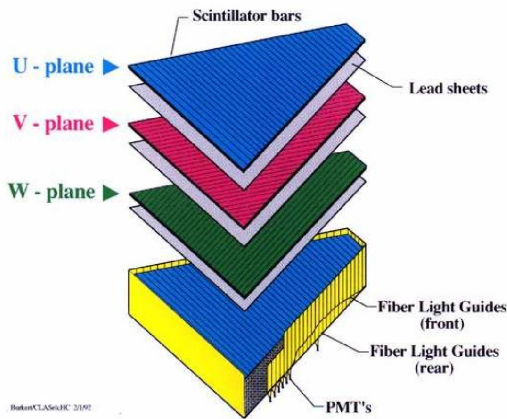
Figure 2-12: Example for one sector of the definition of three different planes of observation (u, v, w) for the Electromagnetic shower Calorimeter
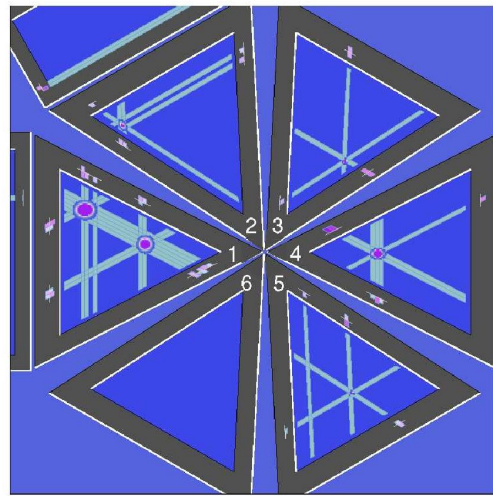
Figure 2-13: Electromagnetic shower Calorimeter example of track reconstruction. One can also see the six sectors structure, that follows the same azimuthal behavior of the Drift chambers (see figure 2-3)

2.2.4 Cerenkov Counters

The main use of the Cerenkov Counters (CC) is to discriminate between electrons and pions [43]. A Cerenkov detector is sensitive to the light that is emitted in a medium when a charged particle travels faster than the material's characteristic speed of light. In the CLAS detector the CC has a polar angle range of $\theta = 8°$ to $\theta = 45°$ with full azimuthal angle coverage (in correlation with the reach of the other detectors). This is achieved by covering as much space as possible with mirrors and placing light-collecting cones and photomultiplier tubes (PMTs) in the regions of ϕ that are obscured by the toroidal magnet coils (see figure 2-15).

Each of the six sector is divided in 2 regions in the azimuthal direction and then branched in 18 blocks in the polar direction. This gives a total of 216 light collecting modules, which consist of two focusing mirrors, a Winston light-collection cone with a PMT mounted at its base as well as a cylindrical mirror at the base of each cone (see figure 2-15). The
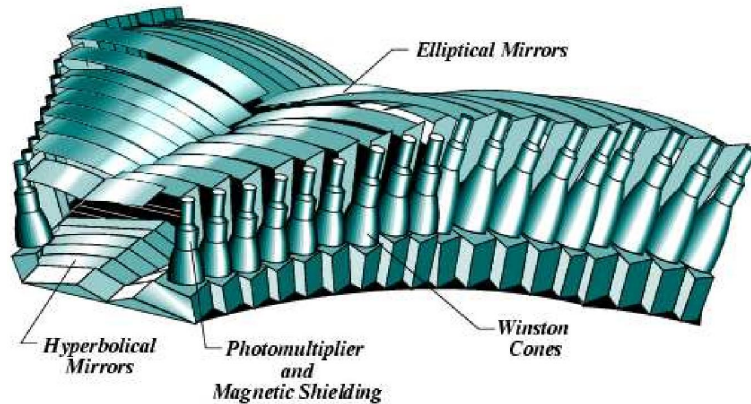
Figure 2-14: Cerenkov detector in CLAS. Here is shown a picture of its structure in each sector

reaction at the center axis of CLAS are characterized by cylindrical symmetry. Adding also the fact that the bending induced by the magnetic field from the Main Torus will just affect the polar angle of the trajectory, one can consider that the trajectories of the charged

particles lie approximately in planes of constant ϕ. From these considerations we can see how placing the PMTs in the shadows of the magnetic coils does not directly influence the angular coverage. T he CC is designed to just involve the azimuthal direction in order to not affect the polar angle information of the track.
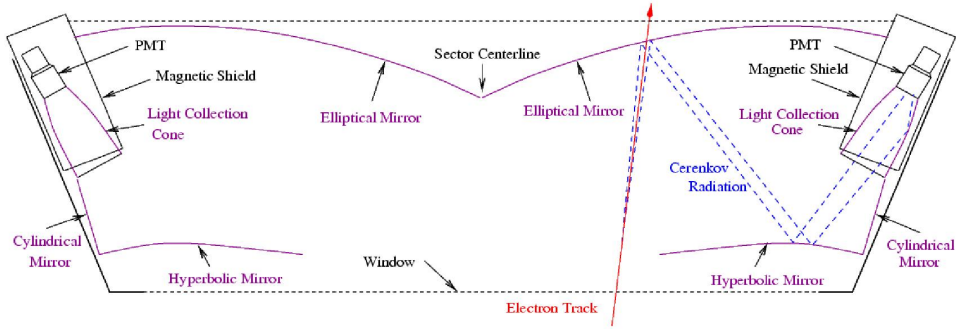
Figure 2-15: Cerenkov detector mirrors and light collecting scheme

2.2.5   Time of Flight system

In the CLAS detector, particle identification is obtained mainly combining the track/momentum data from the Drif Chambers with the information from the Time Of Flight (TOF) sensor. This detector consists of a group of scintillators positioned after Region 3 of the Drift Chambers, in the area between the Cerenkov detector and the Electromagnetic calorimeter, with a polar coverage of $\Delta\theta = 134°$ and full azimuthal extension(see figure 2-3). The scintillators are oriented approximately perpendicular to the track of the scattered particle [44]. To avoid influencing the tracking, like for the Cerenkov detector, the not active parts of the TOF are placed in the regions obscured by the magnet coils. There are 288 scintillators counters 5 cm thick. The forward counters are 15 cm wide and the large angle counters are 22 cm wide, giving an angular coverage of $\sim 2°$. Their length varies varies from 32 cm at the most forward angle to 450 cm at the large angles (see figure 2-16). The time resolution changes with the angle θ respect to the incoming beam line: It ranges from $120ps$

for $\theta < 90°$ to $250ps$ for angles $\theta > 90°$.
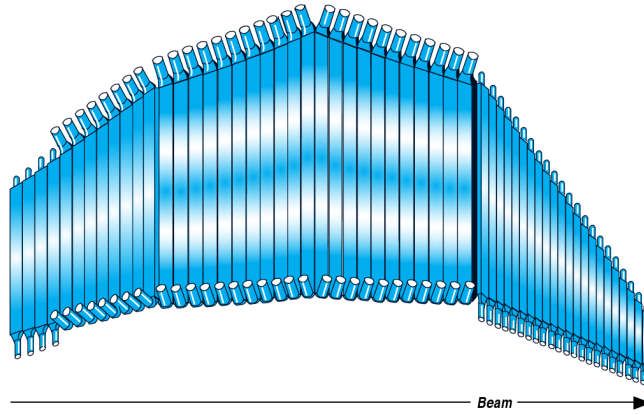
Figure 2-16: Time of flight detector in CLAS

2.2.6 EG2 Targets

The Eg2 experiment used two targets simultaneously to reduce the systematic error in measurements, as the Nuclear Transparency, that involved comparison of data from both the targets. The first target seen by the beam is the cryogenic liquid target (in this experiment was used liquid hydrogen and deuterium) $2cm$ long. The second target is a solid target of radius of $1.5mm$ (see table 2.1 and figure 2-17, 2-18).

	Material					
	Fe	C	Al (1)	Al (2)	Pb	Sn
Thickness (mm)	0.4	1.723	0.580	0.015	0.14	0.312

Table 2.1: Different solid targets used for the EG2 experiment are shown with their relative thickness

Figure 2-17: EG2 solid target holder
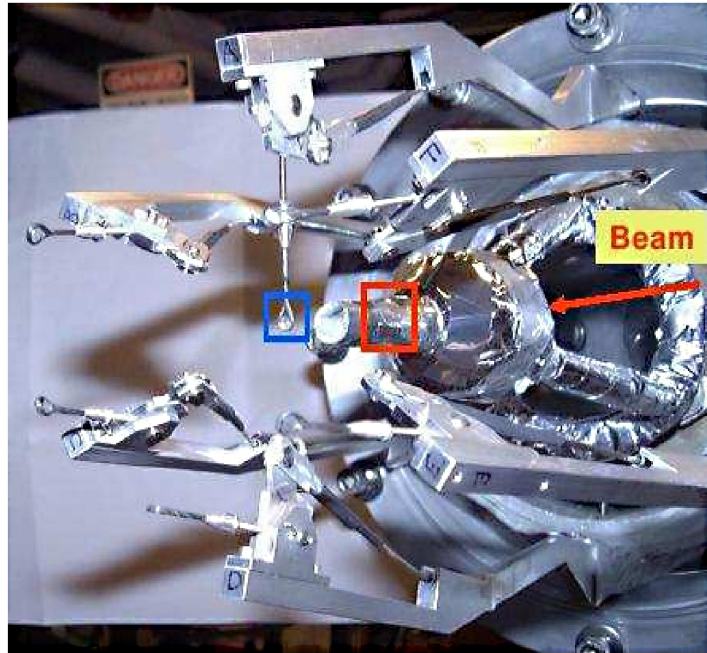
Figure 2-18: EG2 target holder. In blue is highlighted the liquid target; In red the solid target

2.3   Data Acquisition

When an event satisfies a particular trigger condition, the data from all the different detectors is recorded by the Data Acquisition (DAQ). For experiment as EG2, characterized by electron scattering, the signal that gives the trigger to the DAQ is the detection of an electron in the final state. This requirement is given by a contemporaneus hit in the Electromagnetic Calorimeter and in the Cerenkov detector above a selected threshold (Level 1 trigger).

A diagram that shows the structure of the DAQ system is shown in figure 2-19. After passing the pre-trigger discriminator, the signal from the detector is sent to the Level 1 trigger, that contains the information on the threshold requested in the experiment. The Level 2 trigger includes information from the Drift Chambers, but was not used in the EG2 experiment. When the requirements from Level 1 are passed. the information is sent to the Trigger Supervisor, which communicates with 17 Read-Out-Controllers (ROC). The data
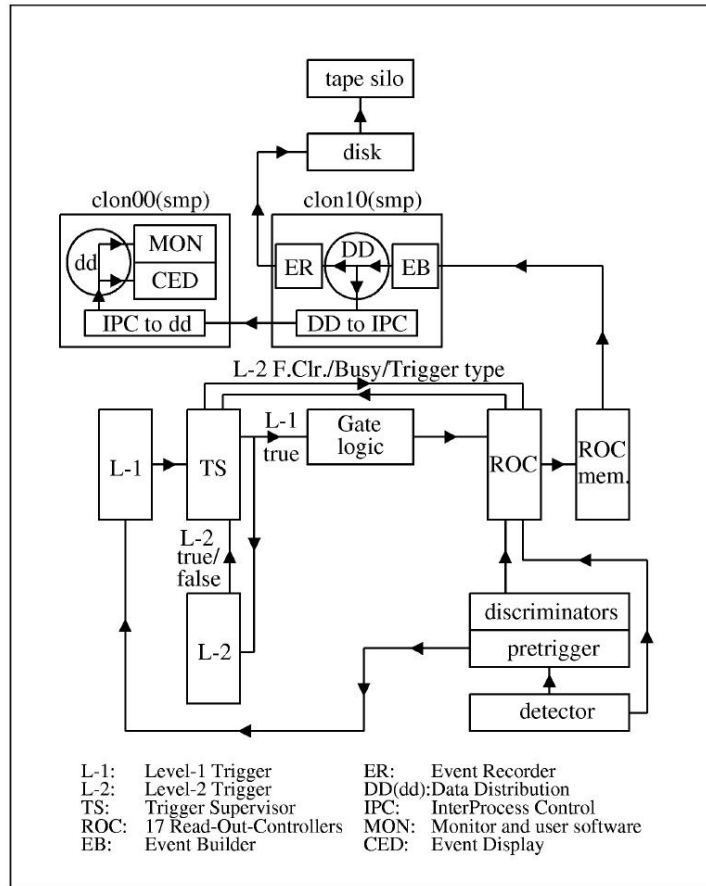
Figure 2-19: Schematic Diagram for the Data Acquisition system

here is then read and converted into digital information and sent from the ROC memory to the Event Builder (EB). From here the Data Distribution (DD) the events are sent to the on-line monitoring system and to the Event Recorder. In the on-line monitoring the data is checked doing a fast analysis on the event and studying the structure of the information given by each detector (for example checking for symmetries in the amount of data received from each sector of CLAS). The recording of the data is done in two steps: Firstly is written on a local disk (where one can do other monitoring that requires higher statistic) to be later transferred into tape at the data mass storage system of Jefferson Laboratory.

2.4 The data ensamble in the EG2 run

The Color Transparency search E02-110 [45] was part of the EG2 experiment and run in parallel with another research lead by W. Brooks E04-104 [46]. After a successful commissioning run in the summer of 2003 with a beam energy of 4.7 GeV, the targets of the EG2 experiment were moved backward respect to the center of the CLAS detector for having a better acceptance of negative charged particles. This movement restrict the forward solid angle not covered by the detectors, increasing the counts for the negative particles, that in the magnetic field used are bending towards the central axis of CLAS. The new position of the targets was $z \sim -30cm$ for the Liquid one and $z \sim -25cm$ for the Solid one. The full data taking resumed in December 2003 for going through March 2004. The down time in Autumn 2003 was caused by the hurricane Isabel that affected the area around the Tomas Jefferson Laboratory. This affected also the possible Q^2 range of the experiment, because the hurricane had an impact on the efficiency of many of the cavities of the continuous electron beam. For this reason the highest energy possible for the beam shifted from the expected $\sim 6GeV$ to $\sim 5.5GeV$. The full data-set consists of measurement of different target combinations at different energies. For a complete description of the experimental data obtained see table 2.2 and 2.3.

Beam Energy	Liquid Target	Solid Target	Number of events
4.0 GeV	^2H	Fe	~ 538.27 M
		C	~ 9.16 M
	empty	Fe	~ 0.40 M
		Al (1)	~ 12.35 M
		C	~ 17.93 M
4.7 GeV	^2H	Fe	~ 48.21 M
		Pb	~ 94.82 M
		None	~ 7.97 M
	empty	Fe	~ 0.80 M
		Pb	~ 0.40 M
		None	~ 1.59 M
	H_2	Fe	~ 14.74 M
		Pb	~ 111.96 M
		None	~ 0.80 M

Table 2.2: Different targets configuration used (see Table 2.1 for reference of the solid target) and electron beam energies delivered for the EG2 experiment of value of 4 GeV and 4.7 GeV are shown with their relative approximate number of events

Beam Energy	Liquid Target	Solid Target	Number of events
5.0 GeV	^2H	Fe	$\sim$ 2174.99 M
		Pb	$\sim$ 1453.05 M
		None	$\sim$ 11.95 M
		Al (1)	$\sim$ 8.77 M
		C	$\sim$ 1047.45 M
		Sn	$\sim$ 95.62 M
	empty	Fe	$\sim$ 9.96 M
		Pb	$\sim$ 8.77 M
		None	$\sim$ 0.80 M
		Al (1)	$\sim$ 231.88 M
		C	$\sim$ 8.77 M
		Al (2)	$\sim$ 9.96 M
	H_2	Fe	$\sim$ 59.36 M
		Pb	$\sim$ 75.70 M
		None	$\sim$ 60.56 M
		Al (1)	$\sim$ 20.32 M
		C	$\sim$ 14.74 M
5.5 GeV	^2H	Fe	$\sim$ 87.25 M
		None	$\sim$ 132.67 M
	empty	Fe	$\sim$ 4.78 M
		None	$\sim$ 14.34 M

Table 2.3: Different targets configuration used (see Table 2.1 for reference of the solid target) and different electron beam energies delivered for the EG2 experiment of value of 5 GeV and 5.5 GeV are shown with their relative approximate number of events

Chapter 3

REACTION IDENTIFICATION

The search for experimental evidence for Color Transparency is done in the Eg2 experiment investigating the Q^2 dependence for exclusive incoherent ρ^0 electron-production in a Nuclei(A scheme for this reaction is shown in figure 3-1). The Virtual photon γ^* fluctuates in a q, $\bar{q}$ pair , that will interact with one of the nucleons inside the nucleus and produce a ρ^0 meson. This will decay in a π^+ π^- pair.
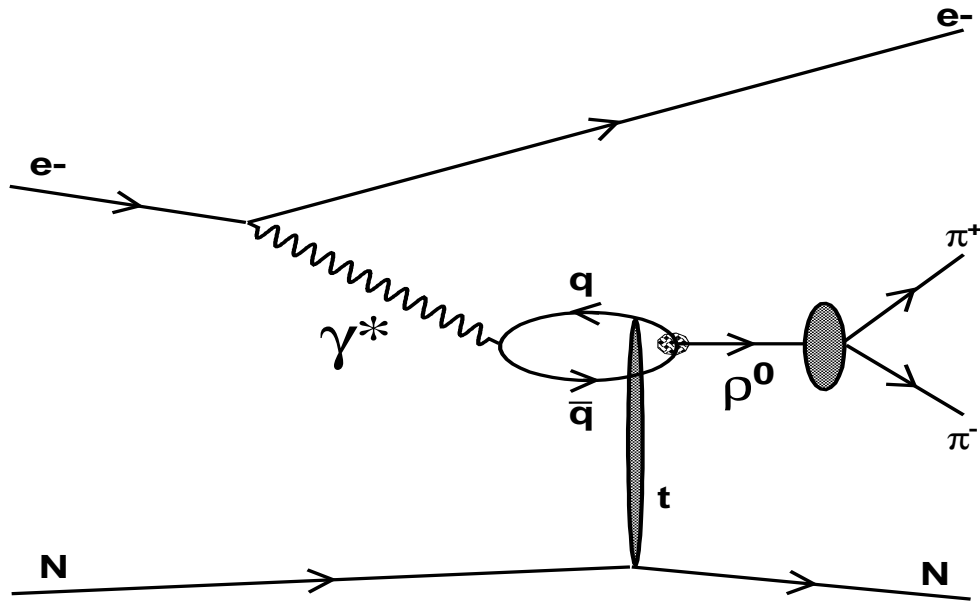
Figure 3-1: Reaction under study. The particle detected in the final state are the scattered electron and the π^+ , π^- pair.

The key points of this analysis will be:

- To define and study the mass distribution of the ρ^0. This will be determined using an invariant mass technique on the π^+ π^-.

$$M_{\rho^0} = \sqrt{(p^\mu_{\pi^+} + p^\mu_{\pi^-})(p_{\pi^+\mu} + p_{\pi^-\mu})} \tag{3.1}$$

- To determine the kinematics of the reaction one will need full knowledge of the γ^*. This information will be obtained from a comparison of the quadrimomenta of the electron beam and of the scattered $e-$.

3.1   Electron ID

To search for the scattered electron I analyzed the first track of the EVNT bank. The cooking procedure puts the particle that most likely have triggered the event in this position. For being considered as an electron we request on this particle three different type of cuts:

1. One that checks for good definition of the particle's signal in each detector;

2. One that rejects the pion contamination on this track;

3. One that rejects tracks from regions where the efficiency of the detector is not full.

3.1.1   Cuts on the track

For defining a good signal in the detector the following cuts have been used:

- $Status > 0$: To reject particles that passed the HBT (Hit Based Tracking), but failed the TBT (Time Based Tracking);

- $(DCstat, ECstat, SCstat, CCstat) > 0$: To consider particles where are involved the following detectors: Drift Chambers, Electronic Calorimeter, Time of Flight, Cerenkov Counters

- $charge = -1$: To require that the charge of the particle is the same as that of the electron.

3.1.2 Pions rejection

Information from the Cerenkov Counters and the Electronic Calorimeter are used for rejecting the pions from the first track:

1. Cerenkov Counters : We Consider the momentum distribution of the π^- produced in our experiment and analyze the momentum dependence of the Number of photo-electrons detected in the Cerenkov Counters (See figure 3-2 .The pions will give a signal centered around a few photo-electrons). The cuts applied on the Number of photo-electrons (N_{phe}) depend on the momentum of the track (p):

$$p < 2GeV \ and \ N_{phe} \times 10 > 25 \tag{3.2}$$

$$or \ p \geq 2GeV \ and \ N_{phe} \times 10 > 5$$

2. Electronic Calorimeter : The Energy deposited in the Electromagnetic Calorimeter can be view summing the reading from all the 13 EC layers (E_{tot}) or considering the separate reading from two groups of 5 layers (EC_{in}) and 8 layers (EC_{out}) to obtain longitudinal information. Analyzing the plot in figure 3-3 one can see that, because in this data the trigger has an EC total energy threshold of $0.172GeV$, there is a considerable decreasing of electron for $E_{tot} < 0.172 \Rightarrow EC_{out} < 0.172 - EC_{in}$. The pion contamination is visible as a sharp peack in the energy deposited in the inner part for energy below our threshold. This peack has a long energy tail that is detected in the outer region of the EC (for more information see [41]). For these reasons the following cut was applied:

$$E_{in} > 0.05GeV \ , \ E_{out} > 0.172GeV - 1.2 \, E_{in} \tag{3.3}$$

A further cut was also decided on the plot in figure 3-4 : Because the sampling fraction (which states the approximate fraction of the particle's energy which will be observed in this detector), one is expected to have for electrons a value of $\frac{EC_{tot}}{p} \sim 0.27$. For this reason, a $\pm 3\sigma$ cut around the central peak (~ 0.27) was placed for the distributions
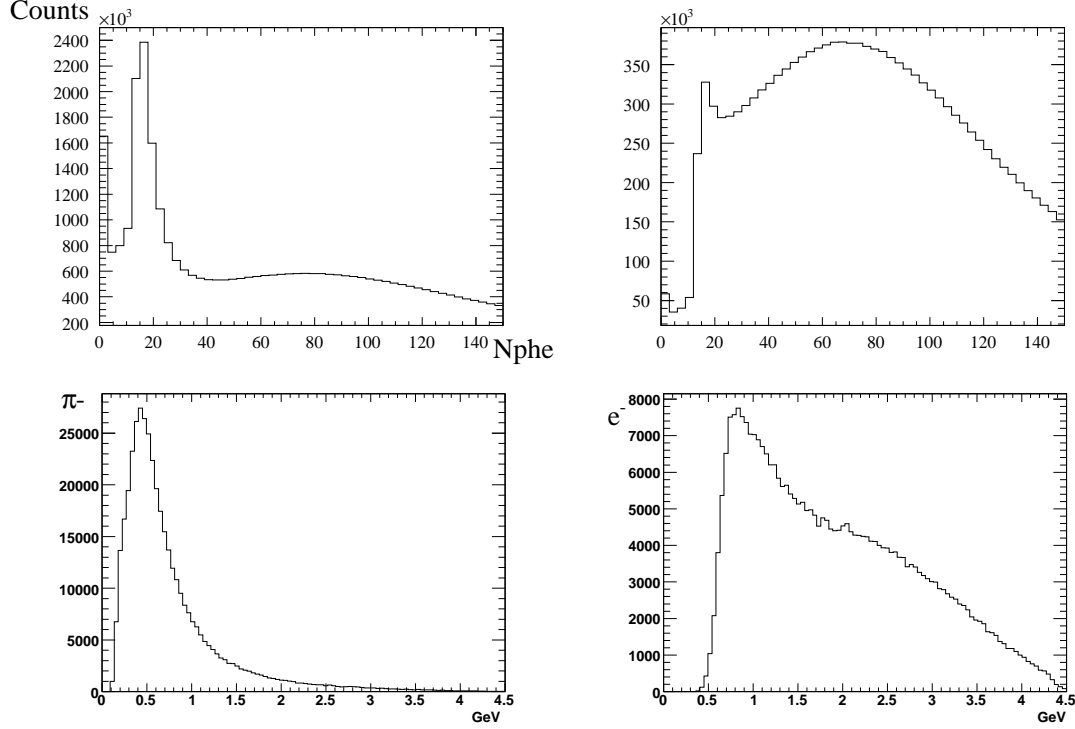
Figure 3-2: On the top part is plotted the Number of photo-electron produced in CC multiply by 10 for 2 different momentum range ($p < 2.0 GeV$ on the left and $p > 2.0 GeV$ on the right) for enhancing the fact that the main part of the pion contamination is for $p < 2.0 GeV$. One can compare the different momentum distribution for π^- (on the right) and e^- (on the left) in the 2 lower plots.

of EC_{tot} obtained at constant momentum p. For defining the region of this cut , the distribution of figure 3-4 was "sliced" with constant momentum range and then fitted with a Gaussian. In this way one can determine the center of the distribution and the relative σ. The 3σ points where then fitted as a function of the electron momentum (see figure 3-4). The final cut applied is:

$$\frac{EC_{tot}}{p} > 0.220 - 0.260 \, e^{-0.672 GeV^{-1} \, p} + \frac{0.0616 GeV}{p} \tag{3.4}$$

$$\frac{EC_{tot}}{p} < 0.350 + 0.0326 \, e^{-0.553 GeV^{-1} \, p} + \frac{0.00209 GeV}{p}$$

3.1.3 Cuts on region of not full efficiency

The Electronic Calorimeter is composed of different sections (see chapter 2.2.3 of this document for more information). Each section has the shape of an equilateral triangle and
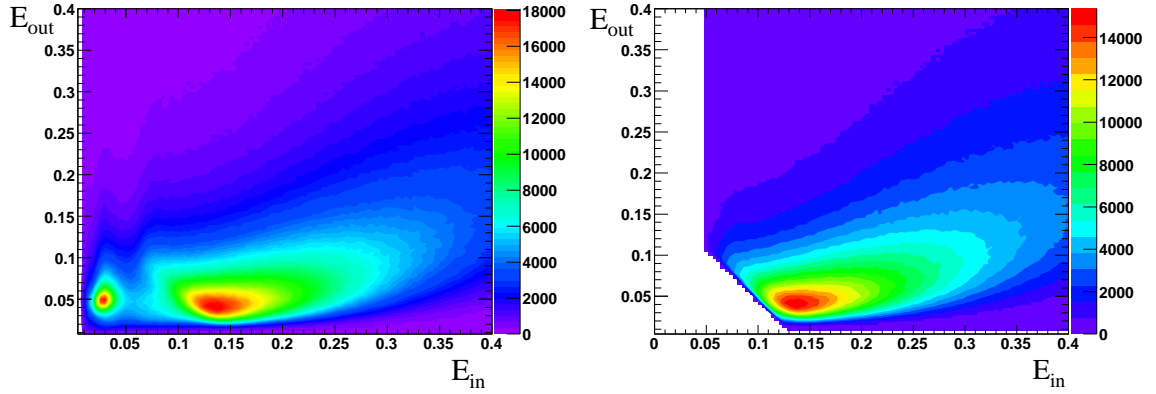
Figure 3-3: E_{out} vs E_{in} plot before (left) and after (right) EC cut
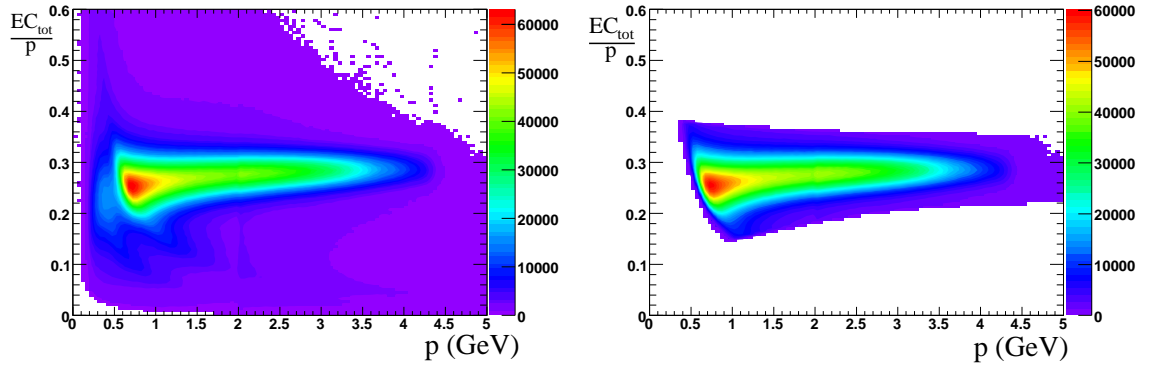
Figure 3-4: $\frac{EC_{tot}}{p}$ vs p plot before (left) and after (right) 3σ cut

the sides of this triangle (parallel to the scintillator strips that carry the signal) are labeled u, v, w. Considering that the signal on this detector is composed of an electromagnetic shower (a signal that occupies more than a single strip), the information detected cannot be trusted with a good confidence level if it is close to the sides of the triangle. For avoiding redundancies, just a single cut on each of these plain/coordinate (u, v, w) is needed (see figure 3-5):

$$u \geq 40 \tag{3.5}$$

$$v \leq 360$$

$$w \leq 395$$
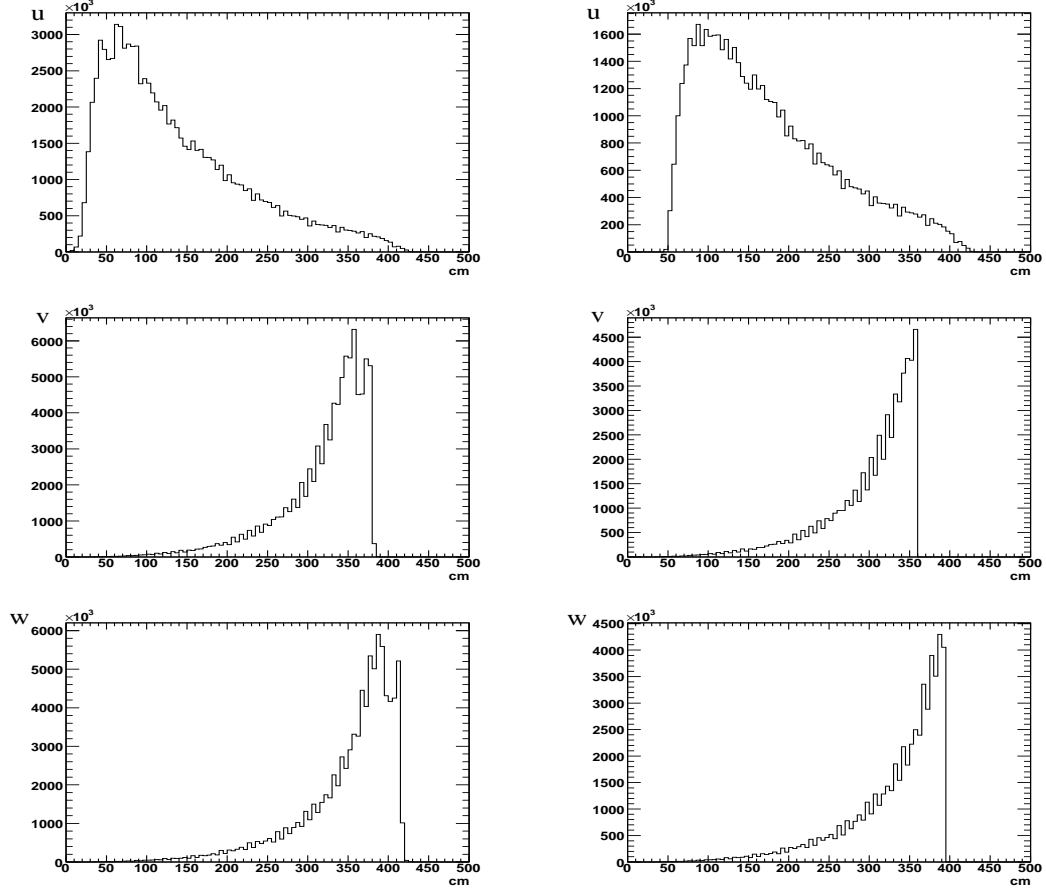
Figure 3-5: From Top to Bottom, respectively EC u, v and w coordinate before (left) and after (right) the cut defined in 3.5

3.2 Pions ID

Well identifying pions and separating their signal from the one of electrons is one of the important tasks in this experiment. Different series of cuts have been decided to better recognize the signal from π^+ and π^-.

3.2.1 Identification of π^+

To identify the track of a π^+ the following cuts have being used:

- $Status > 0$: To reject particles that passed the HBT (Hit Based Tracking), but failed the TBT (Time Based Tracking);

- $(DCstat, SCstat) > 0$: To consider particles where all these detectors are involved:

respectively Drift Chambers and Time of Flight

- $charge > 0$: To require that the charge of the particles is the one of a π^+ .

- The β of the particle was determined using two different ways:

  1. Using information of the track's momentum, one can determine the speed of the particle (assuming that is really a pion) by $\beta_{\pi+} = \frac{p_{\pi+}}{\sqrt{p_{\pi+}^2 + m_{\pi+}^2}}$;

  2. Using togheter the information on the length of the particle's path ($l_{\pi+}$) and its time of flight (t_{TOF}), one can also directly measure the β as $\frac{l_{\pi+}}{t_{TOF}c}$.

One can then compare the values so obtained plotting their difference $\Delta\beta$ as a function of the track's momentum. The π^+ distribution will be shown as a peack around the x axis, which represents points characterized by $\Delta\beta \sim 0$ (see figure 3-6)
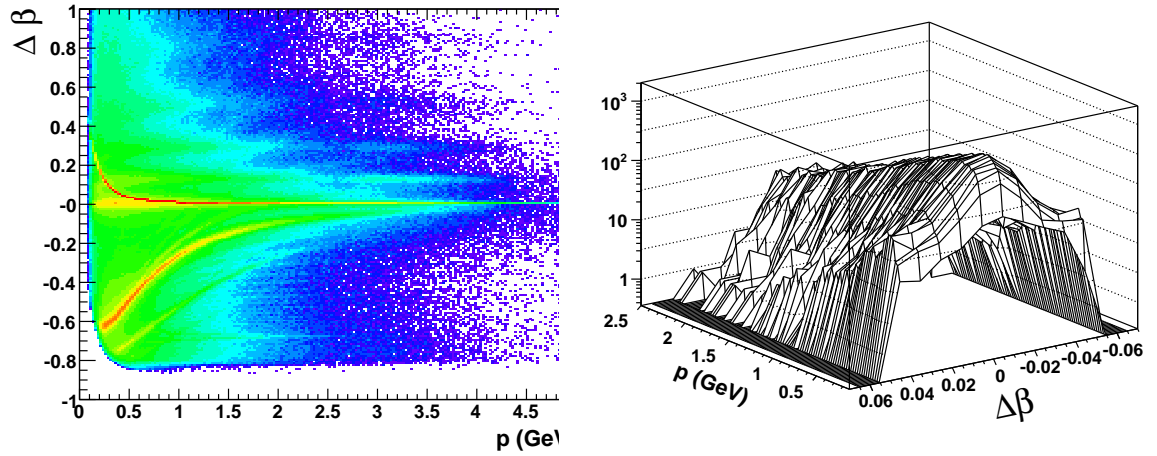
Figure 3-6: $\Delta\beta$ is plotted here as a function of the track's momentum p express in GeV. A cut has been placed around the x axis ($|\Delta\beta| < 0.05$). The result of the cut shown in the picture on the right. The points at $|\Delta\beta| = 0.05$ represent the $\pm 2\sigma$ cut for the distribution determined at constant momentum and centered around $|\Delta\beta| = 0$

$$|\Delta\beta_{\pi+}| < 0.05 \tag{3.6}$$

- To identify pions with momentum $p > 2.5 GeV$ we consider information obtained from the Cerenkov detector. At this energies we know that the pions will have enough

speed to fire the Cerenkov detector. More massive particles, as kaons and protons will not already pass the speed of light of the medium and will not produce a distinct Cerenkov signal. For this reason we require (where N_{phe} represents the Number of photo-electron produced in the Cerenkov detector):

$$if \ p > 2.5 GeV \ \Rightarrow \ N_{phe} \times 10 > 25 \tag{3.7}$$

- This track is supposed to fail the positron ID (defined in the same way as the electron, with the difference that now the required $charge = +1$)

3.2.2 Identification of π^-

To identify the track of a π^- the following cuts have being used:

- $Status > 0$: To reject particles that passed the HBT (Hit Based Tracking), but failed the TBT (Time Based Tracking);

- $(DCstat, SCstat) > 0$: To consider particles where all these detectors are involved: respectively Drift Chambers, Time of Flight

- $charge < 0$: To require that the charge of the particle is the one of an electron.

- As for the π^+ we determine the β of the particle using two different ways:

  1. Using information of the momentum of the track, one can determine the speed of the particle, $\beta_{\pi+} = \frac{p_{\pi+}}{\sqrt{p_{\pi+}^2 + m_{\pi+}^2}}$;
  2. Using togheter the information on the length of the particle's path ($l_{\pi+}$) and its time of flight (t_{TOF}), $\beta = \frac{l_{\pi+}}{t_{TOF}c}$.

One can then compare the values obtained plotting their difference $\Delta\beta$ as a function of the track's momentum. The $\pi-$ distribution will be shown again as a peack around the x axis, which represents points characterized by $\Delta\beta \sim 0$ (see figure 3-7)

$$|\Delta\beta_{\pi^-}| < 0.05 \tag{3.8}$$
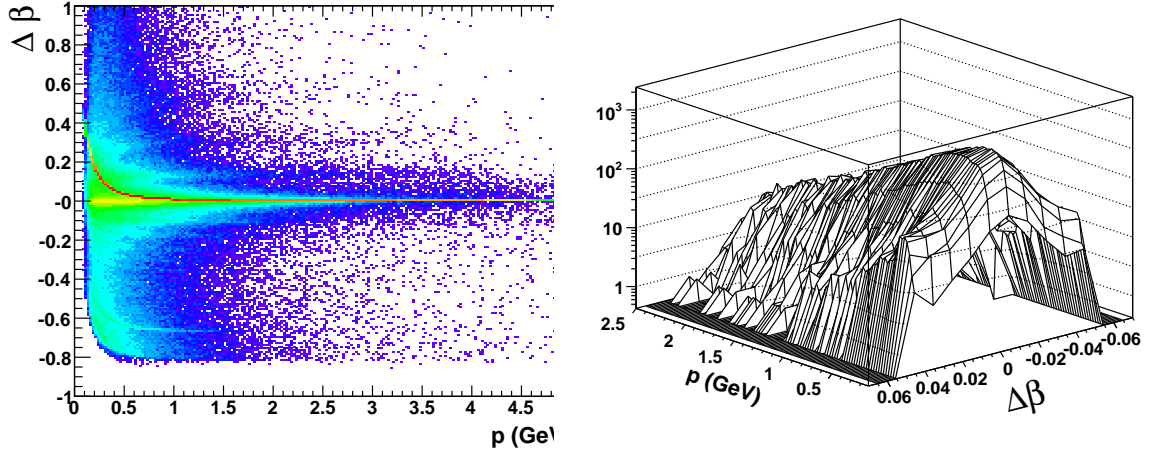
Figure 3-7: $\Delta\beta$ is plotted here as a function of the track's momentum p express in GeV. A cut has been placed around the x axis ($|\Delta\beta| < 0.05$). The result of the cut shown in the picture on the right. The points at $|\Delta\beta| = 0.05$ represent the $\pm 2\sigma$ cut for the distribution determined at constant momentum and centered around $|\Delta\beta| = 0$

- As for the π^+ we require a cut using the Cerenkov detector for pion characterized by higher energy

$$if \ p > 2.5 GeV \ \Rightarrow \ N_{phe} \times 10 > 25 \tag{3.9}$$

- The track needs to fail the electron ID (as described in this chapter).

3.3 Extraction of the ρ^0 distribution

After having identified each particle in our reaction (see figure 3-1), we can proceed now in extracting the mass distribution for the ρ^0 vector meson. The following requirements have been used to disentangle the signal of the ρ^0 from other processes.

1. We are selecting only events with:

   - Number electron $= 1$ and as first particle in the EVNT bank

   - Number of $\pi^+ = 1$

   - Number of $\pi^- = 1$

   - Number of positron $= 0$

2. We require a vertex cut: Electron, π^-, π^+ (See figure 3-8) needs to have vertexes from the same target.
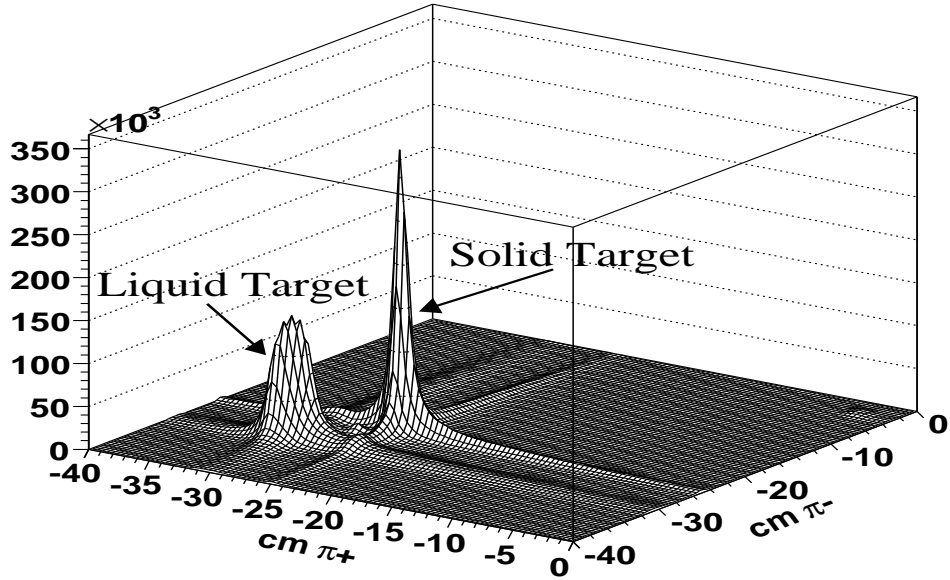
Figure 3-8: Histogram of the Z Vertex position for the π^+ and π^-. One can easily distinguish between the Solid and Liquid Target

To have selection for the target in the electron track, we use a cut the will be dependent on which sector of CLAS detects the electron. In this way we can avoid problem due to beam instabilities and to misalignment of the beam or of particular detectors.

3. At this step we can find the mass of the ρ^0 using an invariant mass technique on the π^-, π^+ (using momentum conservation on the ρ^0 decay's products). At this step the invariant mass distribution is far from the expected Lorentz behavior (see figure 3-10).

4. At this point we can use different kinematical cuts for "cleaning" the ρ^0 distribution. The first cut will be $W > 2\,GeV$ and is done to avoid the resonance region (see figure 3-12). The definition of W is (see figure 1-1 and equation 1.2 at page 4):
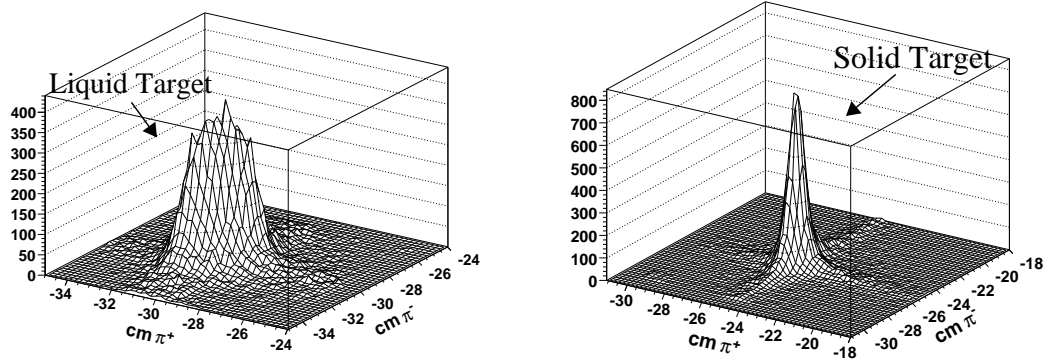
Figure 3-9: After we require that the event has an electron with vertex correspondent to one of the two targets, the selection of the target for π^+ and π^- from the same event results easier. In these plots are shown the vertexes distribution for π^+ and π^- after we already have applied our cut for the electron track

$$W = \sqrt{M_{pr}^2 + 2\,M_{pr}\,\nu - Q^2} \tag{3.10}$$

5. The second kinematical cut will be $(0.1\,GeV^2 < -t \leq 0.4\,GeV^2)$ (see figure 3-13). t represents the invariant square of the momentum transfer with the target and is defined as:

$$t = -(p_{\gamma*}^\mu - p_{\pi+}^\mu - p_{\pi-}^\mu)^2 \tag{3.11}$$

Where $-t > 0.1 GeV^2$ is for excluding coherent production off the nucleus; $-t < 0.4 GeV^2$ is for still being in the diffractive region.

6. The last kinematical cut is done to select the elastic part of the mass spectrum. This is done selecting Energies of the vector meson ρ^0 which don't differ too much from the energy of the incoming γ^*. To this purpose we introduce a variable z defined as

$$z = \frac{E_{\rho^0}}{\nu} \tag{3.12}$$

We will consider in our analysis ρ^0s which satisfy $z > 0.9$.

After these kinematical cuts, the Invariant Mass distribution for the combination of π^-, π^+ will assume a Lorentz like behavior, as was expected for the ρ^0 (see figure 3-11) with the
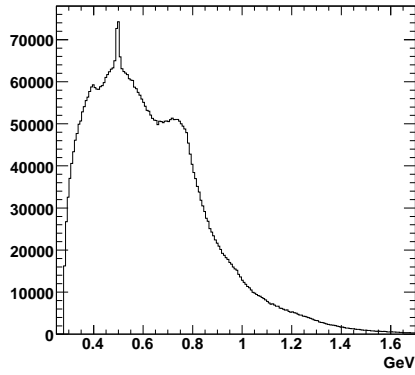
Figure 3-10: Invariant mass from the reconstructed π^+ and π^- for the Liquid target before kinematical cuts
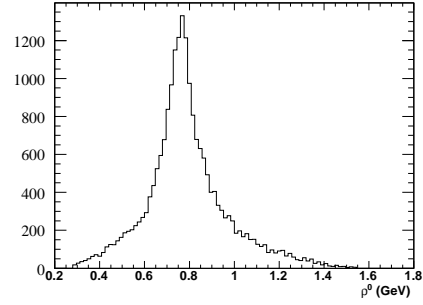
Figure 3-11: Final ρ^0 distribution for full Q^2 range

addition of a small background contribution. To determine the shape of the still present

background we will use simulated events, as will be described in Chapter 5.
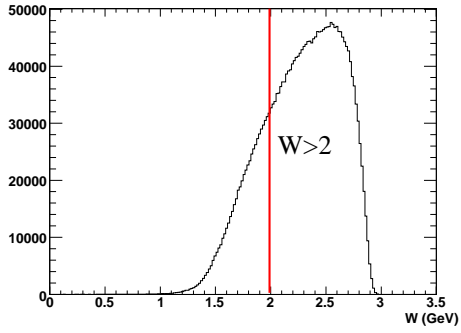
Figure 3-12: $W_{el} > 2 GeV$ to avoid the resonance region
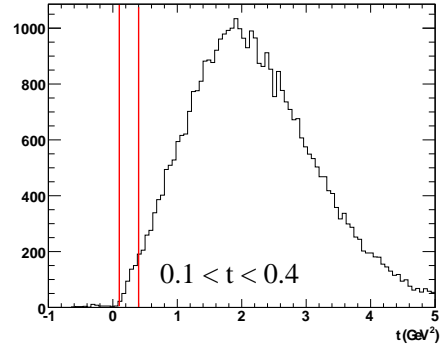
Figure 3-13: $0.1 \, GeV^2 < t < 0.4 \, GeV^2$ to select the elastic and diffractive process and exclude coherent production
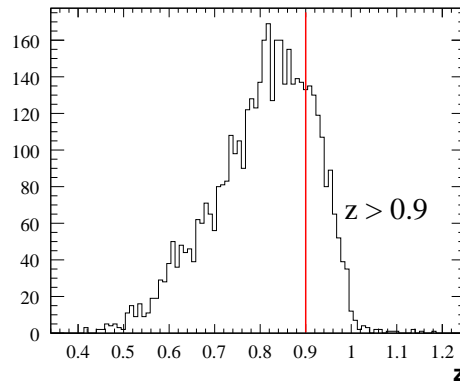
Figure 3-14: $z > 0.9$ to select the elastic process

Chapter 4

FIDUCIAL CUT

4.1 Motivation

The CLAS detector is considered, for a starting analysis, as a full 4π detector, able to cover with the same efficiency and accuracy the full solid angle. In reality, being a system composed of different parts and detectors, its acceptance is not the same in every region. One of the detectors most affected is the Electronic Calorimeter, a detector mainly used for the identification of the scattered electron. Because this detector analyzes 'showers' of hits, also a starting analysis will need a regional cut for taking care of its response. For this purpose a cut directly on the coordinates on the surface of the EC (cut in u,v,w), is normally use as a starting procedure. For a more deep knowledge of the full CLAS detector, a detailed analysis of the respond of the detector for every single particle is needed. This is done using a procedure called Fiducial Cut, where are defined the region in which the data can be trusted with a good confidence.

4.2 Previous Method

The previous method was developed by D. Protopopescu ([1]). The method that I will be using is a slight evolution from his study and will be explained in the next section. In both methods the fiducial cut is structured to be a function of :

- particle type

_____

[1] see http://nuclear.gla.ac.uk/clas/e2doc/FiducialCuts/fc4E2.html for further explanations

- particle momentum p

- particle polar angle θ

- particle azimuthal angle φ , that will also give information on the sector of the detector in which the particle hits

For every single particle type, a plot of the angle distribution for different momentum bins is created for every sector. This distribution is then sectioned and studied as shown in figure 4-2. The distribution found , because the reaction does not have a ϕ dependence, will theoretically appear as a flat distribution for every single $\theta = const$ plot. The fact that every sector is a separate detector causes the distribution to look like a central plateau, where the apparatus works 100%, and an external region, where the acceptance is not full. To simulate this distribution and find its edges, a trapezoidal fit is used. The edges of the distribution where the accepance in the detector is full are then defined as the ϕ coordinate of the minor basis of the trapezoid. The error on these edges is defined as a fraction of the distance of these edges to the major basis ϕ coordinates(see figure 4-3). The ditribution of these edges is then fitted with a curve (see equation 4.1 and check figure 4-1 for an example), that will have the information on the fiducial cut for every single momentum bin and sector of the detector.

$$\text{if } (\theta < \theta_{min} \text{ or } \theta > \theta_{max}) \implies \quad \phi = 60(Sector - 1) \tag{4.1}$$

$$\text{else} \implies \quad \phi = 60(Sector - 1) + (Side)\, a \left(1 - \frac{1}{\frac{\theta - \theta_{min}}{b} + 1}\right)$$

Where θ_{min}, a, b are the free parameters,θ_{max} is set to a default value for every single particle, $Side$ $(= \pm 1)$ will switch between the upper and lower part (check(figure 4-1) for an example).

This fit is done so that only the parameters store the requested information for a single momentum bin. These parameters, for every single sector and particle will then be plotted as function on the momentum and fitted with polynomial curves. These curves will then be
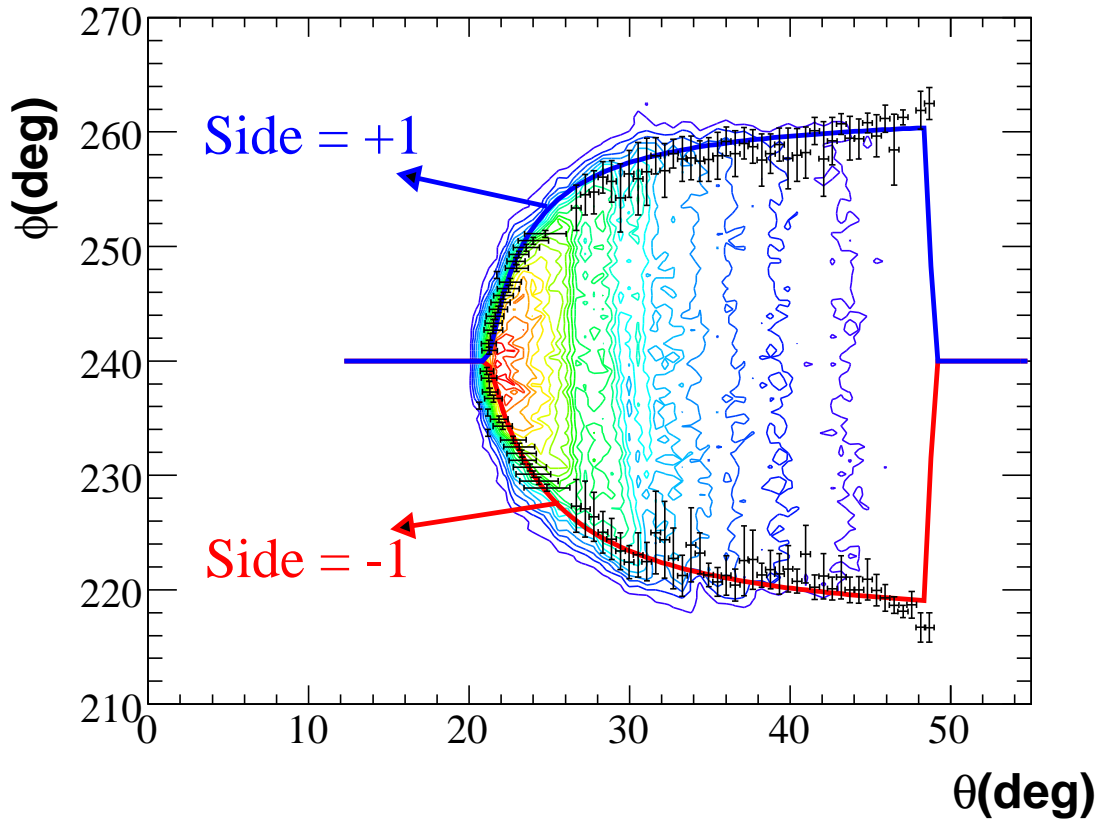
Figure 4-1: Example of the fitted function that defines for simplicity my fiducial cut for every momentum and sector. The red and blue show the 2 different sides of the function, as in equation 4.1.

used in my analysis for defining the Fiducial cut by determining for any particle's momentum vector the corresponding parameters (θ_{min}, a, b) that define my region of good confidence (See figure 4-9).

4.3 New method

My method is a slight evolution of the previous one. I have tried to make improvements in:

1. The poor definition of the edge using a $\theta = const$ picture for the region where the points on the border of my fiducial cut have $\Delta\phi > \Delta\theta$. In this case my determination of the edge will be affected by my bin size in θ, that will give a systematic shift of my
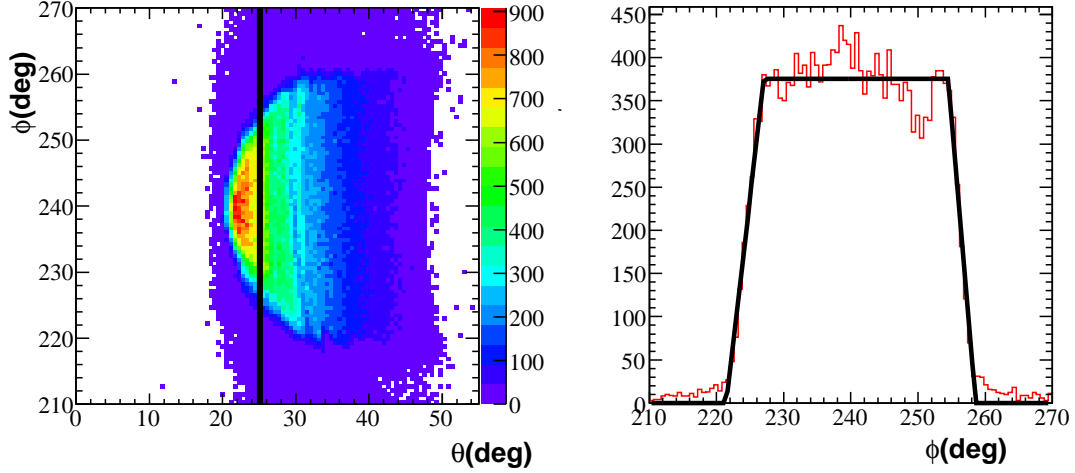
Figure 4-2: Example with previous method. On the left side is shown the contour plot of the hit distribution (plot θ vs. φ) of electrons with energies between $1.15 GeV \leq E < 1.25 GeV$ that are counted in the 5th Sector. On the right side is show the Y projection of this distribution for $27.5° \leq \theta < 28°$. The edges of the distribution are defined using a trapezoidal fit.

   fiducial cut versus the center of the distribution (see figure 4-8 for an example)

2. The fact that using a polynomial fit for describing the momentum dependence of each parameter that defines the fiducial cut could move each parameter away from its physical value.

To solve these problems, the following is being done:

1. The contour distribution that defines the edges has been analyzed in 2 different ways. In the internal region (red zone in the figure 4-4), where the points on the border are characterized by $(\Delta\phi > \Delta\theta)$, a more accurate picture is created by a $\phi = const$ approach (see figure 4-5). To describe the distribution and finding the point that describes consistently the edge of my fiducial cut, I have used a function constructed with two Gaussian curves, characterized by the same center of distribution but different σ
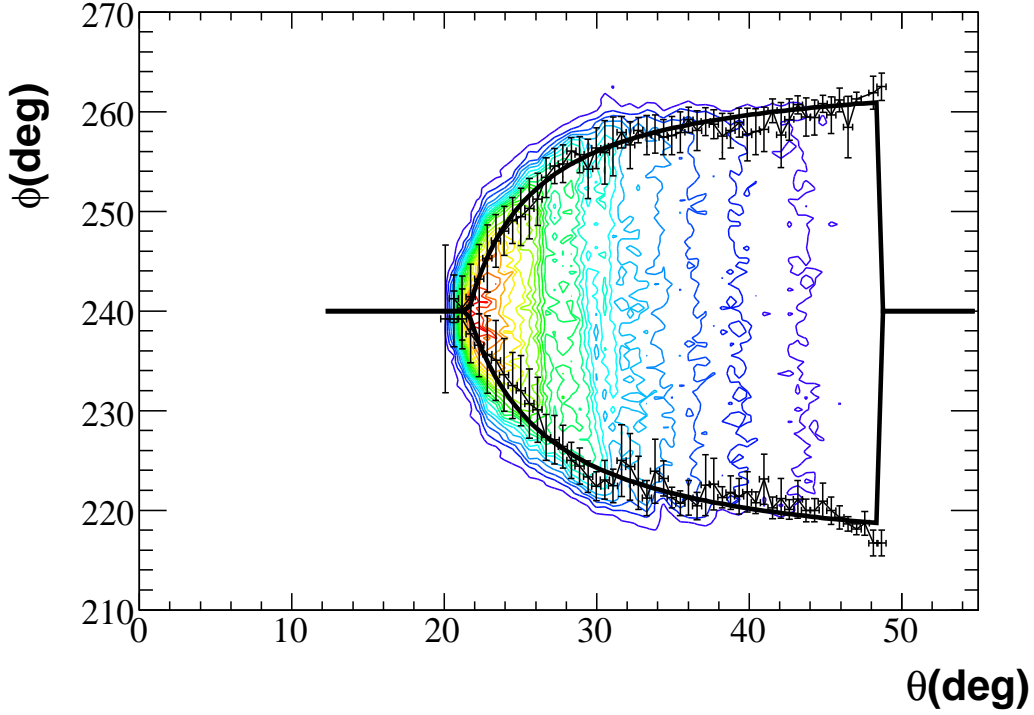
Figure 4-3: Example with previous method. On the plots are shown the edges and their errors.

(see equation 4.2). The error is defined as σ_1

$$
\begin{aligned}
&\text{if}(\theta \leq \mu) &\qquad y &= A\,e^{-\frac{(\theta-\mu)^2}{2\sigma_1^2}} &\qquad (4.2)\\[2ex]
&\text{else} &\qquad y &= A\,e^{-\frac{(\theta-\mu)^2}{2\sigma_2^2}}
\end{aligned}
$$

where $A, \mu, \sigma_1, \sigma_2$ are my free parameters. For the external part (the blue zones in figure 4-4), because the edges follow a path with $(\Delta\phi < \Delta\theta)$ we can still use a $\theta = const$ approach (see for example figure 4-2).

2. To solve some issues that were created by the use of a polynomial fit, more appropriate functions that better follow the behavior of each parameter where used for each different particle. For example equation 4.3 shows the expressions of the parametric functions for θ_{min} on π^- (figure 4-7 shows the results in Sector 5).In equation 4.3 and

in the following ones , *mom* represent the particle's momentum.

$$\theta_{min} = p_0 + \frac{p_1}{mom^2} + p_2\, mom + \frac{p_3}{mom} + p_4\, e^{p_5\, mom} \qquad (4.3)$$
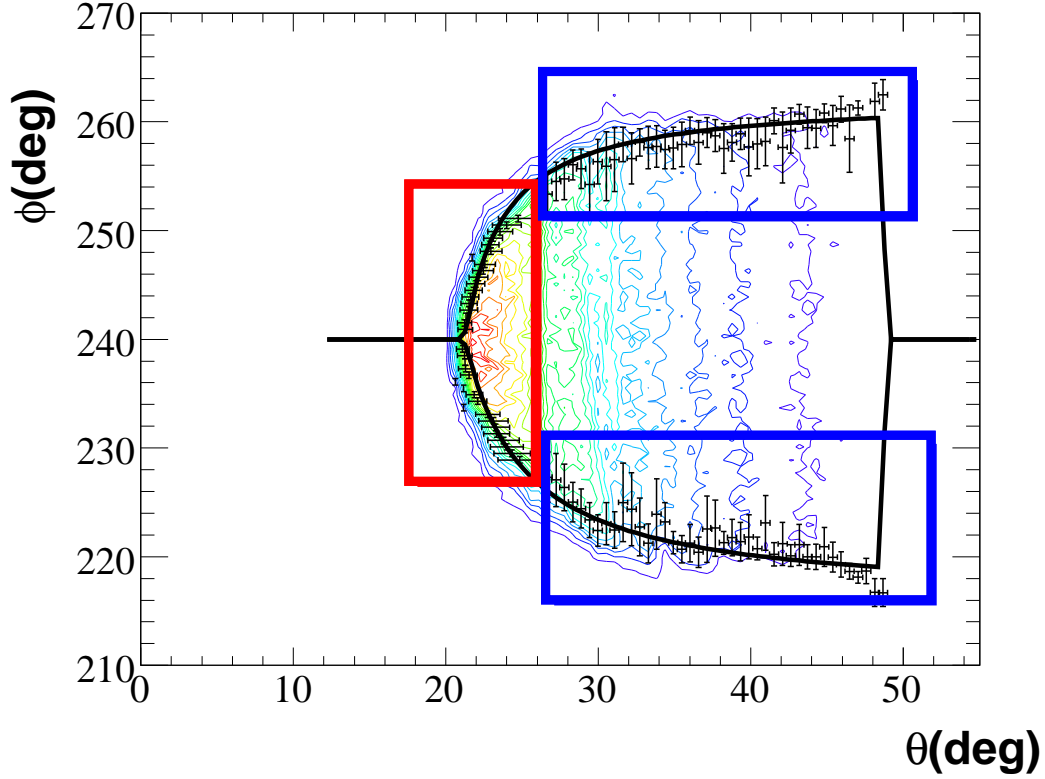
Figure 4-4: An example of contour where the edges for fiducial cut are defined using a $\phi = const$ in the red zone, and a $\theta = const$ in the blue zones.
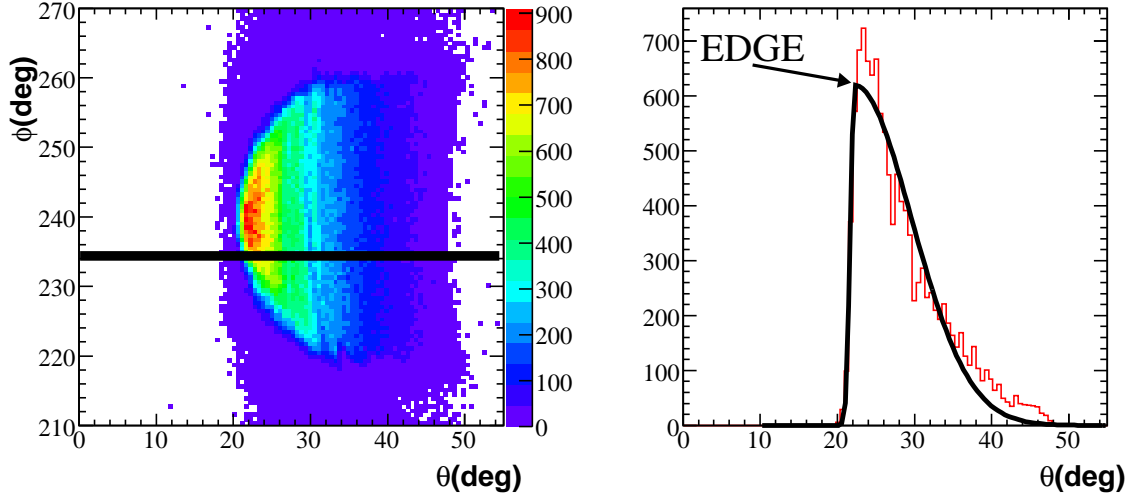
Figure 4-5: Example with new method. On the left side is shown the contour plot of the hit distribution (plot θ vs. φ) of electrons with the same ranges as in figure 4-2. On the right side is the Y projection of this distribution for $234° \leq \varphi < 234.6°$. The edge of the distribution is defined using $\phi = const$ as in the picture.

4.4   Results

Using this procedure a fiducial cut was developed and applied to my distributions. One example of the changes followed is in figure 4-9. In the tables 4.1, 4.2, 4.3, 4.4, 4.5, 4.6, 4.7, 4.8 and 4.9 are reported the values of the parameter functions (see equation 4.1) found for different particles and energies. These functions used are divided into two groups, due to a different behavior in their momentum dependence.

- The following functions were used for electron and π^+:

$$a = p_0 + p_1\, e^{p_2(mom - p_3)} \tag{4.4}$$

$$b = p_0 + p_1(mom)\, e^{p_2(mom - p_3)^2}$$

$$\theta_{min} = p_0 + \frac{p_1}{mom^2} + p_2\, mom + \frac{p_3}{mom} + p_4\, e^{p_5\, mom}$$
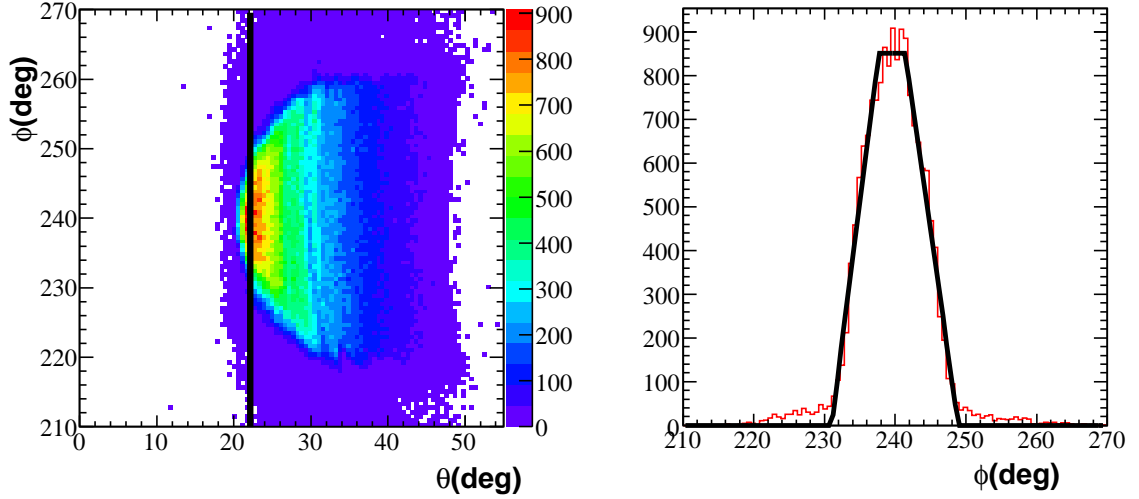
Figure 4-6: Same point with the old method. The definition of the edges are slightly affected by the binning size in θ, because their distribution is mostly parallel to the direction where we are inspecting it (the line at constant θ).

- For π^-:

$$a = p_0 - p_1 \, arctan(p_2(mom - p_3)) \tag{4.5}$$

$$b = p_0 + p_1(mom) \, e^{p_2(mom-p_3)^2}$$

$$\theta_{min} = p_0 + \frac{p_1}{mom^2} + p_2 \, mom + \frac{p_3}{mom} + p_4 \, e^{p_5 \, mom}$$

A test for a Fiducial cut with a target filter for the particle under observation was also done. The difference of the distribution found for the 2 cases was consistent with a shift from one target to the other, but remains inside the error-bar definition of the edge of the particle distribution. So, filtering the data with a target cut did not give further information, but did diminish the single statistic from which the single cut was developed: so was decided to only use it as a further check on the analysis.

For a more detailed picture of the Fiducial cuts for the eg2 experiment check also

`http://physics.unh.edu/~lzana/Fiducial_cut/50GeV/`

where a detailed representation of every single step explained in this chapteris available.
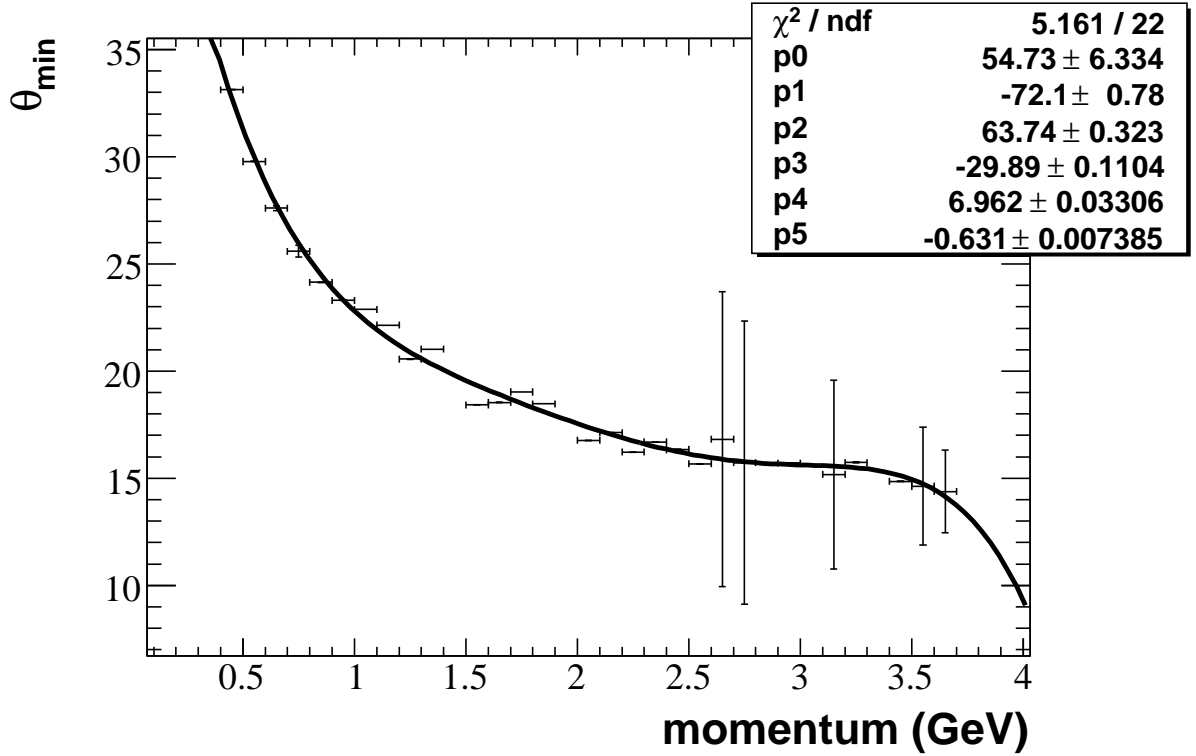
Figure 4-7: Distribution and relative fit for θ_{min}, using the function defined in equation 4.3.

4.5   Cherenkov Efficiency

The Cherenkov detector efficiency, as a function of the momentum vector of the electron has a complicated behavior on θ_e and ϕ_e for the edges of each sector. One can see for example how in figure 4-10 the efficiency has an irregular shape for a low θ_e. In this plot, for enhancing this behavior, the Geometrical cuts on the physical coordinate on the EC detector (u,v,w cut in the definition of the electron in the particle id) was removed. The Fiducial Cut previously developed eliminates from our analysis those regions that will be difficult to study.
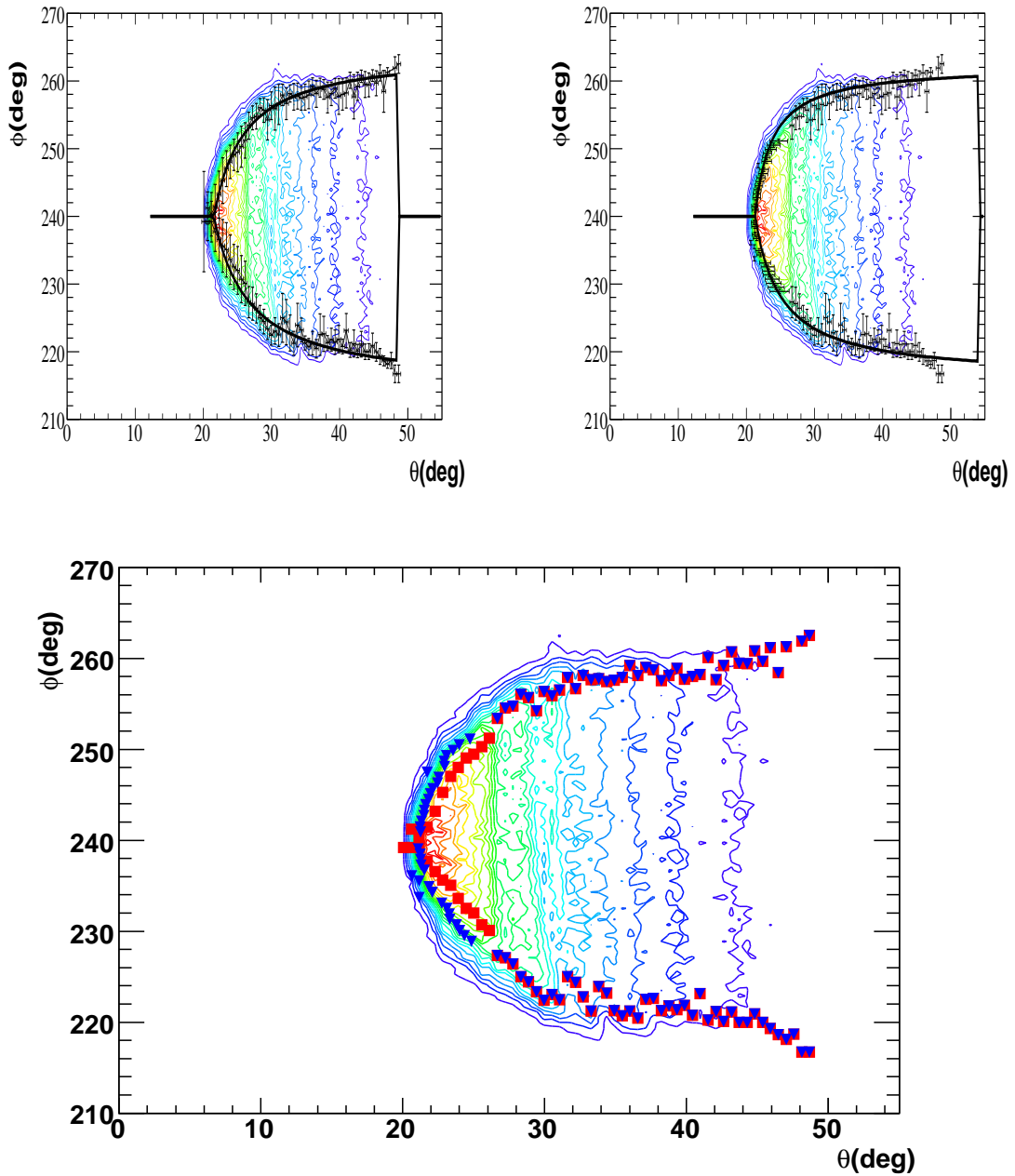
Figure 4-8: On the top left is shown the definition of the edges using only $\theta = const$ plots. On the top right the position of the edges are implemented using $\phi = const$ plots in the central region. At the bottom the difference of the 2 approaches: In red are shown the edges, using only $\theta = const$, in blue using also $\phi = const$ plots in the central region
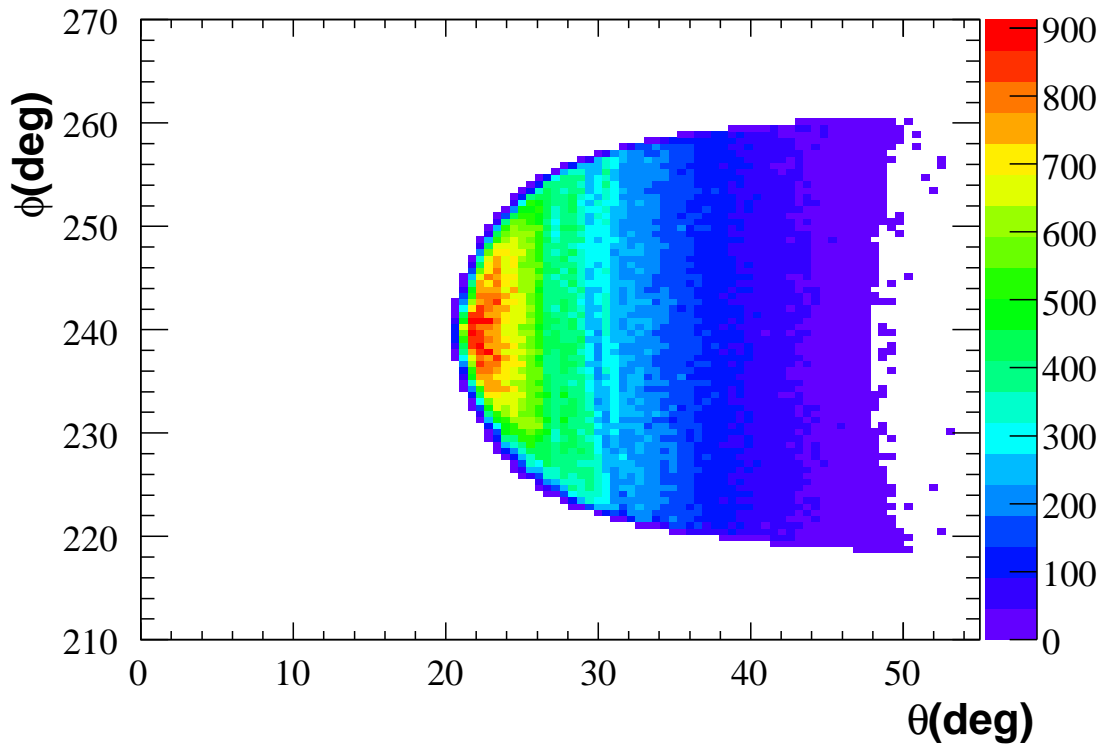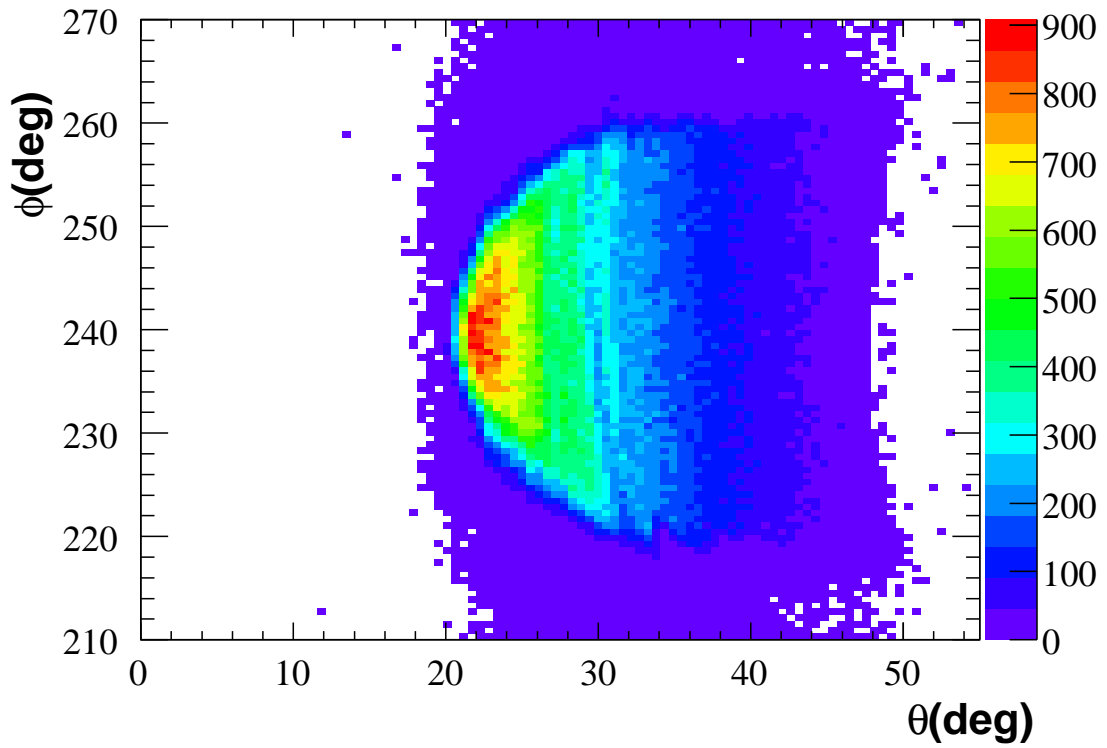
Figure 4-9: On the top is shown the particle distribution before applying the fiducial cut. On the bottom the position of the fiducial cut was applied.
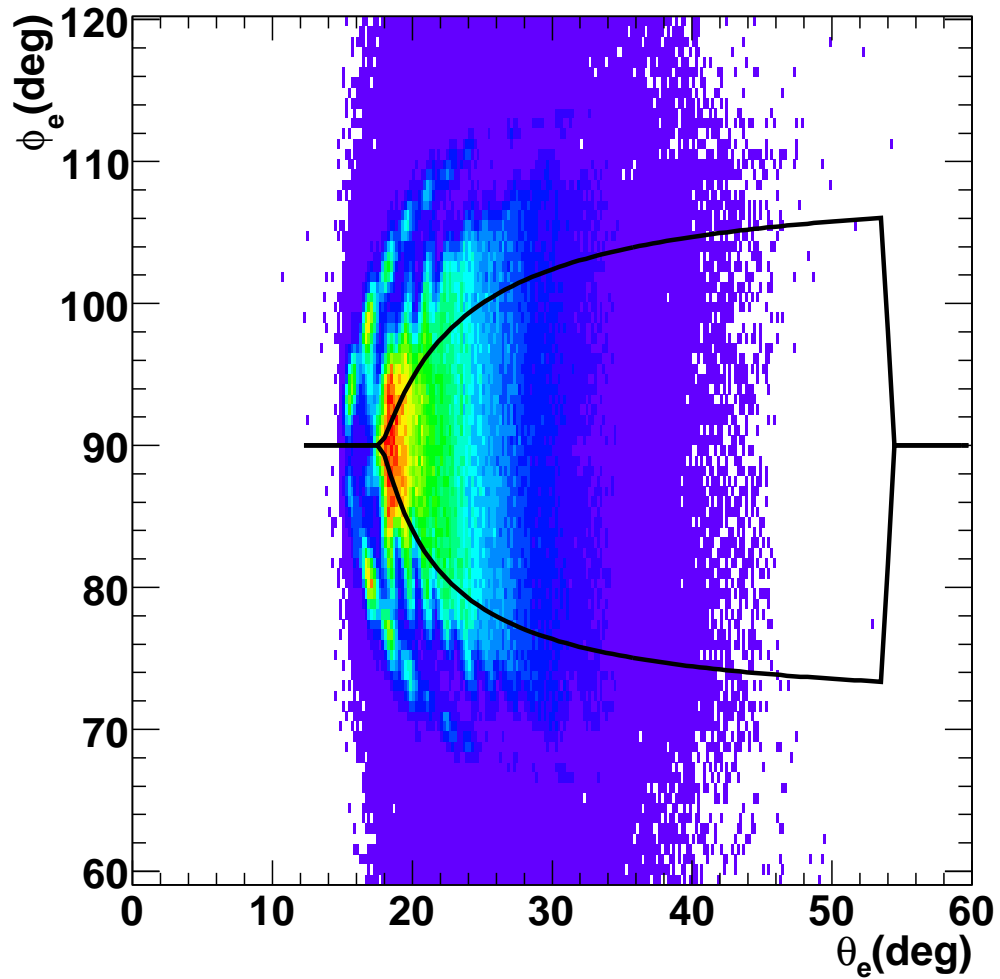
Figure 4-10: Cherenkov efficiency as a function of θ and ϕ for electrons in Sector 2 of the detector of momentum of $2GeV$. In the plot is shown how the Fiducial Cut (the black curve) cuts off the regions where the efficiency has a very complicate behavior.

Sector	Side	Par	p_0	p_1	p_2	p_3	p_4	p_5
1	-1	a	25	-12	0.501025	4.4	0	0
1	-1	b	1.92939	1.7434	-0.557132	0.5	0	0
1	-1	θ_{min}	15	0.88186	-1.30003	5.76432	2.5729	-0.1
1	1	a	25	-12	0.823146	4.4	0	0
1	1	b	3.1227	1.89182	-2	0.779806	0	0
2	-1	a	25	-12	0.554702	4.4	0	0
2	-1	b	3.06703	2	-2	0.5	0	0
2	-1	θ_{min}	13.075	1.62944	0.226114	0.1	18.2157	-0.828278
2	1	a	22.3726	-12	0.838731	4.4	0	0
2	1	b	1.83127	1.89806	-0.236188	0.62221	0	0
3	-1	a	25	-12	0.498556	4.4	0	0
3	-1	b	2.90265	1.43039	-2	0.749855	0	0
3	-1	θ_{min}	13	1.71788	0.0359657	0.100001	15.8527	-0.661962
3	1	a	25	-12	0.582999	4.4	0	0
3	1	b	1.92176	1.82314	-0.759261	0.5	0	0
4	-1	a	25	-12	0.726905	4.4	0	0
4	-1	b	2.36137	2	-0.404826	0.813316	0	0
4	-1	θ_{min}	15	-0.923262	-0.530852	6.14555	17.3828	-1.58196
4	1	a	23.8476	-12	0.704378	4.4	0	0
4	1	b	1.87064	2	-0.315735	0.703461	0	0
5	-1	a	25	-12	0.701835	4.4	0	0
5	-1	b	2.93575	0.852784	-2	0.5	0	0
5	-1	θ_{min}	15	1.31004	-1.16489	5.10505	2.22448	-0.1
5	1	a	22.7683	-12	2.55358	4.4	0	0
5	1	b	2.38154	0.803418	-0.251101	1.6	0	0
6	-1	a	25	-12	0.732397	4.4	0	0
6	-1	b	1.99008	1.66759	-0.351929	0.5	0	0
6	-1	θ_{min}	14.7492	2.42291	-0.667212	6.7429	-86.3025	-4.99965
6	1	a	25	-8	0.396816	4.8	0	0
6	1	b	3.03289	1.03817	-2	0.5	0	0

Table 4.1: Set of parameters for the Fiducial cut (function as equation 4.4) for electron and beam energy of 4.0 GeV

Sector	Side	Par	p_0	p_1	p_2	p_3	p_4	p_5
1	-1	a	25	-12	0.5605	4.4	0	0
1	-1	b	2.1945	1.51417	-0.354081	0.5	0	0
1	-1	θ_{min}	15	-0.425145	-0.666294	5.73077	10.4976	-1.13254
1	1	a	25	-8	0.479446	4.8	0	0
1	1	b	3.57349	2	-2	0.5	0	0
2	-1	a	25	-12	0.714261	4.4	0	0
2	-1	b	4	1.56882	-2	0.5	0	0
2	-1	θ_{min}	15	-1.02217	-0.616567	5.51799	14.0557	-1.16189
2	1	a	25	-10.3277	0.380908	4.79964	0	0
2	1	b	3.02279	0.966175	-2	0.527823	0	0
3	-1	a	25	-12	0.616788	4.4	0	0
3	-1	b	3.3352	2	-2	1.01681	0	0
3	-1	θ_{min}	15	-0.7837	-0.673602	8.05224	15.2178	-2.08386
3	1	a	25	-12	0.675835	4.4	0	0
3	1	b	2.02102	2	-1.70021	0.68655	0	0
4	-1	a	24.6345	-12	0.62982	4.4	0	0
4	-1	b	2.22769	2	-0.760895	1.31808	0	0
4	-1	θ_{min}	15	-1.47798	-0.647113	7.74737	16.7291	-1.79939
4	1	a	25	-11.3361	0.636018	4.4815	0	0
4	1	b	3.1948	0.192701	-1.27578	1.6	0	0
5	-1	a	23.4731	-12	1.84236	4.4	0	0
5	-1	b	1.63143	1.90179	-0.213751	0.786844	0	0
5	-1	θ_{min}	13	3.47361	-0.34459	8.45226	-63.4556	-3.3791
5	1	a	23.7067	-12	2.92146	4.4	0	0
5	1	b	3.0934	0.821726	-0.233492	1.6	0	0
6	-1	a	24.8599	-12	1.00513	4.4	0	0
6	-1	b	3.19807	0.173168	-0.1	1.6	0	0
6	-1	θ_{min}	13	3.5714	-0.398458	9.54265	-22.649	-1.89746
6	1	a	25	-11.4641	0.55553	4.41327	0	0
6	1	b	2.48828	2	-2	0.70261	0	0

Table 4.2: Set of parameters for the Fiducial cut (function as equation 4.4) for electron and beam energy of 5.0 GeV

Sector	Side	Par	p_0	p_1	p_2	p_3	p_4	p_5
1	-1	a	24.1007	-12	0.988602	4.4	0	0
1	-1	b	1.55185	1.68372	-0.161292	0.5	0	0
1	-1	θ_{min}	15	-3.58709	-0.790803	10	41.2384	-2.77844
1	1	a	24.69	-12	1.93755	4.4	0	0
1	1	b	3.12909	2	-0.378116	1.5125	0	0
2	-1	a	24.9833	-12	0.88648	4.4	0	0
2	-1	b	1.82949	2	-0.231991	0.705425	0	0
2	-1	θ_{min}	15	-3.18861	-0.815618	10	32.1378	-2.66887
2	1	a	25	-12	1.01982	4.4	0	0
2	1	b	2.7463	2	-0.253927	1.32911	0	0
3	-1	a	25	-12	0.800149	4.4	0	0
3	-1	b	3.1405	1.58174	-2	1.31869	0	0
3	-1	θ_{min}	15	-2.82339	-0.810061	10	60.6398	-3.4957
3	1	a	25	-12	0.86966	4.4	0	0
3	1	b	3.23553	2	-0.273695	0.709503	0	0
4	-1	a	24.2665	-8	0.607099	4.8	0	0
4	-1	b	3.20671	0.410017	-2	0.522952	0	0
4	-1	θ_{min}	15	-1.97552	-0.84627	10	34.995	-3.9352
4	1	a	25	-12	0.975533	4.4	0	0
4	1	b	3.47462	1.80575	-0.202664	0.5	0	0
5	-1	a	24.188	-12	1.32876	4.4	0	0
5	-1	b	1.5	1.7525	-0.189277	0.856299	0	0
5	-1	θ_{min}	15	-2.30891	-0.800546	10	88.7268	-5
5	1	a	25	-12	1.78226	4.4	0	0
5	1	b	3.61859	2	-0.366367	0.651266	0	0
6	-1	a	24.765	-12	0.925827	4.4	0	0
6	-1	b	1.5	1.34598	-0.326831	1.33186	0	0
6	-1	θ_{min}	14.1075	-2.03962	-0.51452	9.99998	13.4081	-2.09748
6	1	a	25	-12	1.0577	4.4	0	0
6	1	b	3.42444	2	-0.590989	1.6	0	0

Table 4.3: Set of parameters for the Fiducial cut (function as equation 4.4) for electron that scatter from the liquid target and beam energy of 5.0 GeV

Sector	Side	Par	p_0	p_1	p_2	p_3	p_4	p_5
1	-1	a	24.359	-12	1.08727	4.4	0	0
1	-1	b	1.5	1.59052	-0.259681	1.27129	0	0
1	-1	θ_{min}	15	2	-0.766135	6.12341	0.881064	-0.1
1	1	a	25	-12	2.24554	4.4	0	0
1	1	b	3.4203	2	-0.290494	1.6	0	0
2	-1	a	25	-12	0.89663	4.4	0	0
2	-1	b	2.36804	1.80254	-0.5017	1.3313	0	0
2	-1	θ_{min}	15	-3.70033	-0.814569	10	49.079	-2.9723
2	1	a	24.312	-12	1.74735	4.4	0	0
2	1	b	3.07173	2	-0.387264	1.52787	0	0
3	-1	a	24.6813	-12	0.734971	4.4	0	0
3	-1	b	1.5	1.93037	-0.297351	1.18353	0	0
3	-1	θ_{min}	13.09	-1	-0.290864	10	5.10383	-0.978917
3	1	a	25	-12	0.882621	4.4	0	0
3	1	b	1.98006	2	-0.426294	1.58099	0	0
4	-1	a	25	-12	0.681203	4.4	0	0
4	-1	b	1.61194	1.83177	-0.217064	0.5	0	0
4	-1	θ_{min}	15	4	-0.934274	0.580047	4.19068	-0.1
4	1	a	25	-12	1.04315	4.4	0	0
4	1	b	3.36554	2	-0.274802	0.841709	0	0
5	-1	a	24.603	-12	0.970751	4.4	0	0
5	-1	b	1.61678	1.47754	-0.3742	1.25186	0	0
5	-1	θ_{min}	15	3.85171	-0.884537	1.98321	3.17789	-0.1
5	1	a	24.9181	-12	1.60512	4.4	0	0
5	1	b	4	1.16076	-0.587872	1.6	0	0
6	-1	a	25	-12	0.802173	4.4	0	0
6	-1	b	1.5	1.2357	-0.267626	1.6	0	0
6	-1	θ_{min}	15	-3.27307	-0.76759	10	28.4806	-2.34133
6	1	a	24.9784	-12	0.98088	4.4	0	0
6	1	b	2.87847	2	-0.398506	1.6	0	0

Table 4.4: Set of parameters for the Fiducial cut (function as equation 4.4) for electron that scatter from the solid target and beam energy of 5.0 GeV

Sector	Side	Par	p_0	p_1	p_2	p_3	p_4	p_5
1	-1	a	25.9392	-12	0.453685	4.4	0	0
1	-1	b	2.53279	1.19464	-2	1.25872	0	0
1	-1	θ_{min}	15	4	-0.828672	2.51825	2.15567	-0.1
1	1	a	25.142	-12	0.357039	4.4	0	0
1	1	b	2.25185	0.527297	-0.1	1.55534	0	0
2	-1	a	26.3123	-12	0.40864	4.4	0	0
2	-1	b	2.9569	2	-2	0.74865	0	0
2	-1	θ_{min}	13	1.99082	-0.159112	0.100001	13.6076	-0.554978
2	1	a	26.546	-12	0.425442	4.4	0	0
2	1	b	3.27384	2	-2	0.519786	0	0
3	-1	a	25.2953	-12	0.486011	4.4	0	0
3	-1	b	1.98429	1.914	-0.5088	0.721026	0	0
3	-1	θ_{min}	13	3.82167	-0.0647212	0.100008	9.26858	-0.448555
3	1	a	26.4484	-12	0.519846	4.4	0	0
3	1	b	1.5	1.81489	-0.273122	0.5	0	0
4	-1	a	28	-12	0.366217	4.4	0	0
4	-1	b	2.29784	0.351108	-0.1	1.6	0	0
4	-1	θ_{min}	13	1.50112	-1.3	0.1	12.3802	-0.200086
4	1	a	23	-12	0.562825	4.4	0	0
4	1	b	1.65084	1.91044	-0.574873	0.5	0	0
5	-1	a	28	-10.802	0.203741	4.40456	0	0
5	-1	b	2.79198	0.534785	-2	0.720147	0	0
5	-1	θ_{min}	14.6669	1.79097	-0.355746	0.1	14.1265	-0.777645
5	1	a	23.2826	-12	1.15862	4.4	0	0
5	1	b	1.92076	0.90012	-0.112026	0.692653	0	0
6	-1	a	28	-11.9703	0.283665	4.4497	0	0
6	-1	b	1.84305	0.883945	-0.1	1.6	0	0
6	-1	θ_{min}	14.0658	2.20492	-1.3	0.1	8.90341	-0.1
6	1	a	23.8565	-12	1.4323	4.4	0	0
6	1	b	3.18777	0.539951	-2	1.02089	0	0

Table 4.5: Set of parameters for the Fiducial cut (function as equation 4.4) for electron and beam energy of 5.5 GeV

Sector	Side	Par	p_0	p_1	p_2	p_3	p_4	p_5
1	-1	a	17.9074	5.5723	6	1.83182	0	0
1	-1	b	4	2	-2	1.08515	0	0
1	-1	θ_{min}	15	0.256111	-0.925423	4.01752	3.97889	-0.1
1	1	a	17.283	5.21953	6	1.91703	0	0
1	1	b	3.81808	2	-2	1.246	0	0
2	-1	a	19.9864	4.73435	6	1.37676	0	0
2	-1	b	3.61595	1.98742	-2	0.5	0	0
2	-1	θ_{min}	15	7.77818e-12	-0.126147	4.72109	9.33096	-1.56887
2	1	a	18.947	4.40193	6	1.49789	0	0
2	1	b	3.3033	1.02631	-2	0.5	0	0
3	-1	a	18.5174	4.75165	6	1.80735	0	0
3	-1	b	4	1.32282	-0.1	1.6	0	0
3	-1	θ_{min}	15	1.7508e-12	-0.936497	5.08905	2.98662	-0.1
3	1	a	16.6633	5.7028	6	2	0	0
3	1	b	1.53246	1.63003	-0.1	1.6	0	0
4	-1	a	18.0998	5.62361	6	1.42677	0	0
4	-1	b	3.21066	1.19544	-0.1	1.6	0	0
4	-1	θ_{min}	15	1.53231e-12	-0.501064	4.50628	7.2551	-0.644599
4	1	a	17.6381	5.33805	6	1.50883	0	0
4	1	b	4	0.331336	-0.1	1.6	0	0
5	-1	a	18.5118	6.82854	2.02903	1.66004	0	0
5	-1	b	3.04887	2	-0.1	1.6	0	0
5	-1	θ_{min}	15	1.55422e-12	-1.09188	5.22385	3.77058	-0.1
5	1	a	17.5285	5.2995	6	1.54247	0	0
5	1	b	1.63324	1.79676	-0.1	1.6	0	0
6	-1	a	18.7772	4.88048	6	1.48777	0	0
6	-1	b	2.88692	2	-2	0.670166	0	0
6	-1	θ_{min}	15	2.10305e-11	-0.154682	4.03708	11.844	-0.99065
6	1	a	17.953	4.81356	6	1.9173	0	0
6	1	b	3.32424	2	-2	1.39931	0	0

Table 4.6: Set of parameters for the Fiducial cut (function as equation 4.5) for π^-

Sector	Side	Par	p_0	p_1	p_2	p_3	p_4	p_5
1	-1	a	19.1102	4.66203	6	1.81612	-66.8709	7.10615
1	-1	b	2.77099	1.7572	-0.1	1.6	2.48338	-0.342461
1	-1	θ_{min}	15	5.72237e-11	-0.929105	5.6858	1.67706	-0.1
1	1	a	16.757	5.27564	6	1.97715	-52.4773	5.3715
1	1	b	2.78222	2	-0.1	1.6	-1.35167	0.0964232
2	-1	a	19.1401	6.66175	2.50216	1.39498	-29.3615	2.45971
2	-1	b	4	2	-0.1	1.6	7.4528	-0.833107
2	-1	θ_{min}	15	4.92273e-14	-0.278366	3.2139	19.8617	-1.92141
2	1	a	19.0101	3.61646	6	1.59532	-11.0627	0.787976
2	1	b	2.14054	2	-0.1	1.6	5.47021	-0.589086
3	-1	a	17.7755	5.53216	6	1.83457	80.0292	-8.27904
3	-1	b	4	2	-0.1	1.6	-16.9357	1.61027
3	-1	θ_{min}	15	0.0847825	0.176445	0.1	29.1472	-1.38031
3	1	a	17.0281	5.78443	6	2	131.174	-13.6811
3	1	b	2.45078	2	-0.1	1.6	15.7436	-1.65744
4	-1	a	18.6028	6.14009	2.99805	1.44775	2.15047	-0.19045
4	-1	b	4	2	-0.1	1.6	0.683928	-0.139022
4	-1	θ_{min}	15	8.02785e-12	-0.13664	3.53939	14.6939	-1.3825
4	1	a	17.6545	5.37066	6	1.53001	22.8617	-3.30725
4	1	b	3.24588	2	-0.1	1.6	-0.457285	0.0833146
5	-1	a	18.8869	5.12526	6	1.69547	-4.51536	-0.00135075
5	-1	b	3.16918	1.18792	-0.1	1.6	0.624475	-0.0762626
5	-1	θ_{min}	15	1.45883e-14	-0.239069	3.8965	12.0028	-1.23209
5	1	a	19.8552	3.73797	6	1.47751	-33.4806	2.85274
5	1	b	1.99527	1.83377	-0.1	1.6	0.179893	0.0215777
6	-1	a	19.7426	4.83528	6	1.38671	-76.6483	7.9199
6	-1	b	3.1559	2	-0.1	1.6	10.7671	-1.12188
6	-1	θ_{min}	15	3.22542e-13	-0.235386	3.77968	13.2531	-1.21174
6	1	a	18.7704	4.41378	6	1.84804	7.99312	-1.05906
6	1	b	3.3177	1.15112	-0.1	1.6	5.59571	-0.604218

Table 4.7: Set of parameters for the Fiducial cut (function as equation 4.5) for π^- that scatter from the liquid target

Sector	Side	Par	p_0	p_1	p_2	p_3	p_4	p_5
1	-1	a	21.5906	3	6	1.5	-98.4753	10.1199
1	-1	b	4	2	-0.263359	1.6	12.5401	-1.31724
1	-1	θ_{min}	15	0.129496	-0.932709	5.51985	2.42232	-0.1
1	1	a	20.7613	3	6	1.42228	-63.0704	6.65034
1	1	b	4	2	-0.381708	1.6	4.99486	-0.561441
2	-1	a	15.4821	3	6	1.5	-0.822768	-0.819526
2	-1	b	4	1.29235	-0.1	1.09843	9.95987	-1.09267
2	-1	θ_{min}	13.2774	0.277136	-0.12473	8.0107	-23.8628	-5
2	1	a	21.0209	3	6	1.42991	12.4385	-2.00364
2	1	b	4	2	-0.1	1.6	5.34311	-0.556602
3	-1	a	21.1478	3	6	1.5	75.2906	-7.97896
3	-1	b	4	2	-0.1	1.6	-1.74447	0.0839423
3	-1	θ_{min}	15	1.5451e-12	-0.552632	8.31603	-34.8054	-3.51681
3	1	a	20.8521	3	6	1.5	42.0139	-4.70016
3	1	b	3.81429	2	-0.35339	1.6	6.05545	-0.666807
4	-1	a	19.6232	3	6	1.5	7.44871	-1.60669
4	-1	b	4	0.897632	-0.1	1.6	11.0814	-1.05975
4	-1	θ_{min}	15	0	-0.377014	7.59012	-13.9522	-5
4	1	a	18.3193	3	6	1.5	-10.3767	0.714046
4	1	b	3.62012	2	-0.1	1.6	4.20159	-0.402619
5	-1	a	22.1876	3	6	1.26767	33.3173	-4.00962
5	-1	b	3.67317	2	-0.1	1.6	3.60755	-0.366642
5	-1	θ_{min}	15	4.19664e-15	-0.469396	7.82059	-19.2934	-5
5	1	a	20.7616	3	6	1.23536	-25.2243	2.01082
5	1	b	1.5815	2	-0.110684	1.6	14.8785	-1.52585
6	-1	a	17.8822	3	6	1.5	-27.9399	2.5226
6	-1	b	4	2	-0.1	1.6	1.70384	-0.067631
6	-1	θ_{min}	15	2.42473e-14	-0.68071	8.52575	-27.054	-5
6	1	a	22.4999	2.23911	6	1.5	-49.2345	5.28787
6	1	b	4	2	-0.335201	1.6	12.6318	-1.33811

Table 4.8: Set of parameters for the Fiducial cut (function as equation 4.5) for π^- that scatter from the solid target

Sector	Side	Par	p_0	p_1	p_2	p_3	p_4	p_5
1	-1	a	25	-12	1.64476	4.4	0	0
1	-1	b	4	2	-0.978469	0.5	0	0
1	-1	θ_{min}	7.00823	0.207249	0.169287	0.1	0.1	-0.1
1	1	a	25	-11.9735	0.803484	4.40024	0	0
1	1	b	2.53606	0.442034	-2	1.02806	0	0
2	-1	a	25	-12	1.51915	4.4	0	0
2	-1	b	4	2	-2	0.5	0	0
2	-1	θ_{min}	5.5	0.1	0.506354	0.1	3.30779	-0.651811
2	1	a	24.8096	-8	0.85143	4.8	0	0
2	1	b	2.65468	0.201149	-0.179631	1.6	0	0
3	-1	a	25	-12	1.1095	4.4	0	0
3	-1	b	2.78427	2	-1.73543	0.5	0	0
3	-1	θ_{min}	7.06596	0.127764	-0.0663754	0.100003	4.499	-3.1793
3	1	a	24.8758	-8	1.01249	4.8	0	0
3	1	b	3.17084	1.27519	-2	0.5	0	0
4	-1	a	25	-12	0.977829	4.4	0	0
4	-1	b	3.58539	1.38233	-2	0.5	0	0
4	-1	θ_{min}	6.32763	0.1	0.221727	0.1	5.30981	-3.3461
4	1	a	25	-12	0.910994	4.4	0	0
4	1	b	2.47156	1.76076	-1.89436	1.03961	0	0
5	-1	a	25	-12	0.955366	4.4	0	0
5	-1	b	3.32277	0.0410601	-0.953828	0.5	0	0
5	-1	θ_{min}	5.5	0.211012	0.640963	0.1	3.20347	-1.10808
5	1	a	25	-8.52574	0.682825	4.79866	0	0
5	1	b	2.42349	1.25399	-2	0.815707	0	0
6	-1	a	25	-12	0.969146	4.4	0	0
6	-1	b	4	2	-2	1.08576	0	0
6	-1	θ_{min}	5.5	0.281549	0.358452	0.1	0.776161	-0.462045
6	1	a	25	-8	0.88846	4.8	0	0
6	1	b	2.64394	0.15892	-2	1.31013	0	0

Table 4.9: Set of parameters for the Fiducial cut (function as equation 4.4) for π^+

Chapter 5

DATA ANALYSIS

5.1 Background Study

It is important in our analysis to determine in both our targets the cross section of the ρ^0 vector meson. For this purpose one needs to disentangle in the invariant mass distribution (see for example figure5-1) the signal of the ρ^0 decay (A Breit-Wigner shape) from background processes which pass our cuts. A normal procedure will be to use a predetermined
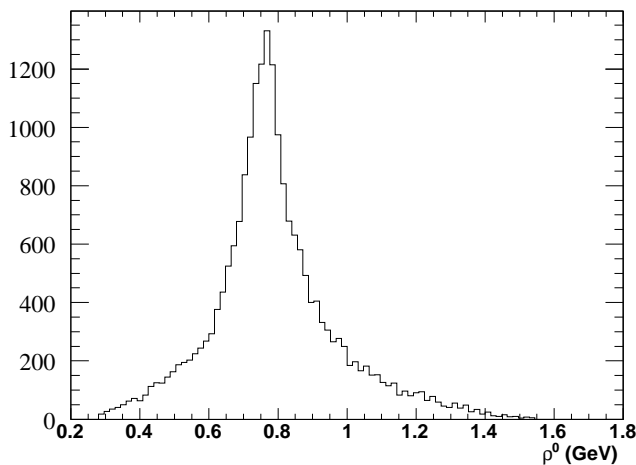
Figure 5-1: Final ρ^0 distribution for full Q^2 range

background-signal function. A fitting procedure will calculate the weight of one respect to the other. Considering that the final ρ^0 distribution has a shape very close to the one expected from the decay of the ρ^0, this fitting procedure will model dependent from the

background shape considered. Another point is that the χ^2 minimization will be driven mainly by the edges of the distribution, because they correspond to the points with smaller errors. We have decided to use a Montecarlo simulation approach to have a less model dependent study of the background.

5.1.1 Event Generator

The Montecarlo Event generator was implemented by B. Mustapha[1] from a preexisting generator developed at the INFN of Genova [47]. It has the following features:

- Characteristics of both the eg2 targets with different combinations (with also the possibility to run with empty configuration).

- Possibility to change the electron beam energy.

- Different ways to turn on the Fermi motion in the target.

- Possibility to consider also Radiative Effects.

- Capability of taking into account Straggling effects with different characteristics.

- Possibility to limit the kinematics of the generated event following our analysis cuts. In this way one does not generate event that will never be considered in the final study. This will save time in processing the next steps, because omits the computation of this data.

- Possibility to use experimental cross sections for every single process (ρ^0 production + single background contributions) as determined in [48]. Using experimental data one has a solid independent basis for determining the signal from the other reactions.

- Chance to define the ρ^0 distribution as a Classical or Relativistic Breit-Wigner.

- Assumption that the main contribution to our background processes will be due to:

---

[1]Argonne National Laboratory: email mustapha@phy.anl.gov

1. $\gamma^* + p \longrightarrow \Delta^{++} + \pi^-$

2. $\gamma^* + p \longrightarrow \Delta^0 + \pi^+$

3. $\gamma^* + p \longrightarrow p + \pi^+ + \pi^-$

One will see if this conjecture have to be consider correct or not from the agreement of the simulated data with our experimental behavior.

This event generator shows very good agreement with the kinematical behavior of our Virtual Meson analysis, giving many advantages as in our definition of the backgrounds or acceptance correction. This will be shown and explain in the following sections.

5.1.2 GSIM

GSIM is a program which simulates the response of the CLAS detector to Montecarlo generated events. The peculiarity of the Eg2 targets has been implemented by Hayk Hakobyan (see figure. 5-2 as a reference for the Eg2 target and 5-3 as the simulated picture). One can see a more detailed description of the implementation of the target at [49] and [50].
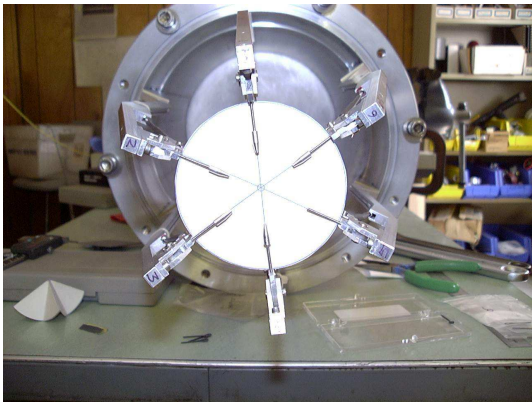
Figure 5-2: Picture of the Eg2 target during the assembling process
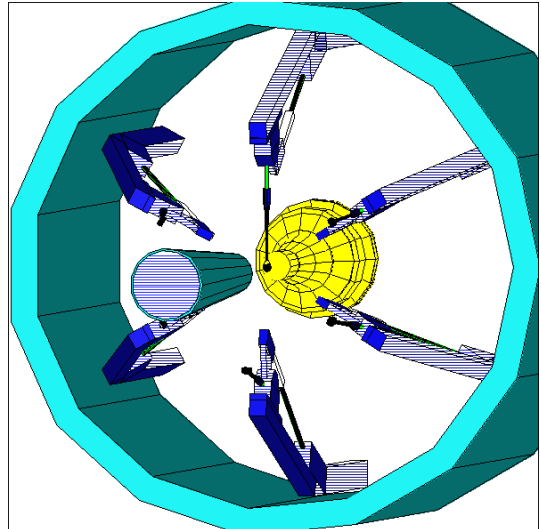
Figure 5-3: Eg2 Target input in GSIM

84

5.1.3 GPP

After the simulation with GSIM of the full geometry of CLAS during the EG2 experiment, one needs to connect the Montecarlo data to the resolution and efficiency of the detector during the run. One will also have to take into account the fact that we are analyzing separately different targets configuration and that each of these configurations will have slightly different efficiency (because they were taken at different times). To construct an estimate of the situation of the detectors, a file has been created with the sum of the information of each run for each single configuration of targets and Beam Energy (See http://www.jlab.org/Hall-B/secure/eg2/Efficiency/). The procedure I have followed to create a Map for the Drift Chambers Inefficiency is the one presented in [51]. A different Map has been created and put in a database for each combination of targets and energy. In figure 5-4 is shown an example of the efficiency during our experiment which will be tuned into our simulation.
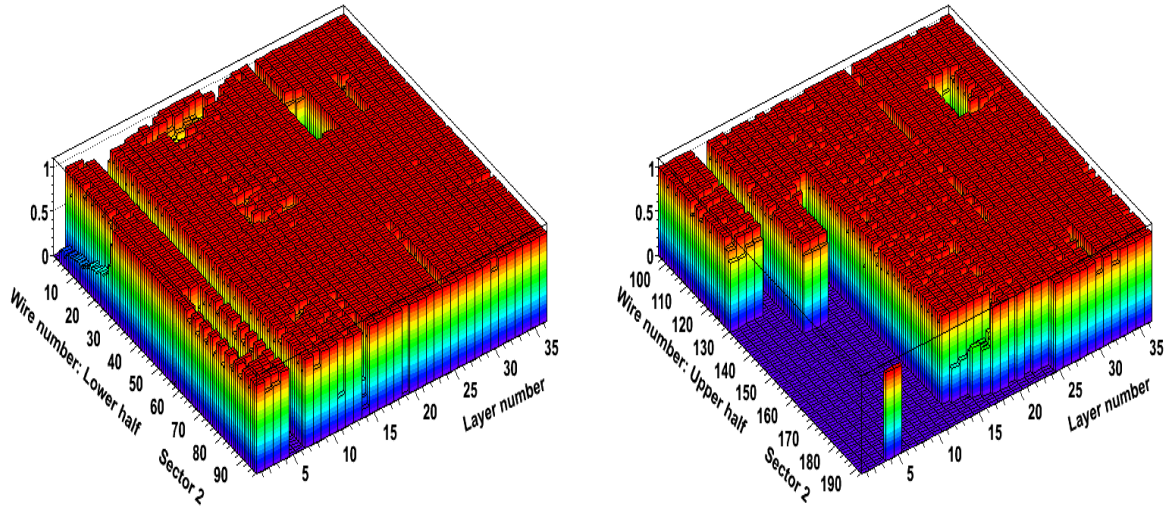
Figure 5-4: Efficiency plot in Sector 2 for $D^2 + Fe$ at $5GeV$ as a function of the Layer Number and the Wire Number.

Another feature of GPP (GSIM Post Processing) is that it permits to smear the distributions of the Distance Of Closest Approach (DOCA) in the Drift Chambers and of the Time Of Flight simulated in the scintillators. This will give a more realistic behavior, adding a Gaussian with an adjustable sigma to the distribution's edges. To correlate the simulation with the data, I have used the Time Based Track Residual for both proton and electron: This quantity is determined during the data analysis for each Sector and Super-Layer of the Drift Chambers (and is used in DC calibrations). As before, I have added the information of each run in any specific combination and created a single file as a model for the simulated events. This is done in order to have a picture of the detector properties during every single configuration of the experiment. As shown in figure. 5-5, in exchange for having a better agreement with the experimental value, I have used, for fitting the data, the sum of 2 different Gaussian with the same weight. One (wide) will cover the edges distribution, the other (narrow), will shape the center (a similar procedure is used in DC calibrations). At the time of introducing the inefficiencies in the simulation (see section 5.2 at page 5.2), I will have to run 50% of the time with one configuration (wide) and 50% with the other (narrow). In order to get the desired result I will need to consider both the outputs together (as shown in figure 5-5).

GPP permits just the choice of a single sigma (as the parameter for the gaussian smearing) for each Region of the Drift Chambers. I will choose the one which better describes the behavior shown by protons and electrons in our data-set (See http://clasweb.jlab.org/cgi-bin/ENOTE/enote.pl?nb=eg2&action=view&page=112). A good agreement on the resolution of our dataset is important because is connected directly to the reconstruction protocol.

5.1.4   Results simulation

After run our simulation through GPP, we will process our MonteCarlo events exactly as our original dataset, firstly reconstructing the track with RECSIS and then putting it in our ρ^0 identification procedure (as explained in Chapter 3). We can now compare our Vector Meson Invariant mass histograms and see how, as shown in figures. 5-6 , 5-7 , 5-8 , 5-9,
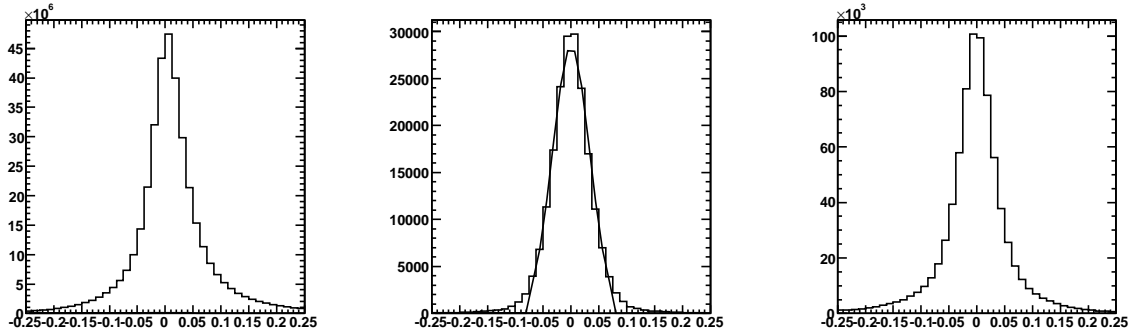
Figure 5-5: Distribution of TBT Residual for Proton in Super-Layer 1: On the left the data, in the center what will look like if we just fit the distribution with a single Gaussian. In the right we have use the sum of 2 different Gaussian , one wide, one narrow

we have good agreement with the behavior detected. This implies that we are confident to be able to separate the ρ^0 Breit-Wigner from the contributions due to the background processes. We also know that we made the right assumption in the Event Generator, when we considered just 3 contributions for the composition of the background processes.

A multiple fit procedure will be used in order to separate the background from the signal and having a better control of the error in the procedure:

- At start we select events which are in our particuar kinematical region (applying cuts in W, t and z and selecting separately each bin in Q^2)

- From the simulated events we determine the statistical distribution of the invariant mass for just the background processes. This distribution is then fitted with a polynomial of 5th order

- We will now select in the simulated events all the processes (this time also the ρ^0 electroproduction). We will fit the distribution so obtained with the function constructed by adding a Breit-Wigner distribution on top of the background function determined in the previous step (see figure 5-6 and figure 5-8).

- We will scale the function so constructed to the invariant mass distribution obtained

ρ^0 REC bin 1 Liquid target χ^2=246 for DF=57
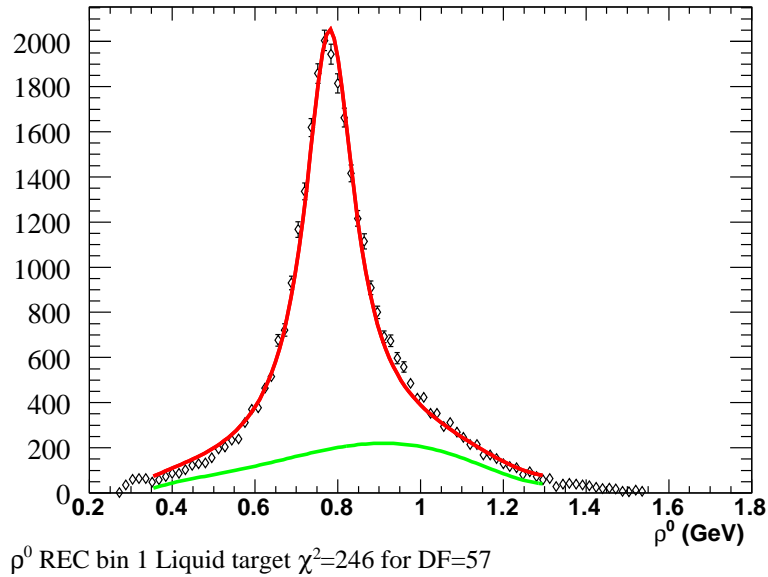
Figure 5-6: Invariant mass distribution for a Q^2 bin of simulated data with Deuterium target. On green is shown the contribution due to background processes fitted with a polynomial of 5th order. On red is shown the fit of the data of the function obtained adding a Breit-Wigner curve to the background function.

from the data (see figure 5-7 and figure 5-9).

This function well describes the data points of the invariant mass distribution for each experimental Q^2 bin. In this way we will obtain a reliable way of weighting the different contribution on the invariant mass in this kinematical range and we will be able to separate the signal from the background processes.

5.2 Acceptance and Efficiency Corrections

CLAS is a detector which covers mostly all the 4π solid angle range. One will analyze at the same time the correction at the experimental data due to:

- Acceptance: Where one is correcting for the fact that the geometry of CLAS does not cover the full momentum-space range of the phenomena under study

- Efficiency: Where one is considering that the detectors that compose CLAS and the reconstruction protocol and our analysys, don't have a perfect efficiency in detecting

ρ^0 bin 1 Liquid target χ^2=68 for DF=57
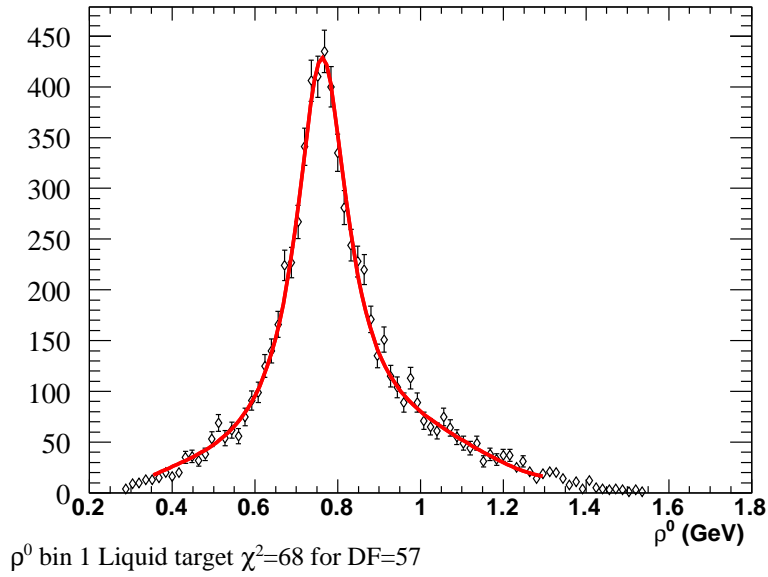
Figure 5-7: The function obtained from the simulation shown in figure 5-6 is then scaled to fit the experimental data points. Here is shown the result of this fit

each particle in our experiment.

This is due to the complexity and difficulty to disentangle the two different contributions from the dataset. In order to determine these corrections to our data, one will need to find a way of getting from our experimental distributions what shape should the data-set be before passing through the detectors. The method used to find the response of CLAS to our experiment is determined by the behavior observed on simulated data:

- As Event generator we will use the one developed for the study of the Background (see section 5.1.1), because can well describe the kinematic behavior of our experiment

- The events are then passed through GSIM, which will simulate the geometry of the detector and of the target: This will take care of the Acceptance of CLAS

- The output of GSIM will then pass through GPP, simulating the efficiency of every single part and giving to them a more realistic statistical behavior

- The output of GPP will pass through a reconstruction process. The data will go through a first pass data analysis in order to simulate its efficiency.

ρ^0 REC bin 1 Solid target χ^2=215 for DF=57
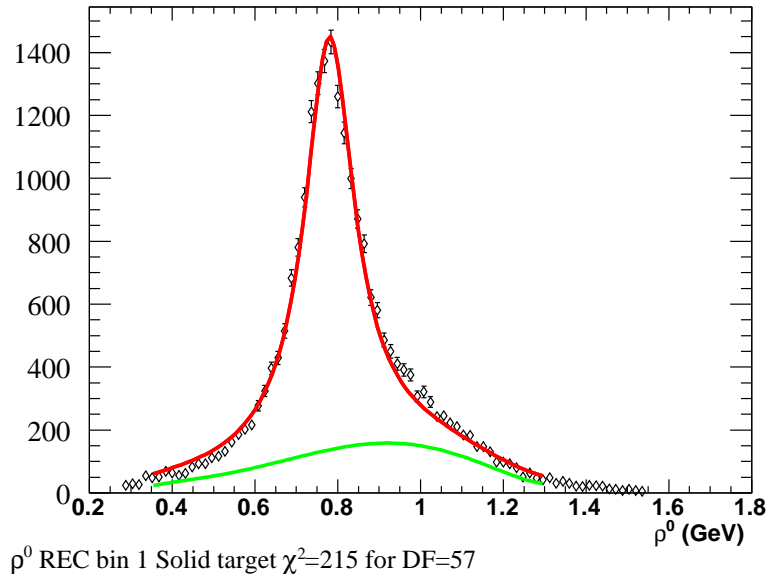
Figure 5-8: Invariant mass distribution for a Q^2 bin of simulated data with Carbon target. On green is shown the contribution due to background processes fitted with a polynomial of 5th order. On red is shown the fit of the data of the function obtained adding a Breit-Wigner curve to the background function.

- The data so processed will go through our Particle Identification and analysis as exactly was the experimental data.

At every step will still be accessible the original generated event distribution and the reconstructed one, permitting to develop a statistical analysis of our acceptance correction.

5.2.1 Independent Variables

In the interest of having a statistical analysis of our Acceptance corrections one will have to bin the data distribution. The distribution will be described by a complete set of independent variables which fully delineate the reaction under study. One will have to use independent variables, because each bin, each single ipercube in this n-dimensional space (where n is the number of degree of freedom of the process), can be treated as an independent identity (and so its acceptance/efficiency correction). Firstly one will have to determine how many variables are needed to identify the process: Considering our reaction (see figure5-10) one has:

ρ⁰ bin 1 Solid target χ^2=113 for DF=57
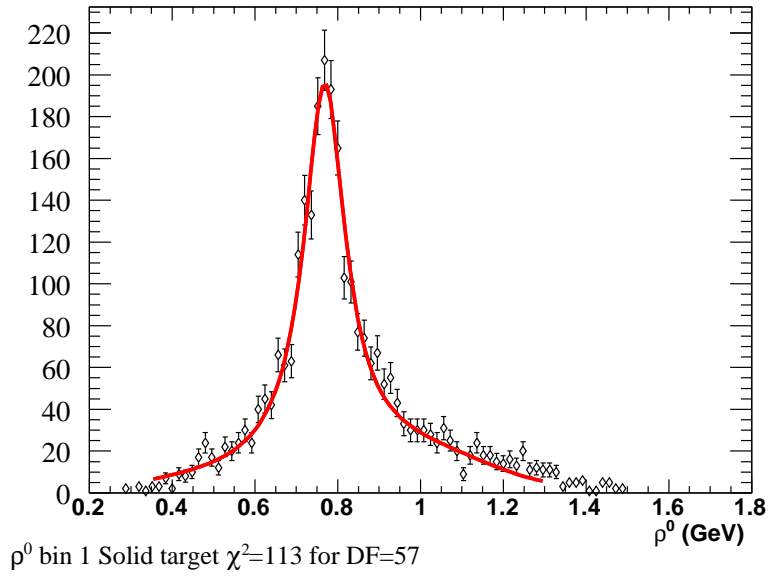
Figure 5-9: The function obtained from the simulation shown in figure 5-8 is then scaled to fit the experimental data points. Here is shown the result of this fit

- The incoming electron: Is fully known, so no variables are needed to describe it

- The incoming proton: One can think 2 models:

  1. The proton is considered at rest in the target, so its behavior is fully known

  2. The proton in the nucleus is considered in motion (Fermi motion). One will have to expend some variables to describe it. But, if one average the acceptance over the Fermi motion (parameterized in the event generator), the kinematic of this particle can be considered as fully known.

- The outgoing electron, the recoiling proton and the detected π^+ and π^-: For each of these one has 3 unknown ((4 momentum - 1) because the particles are physical, so on mass-shell). This will give a total of 12 unknowns. If one consider now that the process needs to satisfy the quadri-momentum conservation (4 unknowns) and that has cylindrical symmetry respect to the direction of the beam (1 unknown), one can state that this reaction has 7 degree of freedom.

91
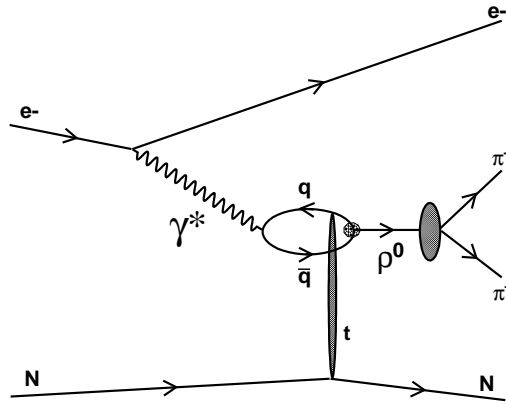
Figure 5-10: Reaction under study. 7 Variables are needed for fully describing his behavior
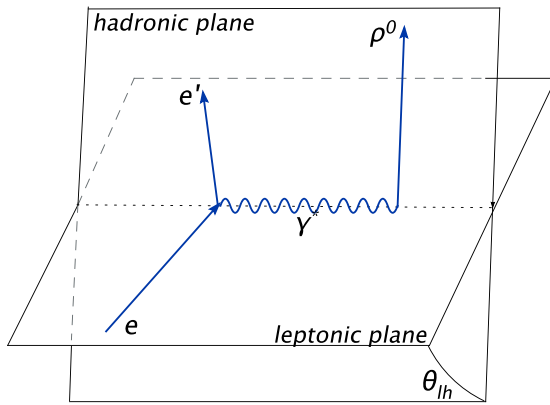
Figure 5-11: Lepton and Hadron plane and definition of the angle
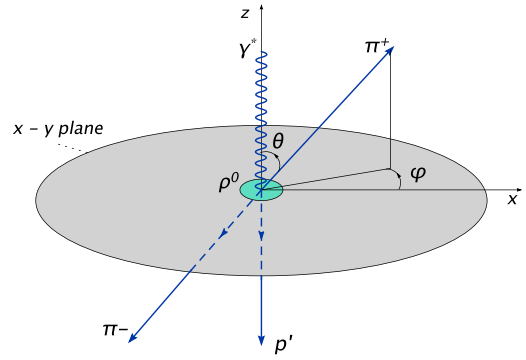
Figure 5-12: ρ^0 decay in the ρ^0 rest system.

Based on the article by K.Schilling [52] and from consideration also of the behavior of our kinematical cuts, the variables being used are:

1. Q^2 (see figure5-10 and relation at pag.4)

2. W (see figure5-10 and relation at pag.4)

3. t (see figure5-10 and relation at pag.58)

4. ρ^0_{mom}, the magnitude of the momentum of the ρ^0 particle

5. θ_{π^+} (see figure5-12) defined as the θ for the decaying π^+ in the ρ^0 rest mass system,

92

where:

- the $\hat{z}$ axis is defined as the vector opposite to the momentum vector of the recoiling proton

- the $\hat{y}$ axis is defined before boosting the system in the ρ^0 rest mass frame as $\hat{y} = \frac{\vec{p_\gamma^*} \times \vec{p_{\rho^0}}}{|\vec{p_\gamma^*} \times \vec{p_{\rho^0}}|}$. It is $\perp$ to $\vec{p_{\rho^0}}$ by construction, so it is left unchanged when boosted in the ρ^0 rest mass frame

- the $\hat{x}$ axis is constructed for completion in the boosted frame as $\hat{x} = \hat{y} \times \hat{z}$

6. ϕ_{π^+} (see figure5-12) is defined as the ϕ for the decaying π^+ in the ρ^0 rest mass system defined above

7. ϕ_{lh} (see figure5-11) is defined as the angle between the leptonic and hadronic plane

For the sake of deciding how to bin in these variables, we will take into account different factors:

- The structure of the cuts applied for constructing our analysis

- The comparison for the variables in consideration of the behavior of the final simulated event distribution with the same variables distribution for the data. In case of complete agreement, after renormalization, of those two plots, we will consider that the simulation is well describing the acceptance correction in this variable. That will permit us to decrease the number of bins for this variable, because we can integrate over the full distribution. We will still need to consider the binning induced by our analysis cuts.

Comparing the results shown from figure 5-13 to figure 5-26, one can see how the simulated events well follow the physical behavior for mostly all of the experimental variables. Some discrepancy is found in the shape shown for t (see figures 5-17 and 5-18),θ_{π^+} (see figures 5-21 and 5-22) and ρ^0_{mom} (see figures 5-19 and 5-19). One can just integrate over the other variables and use the binning induced by our analysis cuts. The final binning used is shown in Tab 5.1.

	Q^2	W	t	ρ^0_{mom}	θ_{π^+}
Bins	n	3	2	4	6

Table 5.1: Binning used to determine the acceptance correction. The value of n depends by the number of bins in Q^2 that we use for studying our transparency effect. It is also directly connected to the statistic available for the single data-set (For example for data with Iron and Deuterium targets, we used $n = 6$).

Q^2 reconstructed event liquid

Q^2 reconstructed event solid
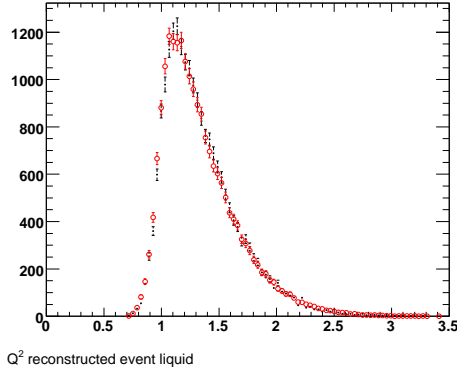
Figure 5-13: Q^2 distribution for Liquid target for data (black) and simulation (red).
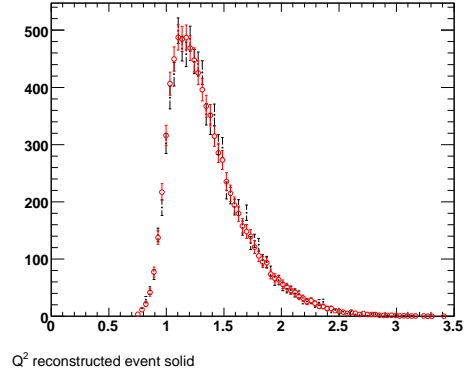
Figure 5-14: Q^2 distribution for Solid target for data (black) and simulation (red).

5.2.2 One to one bin Acceptance correction

After we define which variables we want to use for describing our reaction, we want now to analyze how a generated bin evolve during the all process. One can focus mainly on how to connect the final distribution with the original bin occupancy. In the following I will refer as generated event when I analyze it using the kinematics given by the montecarlo generator; I will refer as reconstructed event when I use the kinematics detected. In this analysis of ρ^0 electroproduction we will use two different methods to determine the acceptance correction to the data-set:

1. The acceptance correction is determined comparing the occupancy of each generated bins with the occupancy in the correspondent (same bin) reconstructed one.

2. The acceptance correction is obtained considering also the possibility that an event generated with kinematics of a particular bin could have its variables slightly modified. It will not be part of the same bin in the reconstructed data. The event "migrates"

94

W reconstructed event liquid

W reconstructed event solid
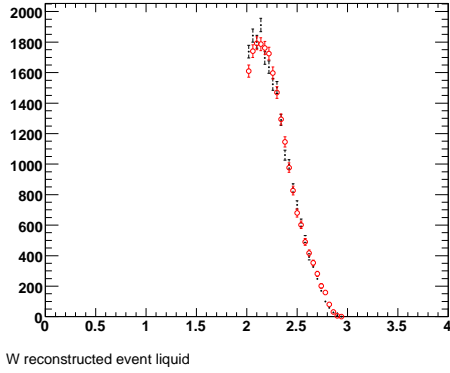
Figure 5-15: W distribution for Liquid target for data (black) and simulation (red).
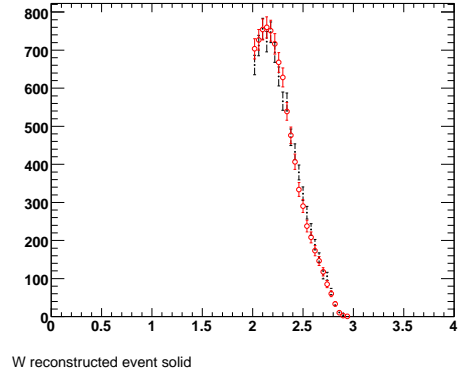
Figure 5-16: W distribution for Solid target for data (black) and simulation (red).

t reconstructed event liquid

t reconstructed event solid
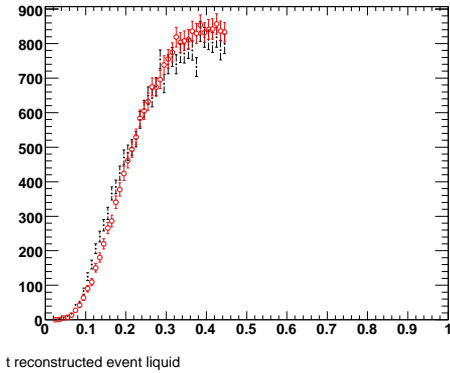
Figure 5-17: t distribution for Liquid target for data (black) and simulation (red).
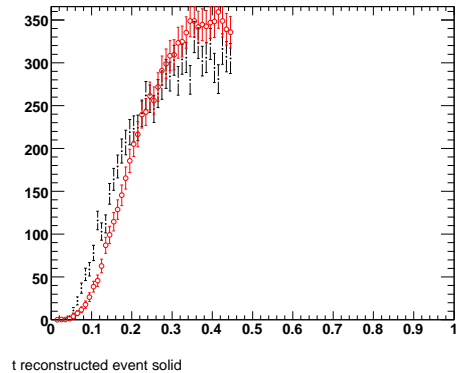
Figure 5-18: t distribution for Solid target for data (black) and simulation (red).

to a different bin. I will talk about this way of constructing the acceptance correction in section 5.2.3.

In this section I will introduce the acceptance correction as in point 1, which was developed for this analysis by Lamiaa El Fassi [1], who also worked in this project. The number of events generated in each target is shown in table 5.2.

The efficiency is defined in each of the 5 dimensional bins k (function of $Q^2, t, W, p_{\rho^0}, \theta_{\pi^+}$) as

$$eff_k = \frac{N_{rec}(Q^2, t, W, p_{\rho^0}, \theta_{\pi^+})}{N_{gen}(Q^2, t, W, p_{\rho^0}, \theta_{\pi^+})} \qquad (5.1)$$

95
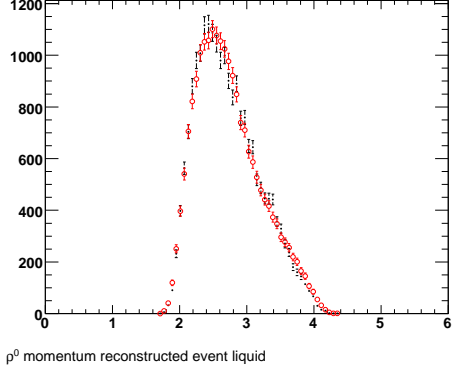
Figure 5-19: ρ_{mom} distribution for Liquid target for data (black) and simulation (red).
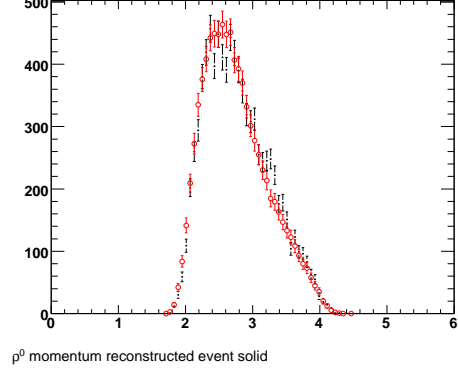
Figure 5-20: ρ_{mom} distribution for Solid target for data (black) and simulation (red).
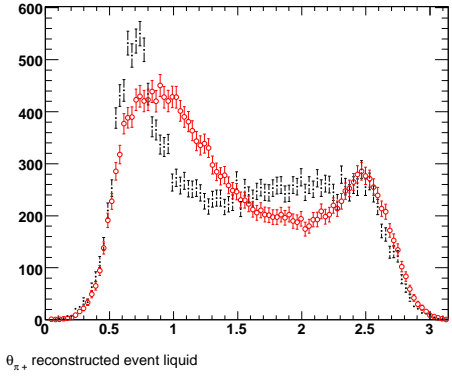
Figure 5-21: $\theta_{\pi+}$ distribution for Liquid target for data (black) and simulation (red).
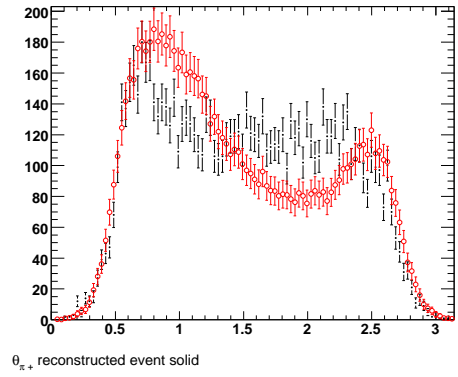
Figure 5-22: $\theta_{\pi+}$ distribution for Solid target for data (black) and simulation (red).

where N represents the number of events in each bin. The correction will be constructed as follows:

- Each event of the data will be assigned to a bin, depending on its kinematics

- This will be considered with a weight $w_k = 1/eff_k$

- At last will be considered the sum of all the events which are part of the same Q^2 bin (used to check the Nuclear Transparency dependence on Q^2),

$$n_{Q^2} = \sum_{k=1}^{m} w_k N_k \tag{5.2}$$

96

$\phi_{\pi+}$ reconstructed event liquid

$\phi_{\pi+}$ reconstructed event solid
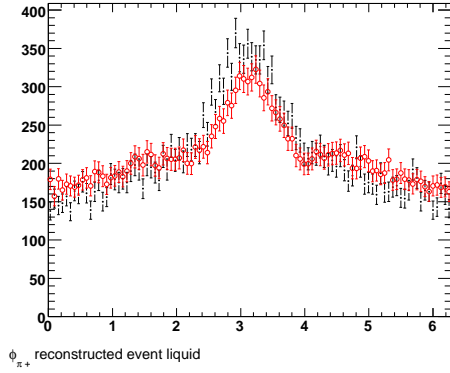
Figure 5-23: $\phi_{\pi+}$ distribution for Liquid target for data (black) and simulation (red).
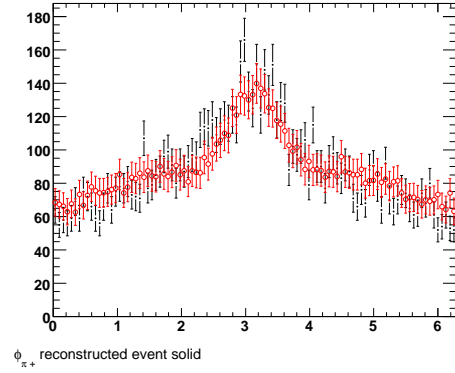
Figure 5-24: $\phi_{\pi+}$ distribution for Solid target for data (black) and simulation (red).

ϕ_{e-h} reconstructed event liquid

ϕ_{e-h} reconstructed event solid
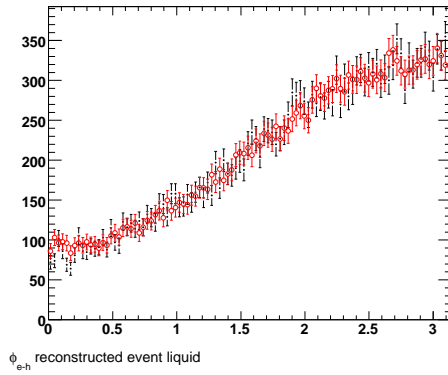
Figure 5-25: ϕ_{e-h} distribution for Liquid target for data (black) and simulation (red).
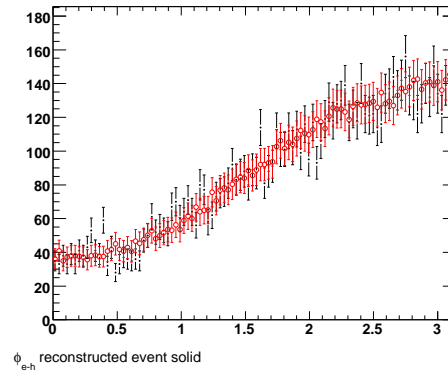
Figure 5-26: ϕ_{e-h} distribution for Solid target for data (black) and simulation (red).

where I am assuming that n_{Q^2} contains m bins and that each k bin as N_k experimental events.

Some bins will have very small statistic, due to small efficiency. This could carry instabilities in the definition of the acceptance correction. To avoid this problem, different cuts in the correction have been applied:

- we rejects events with Q^2 below $0.8 GeV^2$ (0.4 % of the data)

97

Beam Energy	Target	Number of events generated
5.0 GeV	^2H	200 M
	Fe	200 M
	C	100 M
4.0 GeV	^2H	80 M
	Fe	80 M

Table 5.2: Number of events generated in each target and beam energy, which have been used in this analysis.

- we rejects bins with w_k which satisfies (see figure 5-27):

$$w_k \geq 2000 \tag{5.3}$$

$$\frac{\Delta w_k}{w_k} \geq 0.25$$

These cuts will induce a discrepancy if we try to obtain from the reconstructed events the full count of generated events. For this reason we will define a correction factor f_w as

$$f_w = \frac{\sum_{k=1}^{m} w_k N_{k(rec)}}{N_{Q^2(gen)}} \tag{5.4}$$

This correction is defined for each Q^2 bin in which we will divide the ρ^0 histograms. As the acceptance correction, the value of f_w is determined for each target and energy separately (see table 5.3).

Error and statistical analysis

To determine the statistical behavior of the acceptance correction determined in this way, one will need to see how this correlation is logically constructed. One generated events has just two possibilities: being part of the reconstructed bin or not being part of the reconstructed bin. The number of generated events will not carry any error, because will be considered as the number of trials. Taking into account the great number of generated events which we are using, we can assume that the value of eff_k (see equation 5.1) can be considered as a good estimate of the probability that a generated event will be reconstructed.
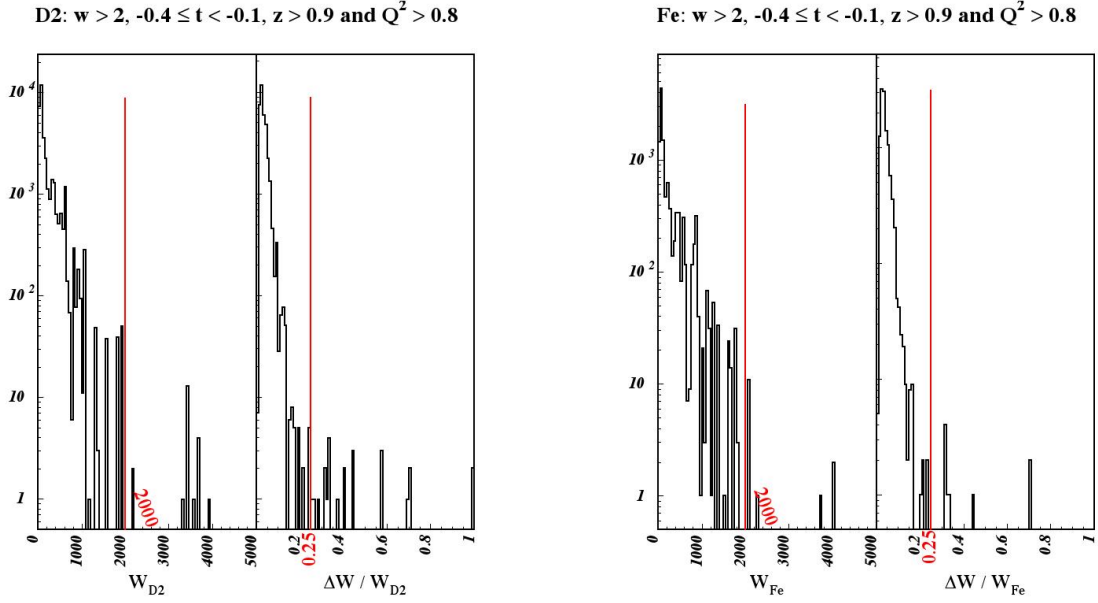
Figure 5-27: w and $\frac{\Delta w}{w}$ histograms for the correction obtained for Deuterium target (left) and Iron target (right). The cuts applied (see equation 5.3) will reject the part of the acceptance correction which will cause some instabilities [1].

To determine the error on eff_k one will need to determine the statistical fluctuation of the number of reconstructed events in each bin $N_{k(rec)}$. After this observations one can see how the acceptance correction follows a binomial statistical behavior, where, in each bin, the number of trials is represented by the number of generated events ($N_{k(gen)}$); The probability p of success is represented in each bin by the efficiency (eff_k). The statistical fluctuation on the number of reconstructed events in a bin is then given by

$$\sigma^2_{N_{k(rec)}} = N_{k(gen)} eff_k (1 - eff_k) \tag{5.5}$$

From this one can derive the error on the efficiency to be

$$\sigma_{eff_k} = \frac{\sigma_{N_{k(rec)}}}{N_{k(gen)}} \tag{5.6}$$

we can find now the error induced on the data after the correction (equation 5.2)

$$\sigma_{n_{Q^2}} = \sqrt{\sum_k^m \left(\underbrace{w_k^2 \sigma^2_{N_{k(dat)}}}_{(a)} + \underbrace{N_{k(dat)}^2 \sigma^2_{w_k}}_{(b)} \right)} \tag{5.7}$$

99

Q^2 bin	Deuterium		Iron		Carbon
	4GeV	5GeV	4GeV	5GeV	5GeV
1	0.96	0.95	0.96	0.94	0.96
2	0.97	0.97	0.97	0.97	0.98
3	0.97	0.98	0.97	0.97	0.97
4		0.98		0.98	
5		0.99		0.99	

f_w values

Table 5.3: Values of the correction f_w defined in equation 5.4 for different targets and energy [1]

In equation 5.7 the (a) part will be used as an estimate for the statistical error. To determine the systematic error induced with this correction we will use the term (b)

Results with this correction

To test the correction so constructed, was decided to plot the Q^2 dependence of the Transparency ratio for the simulated events. In this way we construct an estimate of the entity of the acceptance using this procedure. The result shown in figure 5-28 indicates that this correction is really important and has a Q^2 dependence. This was considered due to the distance between the two targets (solid and liquid) and to the particular kinematic region targeted by this experiment. To increase the confidence in these results I developed an independent way of determining the acceptance correction.

5.2.3 Bin Matrix and Migration

If one starts from an event generated by our MonteCarlo generator, one can schematize this correction as the convolution of two contributions:

- The Event pass all detector/analysis process and is part of our final reconstructed dataset

- The reconstructed event kinematic properties are slightly different from the generated
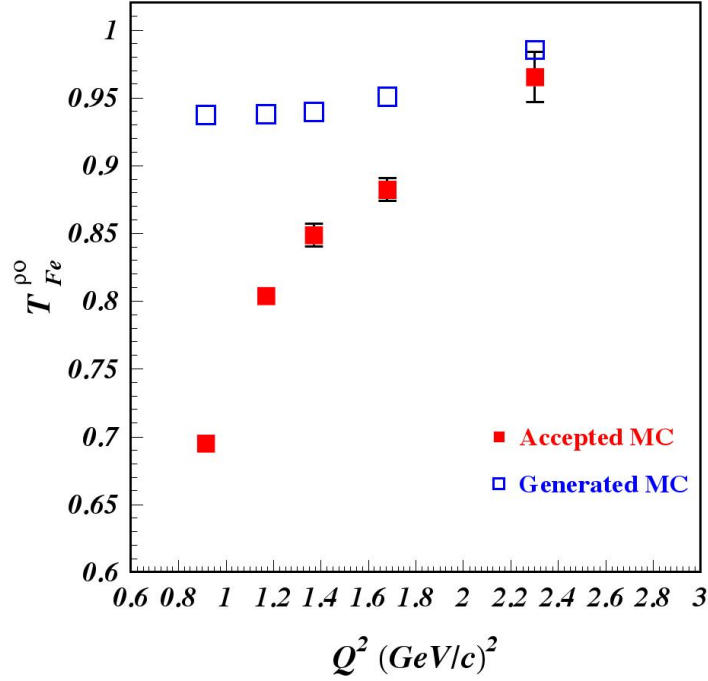
Figure 5-28: In this figure is plotted the Nuclear Transparency ratio for simulations on Iron and Deuterium targets[1]. In blue is plotted the ratio determined using the generated events; In red is plotted the one obtained using the reconstructed events. The effect is really large and will need further study

ones, so the event can "migrate" to a different bin.

A full knowledge of both processes will give a better estimate of what is the real acceptance correction (we still need to bin our distribution, for statistical relevance). One can see from figure 5-29 that is important to take into account the migration to other bins. At the end, our acceptance correction will look like a matrix $N_{bin} \times N_{bin}$ which will relate the number of events in each of the reconstructed bin to the starting generated events:

$$G_i = A_{ij} R_j \tag{5.8}$$

To determine A_{ij} I used the next information:

1. The bin population for the generated event (G_i).

2. The fraction of the population for the generated event which passes our analysis cuts (B_{ik}) for the reconstructed event (It is important to note that, in order to construct
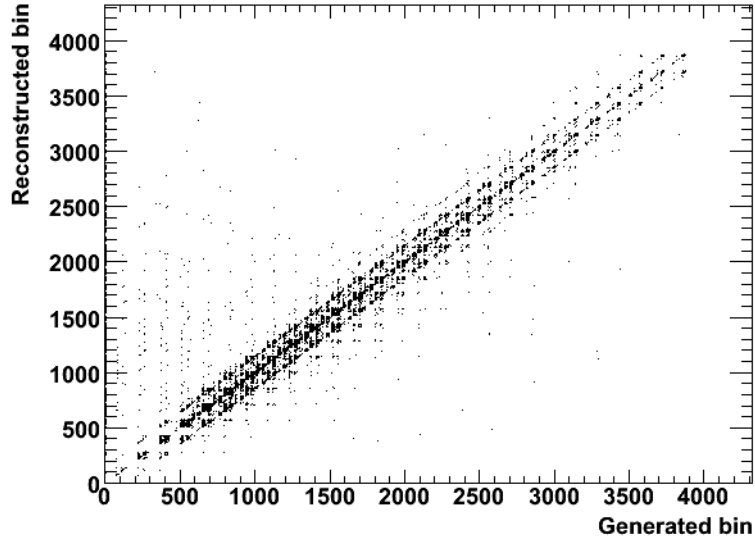
Figure 5-29: Bin migration effect; On the x axis 7-dim the generated bin linearized for 2-dim visualization; on the y axis, the reconstructed one. In case of no bin migration effect, one will have a perfect diagonal.

A_{ij}, the kinematics of the simulated event need to occupy one of the bins for both generated (i) and reconstructed one(j)).

3. The transformation of these selected events. I will determine how the generated event distribution gets deformed during the full process (C_{km}).

4. The fraction of the bin population for the reconstructed event which occupies one of the bin also for his generated part (D_{mj}).

5. the final reconstructed event population without the condition on the generated event bin (R_j), because this is the structure of our experimental data-set.

So, after some normalization (where I will scale the matrix to the value of a single reconstructed event), the acceptance correction will look like

$$G_i = A_{ij} R_j$$

$$G_i = B_{ik} C_{km} D_{mj} R_j \tag{5.9}$$

It is important to note that:

102

- The matrix B_{ik} and D_{mj} are diagonal because they relate a single bin to itself (what fraction of the event in a bin satisfy a certain cut). For this reason they can be expressed as:

$$B_{ik} = \lambda_i \, \delta_{ik} \qquad D_{mj} = \beta_m \, \delta_{mj} \tag{5.10}$$

- The matrix C'_{km} is constructed from the simulated data counting the number of events which are in the $k - generated$ bin and $m - reconstructed$ bin. The structure of the matrix C'_{km} is shown in equation 5.11.

$$(k - generated) \left\{ \begin{array}{c} \overbrace{\begin{pmatrix} C'_{11} & C'_{12} & C'_{13} & \cdots & C'_{1m} & \cdots & C'_{1N} \\ C'_{21} & C'_{22} & C'_{23} & \cdots & C'_{2m} & \cdots & C'_{2N} \\ C'_{31} & C'_{32} & C'_{33} & \cdots & C'_{3m} & \cdots & C'_{3N} \\ \vdots & \vdots & \vdots & \ddots & \vdots & \ddots & \vdots \\ C'_{k1} & C'_{k2} & C'_{k3} & \cdots & C'_{km} & \cdots & C'_{kN} \\ \vdots & \vdots & \vdots & \ddots & \vdots & \ddots & \vdots \\ C'_{N1} & C'_{N2} & C'_{N3} & \cdots & C'_{Nm} & \cdots & C'_{NN} \end{pmatrix}}^{m-reconstructed} \end{array} \right. \tag{5.11}$$

This matrix so constructed will need to be normalized to unit (single reconstructed bin), so that I will be able to delineate the deformation on the experimental data-set. This procedure need to be done in order to connect each bin to their generated value.

Defining now :

1. G'_k as the number of events in the k-generated bin that are part of any reconstructed bins

2. R'_m as the number of events in the m-reconstructed bin that are part of any generated bins

We can finally derive the Acceptance matrix:

$$G'_k = \sum_{m=1}^{N} C'_{km} \tag{5.12}$$

$$R'_m = \sum_{k=1}^{N} C'_{km} \tag{5.13}$$

$$C_{km} = \frac{C'_{km}}{R'_m} \quad \Longrightarrow \quad \text{Normalized} \tag{5.14}$$

$$B_{ik} = \lambda_i \, \delta_{ik} \quad \Longrightarrow \quad \lambda_i = \frac{G_i}{G'_i} \tag{5.15}$$

$$D_{mj} = \beta_m \, \delta_{mj} \quad \Longrightarrow \quad \beta_m = \frac{R'_m}{R_m} \tag{5.16}$$

Putting all togheter, the matrix for correcting our data will be:

$$A_{ij} = \frac{G_i}{G'_i} \, \delta_{ik} \, C_{km} \, \frac{R'_m}{R_m} \, \delta_{mj} = \frac{G_i}{G'_i} \, C_{ij} \, \frac{R'_j}{R_j} \tag{5.17}$$

Error and Statistical Analysis

The acceptance correction matrix has two different statistical behavior:

1. The parts which corresponds to diagonal matrix, because they show how a single bin evolves in these functions, are described by a binomial statistic. In each part one will need to be careful in deciding which quantity represents the number of trials (which part will not carry error)

2. The part which will describe the deformations of the bin occupancies due to bin migration follows a multinomial distribution, becasue considers together an ensemble of possibilities which exclude between each other.

To better schematize the error analysis of each step of the acceptance correction, I am defining the common structure of the statistical uncertainty as

$$\sigma_a^2 = n\,p\,(1-p) \quad \text{where} \quad p = \frac{a}{n} \quad \Longrightarrow \quad \begin{cases} (a) \quad \sigma_p = |\frac{\partial p}{\partial a}|\sigma_a = \frac{\sigma_a}{n} \\[2mm] (b) \quad \sigma_{\frac{1}{p}} = |\frac{\partial(\frac{1}{p})}{\partial a}|\sigma_a = \frac{n}{a^2}\sigma_a \end{cases} \tag{5.18}$$

In equation 5.18 n represents the number of trials, a the number of successes, p the estimate of the probability of success. The Statistical analysis of the three parts of the acceptance correction is done as follows:

- Analysis of the matrix B_{ik} in equation 5.15: In this matrix, following the parametrization in equation 5.18, $p = \frac{1}{\lambda_i}$, $n = G_i$ and $a = G'_i$. For this reason σ_{λ_i} will follow for the determination of the error the case label as (b) in equation 5.18.

- Analysis of the matrix D_{mj} in equation 5.16: In this matrix, $p = \beta_m$, $n = R_m$ and $a = R'_m$. From this follows that the error σ_{β_m} is determined using the equation labeled (a) in equation 5.18.

- Analysis of the matrix C_{km} in equation 5.14: The probability structure of this matrix will follow a multinomial distribution. This distribution is a generalization of the binomial distribution and describes the probability of a particular combination of k-different possible outcomes from n independent trials. Each of the possible outcome has a probability of success of p_k. The probability of a particular combination $x_1, x_2..., x_k$ (where $\sum_{i=1}^{k} x_i = n$, the number of independent trials) is given by:

$$P(x_1, x_2..., x_k) = \frac{n!}{x_1! x_2!....x_k!} p_1^{x_1} p_2^{x_2} .....p_k^{x_k} \quad \text{where} \quad \sum_{i=1}^{k} p_i = 1 \tag{5.19}$$

If one considers each possible outcome separately and groups together the other possibilities one can see how the error will have the same behavior as the binomial distribution

$$\sigma_{x_k}^2 = n\, p_k\, (1 - p_k) \tag{5.20}$$

Other than the possibility of carefully construct the error induced, one of the advantage in constructing the acceptance correction with bin migration in this way is that C'_{km}, following equations 5.12 and 5.13, has the property that:

$$\sum_{k=1}^{N} G'_k = \sum_{m=1}^{N} R'_m = \sum_{k=1}^{N} \sum_{m=1}^{N} C'_{km} \tag{5.21}$$

This property (connected to $\sum_{i=1}^{k} p_i = 1$) gives the freedom to choose which quantity to pick as the independent trial. This will induce the fredom of choosing which matrix to construct. I will construct directly the matrix which define the correction to be applied to the data, avoiding the procedure of inverting a matrix $N_{bins} \times N_{bins}$. In this

way C_{km} represents the probability that a reconstructed event in bin m is generated from bin k (p_k in equation 5.20). The number of indipendent trials is R'_m (n in equation 5.20). The number of sucesses is C'_{km} (x_k in equation 5.20). The error carried by the correction due to C'_{km} is defined as :

$$\sigma_{C_{km}} = |\frac{\partial C_{km}}{\partial C'_{km}}|\sigma_{C'_{km}} = \frac{\sigma_{C'_{km}}}{R'_m} = \frac{\sqrt{C'_{km}\left(1 - \frac{C'_{km}}{R'_m}\right)}}{R'_m} \tag{5.22}$$

Propagating the error from the 3 different contribution in equation 5.17, I can determine the final error induced by the acceptance correction. Following the 2-dimensional implementation of equation 5.7, I will use the error here defined to describe the systematic uncertaintes induced by this acceptance correction.

Simplification of the Acceptance correction matrix

The issue now will be generating and analyzing enough statistic with our simulation to determine with considerable accuracy the value of each of the $N_{bin} \times N_{bin}$ elements of the Acceptance/Efficiency matrix. Such an amount of simulated data is actually not needed, because, for defining the number of ρ^0 in each bin in Q^2 and so determining the cross section, we are integrating in everything that lies in our kinematical cuts. In the same way we will need to sum over our transformed bins after the correction. To show what this imply we can define a matrix:

$$\Pi^{(k)}_{si} = \gamma^{(k)}_s \delta_{si} \text{ , where } \gamma^{(k)}_s = \begin{cases} 1 \text{ if bin } s \text{ is in the kinematical cuts and } k^{th} - Q^2 \text{ bin} \\ \\ 0 \text{ if bin } s \text{ is out the kinematical cuts and } k^{th} - Q^2 \text{ bin} \end{cases}$$
$$\tag{5.23}$$

This matrix will select the bins which have kinematics that are part of a particular Q^2 bin and cut off bins which are outside our kinematical cuts. In fact, to also determine the migration into our data-set, I have defined our binning to go also outside these cuts. This was done for every variable other than Q^2, because we already push the edges of our distribution close to its limits in order to increase our statistic in defining a Q^2 dependence. One can then guess that the contribution following this Q^2 binning will not be determinant,

106

being the addition of the migration of the two sided tail of the distribution inside our range (see figure.5-13 for example). More important is considering the same phenomena for other variables like t (see figure.3-13). Defining now $Q^{(k)}$ as the summed value of corrected events in the kth bin in Q^2, one has (for example here is shown $Q^{(1)}$):

$$Q^{(1)} = \sum_{s=1}^{N} \Pi_{si}^{(1)} A_{ij} R_j = \quad A_{11}R_1 + A_{12}R_2 + A_{13}R_3 + A_{14}R_4 + A_{15}R_5 + A_{16}R_6 + \cdots +$$

$$+ \quad A_{31}R_1 + A_{32}R_2 + A_{33}R_3 + A_{24}R_4 + A_{25}R_5 + A_{26}R_6 + \cdots +$$

$$+ \quad A_{41}R_1 + A_{42}R_2 + A_{43}R_3 + A_{34}R_4 + A_{35}R_5 + A_{36}R_6 + \cdots +$$

$$+ \qquad\qquad\qquad\qquad\qquad\qquad\qquad\qquad \cdots + \cdots =$$

$$= \quad (A_{11} + A_{31} + A_{41} + \cdots)R_1 + (A_{12} + A_{32} + A_{42} + \cdots)R_2 + \cdots$$

One can see that is possible to add the statistic in each column of the matrix A_{ij} for the bins which are into the kinematical cuts of this Q^2 range. Just $N_{bin} \times N_{Q^2}$ elements of the Acceptance/Efficiency matrix are needed to be determine with statistical significance in order to correct our results on Transparency Effect. This also taking into account the migration between different bins.

Another way where I have tried to implement the statistical significance of this acceptance correction was in improving the values and errors definition from the multiple sums of this correction. For example, the correction matrix will have its main contribution from the diagonal terms, which represent the probability that a generated bin will be reconstructed in the same kinematic. Plotting this correction in the planes which describe the kinematical dependence of each bin (plotting it vs t for example or vs $\theta_{\pi+}$) one is able to see a Gaussian behavior with center in the diagonal bin. From another point, when I am finally recon-structing the corrected data, this different bin will have a certain behavior (see figure 5-30). One can then fit these distribution with a function, defining so a sum which will weight the contribution of the different points with their error. Due to the fact that we don't have many bins in each of the kinematical variables, we will not have enough points to well determine the parametric functions. For example, to construct an asymmetric Gaussian, I will need at least ≥ 5 different points. For this reason, and for the fact that this procedure

107
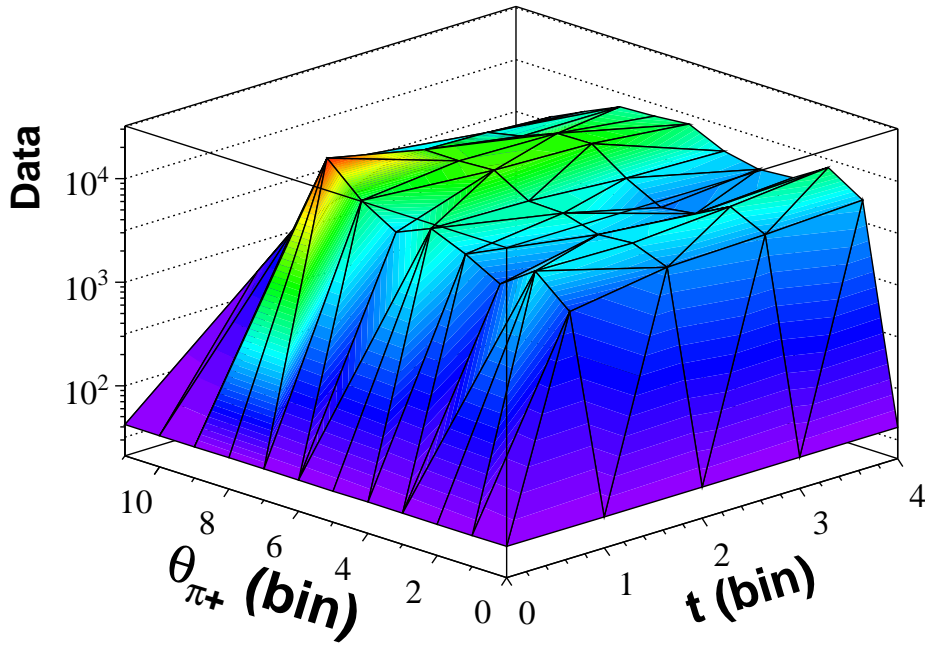
Figure 5-30: Corrected data bin is shown as a function of t and θ_{π^+}

will induce a systematic error due to the choice of a particular function, I have decided to keep using the direct approach explained before (see equation 5.9), adding all the corrected bin and summing their error in quadrature.

5.2.4 Results of Acceptance Correction

For checking if the Acceptance matrix was constructed in the correct way, and so that were not present miscalculations, I have feed this correction with the simulated reconstructed data: As supposed, the correction reconstructed perfectly the bin population of the generated events from the original Montecarlo distribution. If I were to create a plot like the one in figure 5-28 using this correction, I will obtain the same plot. This is because it was obtained treating separately the Montecarlo generated events and the reconstructed one. With the study with bin migration, I will have two independent ways to determine the acceptance correction on the experimental data. In this way I will have a better confidence on the results.

5.3 Radiative Correction

The Radiative Correction has been determined using the Montecarlo event generator, which, as mentioned before, has been implemented with the possibility to include or exclude radiative effects. The kind of radiative effects included are correction to the particles in mass shell in diagrams [53] and correction in the internal part of diagrams. For the latest part has been used a code (DIFFRAD) [54], which has been particularly written for exclusive vector meson production. The correction is then defined as the ratio of ρ^0 generated in our kinematical range (and each Q^2 bin) for simulations with and without radiative effects :

$$F_{Q^2(rad)} = \frac{N_{norad}^{\rho^0}}{N_{rad}^{\rho^0}} \tag{5.24}$$

For the Nuclear Transparency the effect has been found fluctuating between 0.5% and 4%.

5.4 Target Window Correction

To determine the correction due to the windows of the liquid target cell [55], we compared the luminosity with liquid target cell full (deuterium) with the one measured with empty target cell. The ratio between the two was found to be:

$$\frac{L_{empty}}{L_D} = 0.025 \tag{5.25}$$

The material used to construct the cell is Aluminum. We don't have enough data to determine the Transparency ratio for Al (see table 2.2 and 2.3). In order to determine the Transparency ratio for Al we will use the measured data from Carbon and Iron. This data can be fitted with a $A^{\alpha-1}$ function (where A is the mass number and α is the free parameter) [15] for each bin in Q^2 and l_c. We can then determine the expected Transparency ratio for Aluminum [1]. The correction to each bin due to the target windows will be:

$$T_{corr}^A = T^A \left(1 + T^{Al} \times 0.025 \right) \tag{5.26}$$

5.5 Systematic Errors

In this section I will discuss the different sources of systematical error on this analysis. Because we want to determine the Q^2 dependence of the Nuclear Transparency ratio respect to two targets, we will divide the systematic error in two groups:

- The normalization errors: Errors which have no dependence in Q^2, causing a common shift of all the points.

- The point to point errors: Errors which will not shift in the same direction different Q^2 bin.

The point to point error will be added in quadrature with the statistical error. The normalization error will be considered separately, because will not influence the Q^2 slope. In this analysis, once defined a source of systematic error, we define the normalization error for this source as the value of the lowest systematic error. The point to point error will be defined for each source and each bin as

$$\sigma^2_{SYS(p2p)} = \sigma^2_{SYS(tot)} - \sigma^2_{SYS(nor)} \tag{5.27}$$

In the following we will show different source of systematic error (for a more detailed analysis, see [1])

5.5.1 Kinematical Cuts

The cuts on z and t were done to select an exclusive process and to ensure incoherent production (see section 3.3). To find the systematic uncertainties induced by these particular cuts, their limit were let slightly vary and the Nuclear Transparency ratio was determined with the new values. The total systematic error was found affecting the calculated Nuclear Transparency with changes which varied in the Q^2 bins between 0.1% and 1.4% for Iron+Deuterium at beam energy of $5 GeV$. See table 5.4 and table 5.5 for the range and composition of the systematic error (point to point and normalization).

	Point to Point error (%)		
		Iron	Carbon
Q^2 bin	$5GeV$	$4GeV$	$5GeV$
1	1.1	1.1	1.0
2	1.3	-	-
3	0.5	0.9	1.2
4	-	-	-
5	1.1	-	-

Table 5.4: Kinematical cuts: Point to Point systematic errors for different Q^2 bins, different targets and different beam energies

	Normalization error (%)		
		Iron	Carbon
	$5GeV$	$4GeV$	$5GeV$
All Q^2 bins	0.1	0.4	0.4

Table 5.5: Kinematical cuts: Normalization systematic errors for different targets and different beam energies

5.5.2 Acceptance Correction

The systematic uncertainties have been calculated in the two methods used to determine the acceptance correction. Due to the low statistic, the number of bins was not varied, but were changed the limits of each bin. Another test was done omitting the pion non resonant contribution to the background. In both cases the Transparency ratio was determined and the total systematic uncertainties were obtained. This was done adding in quadrature, for each Q^2 bin, the difference of the value so obtained (as explained in this section) with the uncertainty due to the acceptance correction (see equation 5.7 and 5.22).

One to one bin Acceptance correction

For the target combination of Iron+Deuterium with beam energy at $5GeV$ the total systematic error ranges from 0.8% to 1.9% (more detail in table 5.6 and table 5.7).

	Point to Point error (%)		
	Iron		Carbon
Q^2 bin	$5GeV$	$4GeV$	$5GeV$
1	1.6	1.8	1.1
2	-	-	-
3	1.7	1.6	1.2
4	1.6	-	-
5	1.5	-	-

Table 5.6: Acceptance correction (one to one bin): Point to Point systematic errors for different Q^2 bins, different targets and different beam energies

	Normalization error (%)		
	Iron		Carbon
	$5GeV$	$4GeV$	$5GeV$
All Q^2 bins	0.8	0.7	0.7

Table 5.7: Acceptance correction (one to one bin): Normalization systematic errors for different targets and different beam energies

Bin Matrix and Migration

The beam systematic uncertainties induced by the acceptance correction with bin migration are shown in table 5.9 and table 5.8.

5.5.3 Background Subtraction

In order to obtain the systematic error induced by our method of comparison between montecarlo simulations and data, we will test our procedure in 3 different ways:

1. In the Breit-Wigner distribution we will consider the case where the "full with" Γ is considered a free parameter in the fit, or is kept constant at its nominal value of $150.3 MeV$.

2. For the shape of the background we will use the one obtained from our implemented

	Point to Point error (%)			
		Iron		Carbon
Q^2 bin	5GeV	4GeV		5GeV
1	3.0	3.2		2.1
2	-	-		-
3	3.2	3.3		2.4
4	3.1	-		-
5	2.8	-		-

Table 5.8: Acceptance Correction (Bin Migration): Point to Point systematic errors for different Q^2 bins, different targets and different beam energies

	Normalization error (%)			
		Iron		Carbon
	5GeV	4GeV		5GeV
All Q^2 bins	2.1	2.0		2.1

Table 5.9: Acceptance Correction (Bin Migration): Normalization systematic errors for different targets and different beam energies

event generator and the one derived from the original generator.

3. Different shapes for the ρ^0 invariant mass distribution were used in parallel with the non relativistic Breit-Wigner: Relativistic p-wave Breit-Wigner, Ross-Stodolsky parametrization (see [1] for reference of these functions). We then picked the distribution which gave the bigger point to point error.

The value obtained for the systematic error are shown in tables 5.10 and 5.11.

5.5.4 Radiative Correction

The systematic uncertainties will be determined for the Radiative Correction checking the shift induced by our particular montecarlo generator. For this reason we will compare the results from our event generator and the original version [47]. Both montecarlo are implemented with DIFFRAD to determine the radiative correction in vector meson production.

	Point to Point error (%)			
		Iron		Carbon
Q^2 bin	5GeV	4GeV		5GeV
1	1.5	2.2		1.7
2	0.2	1		0.5
3	1.6	0.8		1.7
4	1.5	-		-
5	1.7	-		-

Table 5.10: Background Subtraction: Point to Point systematic errors for different Q^2 bins, different targets and different beam energies

	Normalization error (%)			
		Iron		Carbon
	5GeV	4GeV		5GeV
All Q^2 bins	0.5	0.1		0.7

Table 5.11: Background Subtraction: Normalization systematic errors for different targets and different beam energies

The systematic error for this correction are shown in tables 5.12 and 5.13

5.5.5 Target Window Correction

In order to determine the systematic error on the Target Window Correction, we assumed a 10% uncertainty induced by the determination of the Transparency ratio through a fitting procedure on $A^{\alpha-1}$. This hypothesis follows from other measurement of this dependence (see for example [15]). Propagating this uncertainty through the equation 5.26, one obtains for this correction a normalization systematic error of 0.25%.

	Point to Point error (%)		
	Iron		Carbon
Q^2 bin	$5GeV$	$4GeV$	$5GeV$
1	1.0	1.1	1.1
2	0.5	-	-
3	-	1.4	0.7
4	1.0	-	-
5	1.8	-	-

Table 5.12: Radiative Correction: Point to Point systematic errors for different Q^2 bins, different targets and different beam energies

	Normalization error (%)		
	Iron		Carbon
	$5GeV$	$4GeV$	$5GeV$
All Q^2 bins	0.3	0.5	0.5

Table 5.13: Radiative Correction: Normalization systematic errors for different targets and different beam energies

Chapter 6

RESULTS AND DISCUSSION

In the previous chapter we have defined the procedure for well determine the cross section ratio between two separate target for ρ^0 electroproduction. In this chapter I will show how we determine the Nuclear Transparency in this experiment. I will then test the theoretical conjecture expressed in chapter 1, where was stated the independence of the Nuclear Transparency from the range of Coherence Lengths reached in this experiment. After this I will finally show the results for the experimental Nuclear Transparency dependence on Q^2 and I will compare them with the model from Frankfurt, Miller and Strikman (FMS) (see section 1.3.4 at page 16 of this thesis).

6.1 Definition of our Transparency effect

The EG2 experiment run with two targets at the same time, in order to compare the cross sections obtained from nuclei of mass number A (in this experiments with had enough statistic for Iron and Carbon) with the one determined from Deuterium.

$$T_A^{\rho^0} = \frac{\left(\frac{N_A^{\rho^0}}{L_A^{int}}\right)}{\left(\frac{N_D^{\rho^0}}{L_D^{int}}\right)} \tag{6.1}$$

In equation 6.1 $N_A^{\rho^0}$ and $N_D^{\rho^0}$ are the extracted number of ρ^0 from the two targets. L_A^{int} is the integrated luminosity for the target A and is defined as:

$$L_A^{int} = n_A^{nucleons} \frac{Q_{int}}{q_e} \tag{6.2}$$

$n_A^{nucleons}$ represents the number of nucleons in target A and is obtained from its properties

$$n_A^{nucleons} = \rho_A \times r_A \times N_{Av} \tag{6.3}$$

where ρ_A is the density of the material, r_A is its thickness (see table 2.1) and N_{Av} is Avogadro's number. The other terms of equation 6.2 are q_e, the single electron charge, and Q_{int}, the integrated charge deposited while collecting data from target A. Using the fact now that we measure the ρ^0 produced from both targets at the same time, we can simplify equation 6.1, and obtain for the Nuclear Transparency:

$$T_A^{\rho^0} = \frac{(\frac{N_A^{\rho^0}}{\rho_A \times r_A})}{(\frac{N_D^{\rho^0}}{\rho_D \times r_D})} \tag{6.4}$$

Other systematic effects are attenuated or canceled from this simultaneous measurement and have already been determined (see section 5.5).

6.2   Coherence Length dependence in this experiment

To test the Coherence Length dependence of the Transparency ratio measured in this experiment, we have considered the distribution of Q^2 vs l_c (see figure 6-1). In order to see the contamination of the Q^2 dependence of the bins in l_c, we decided to study two different intervals in Q^2:

- $1.0 GeV^2 < Q^2 < 1.6 GeV^2$

- $1.0 GeV^2 < Q^2 < 2.2 GeV^2$

The results are shown in figures 6-1, 6-2 , 6-3 , 6-4. No l_c dependence is seen with our statistical precision. This behavior was expected for the particular kinematical range investigated by the EG2 experiment (see figure 1-4 and 1-5 at page 9). To understand this one needs to compare the kinematical range of Q^2 and ν of the EG2 experiment ($0.9 GeV^2 < Q^2 < 2 GeV^2$ and $2.2 GeV < \nu < 3.5 GeV$) with the one of the other experiment which searched for Color Transparency using ρ^0, the HERMES measurement. In this experiment was observed a dependence on the Coherence Length (see figure 1-20). This was due to the fact that the HERMES experiment is in a Q^2, ν range which was right on the region where the Coherence Length effect was important ($0.8 GeV^2 < Q^2 < 4.5 GeV^2$ and

$5GeV < \nu < 24GeV$)). The length inspected by the EG2 experiment is $\leq 1fm$, which is similar to a nucleon size. For this reason, the Coherence length effect, which considers the contribution of other nucleons to the production of the ρ^0 vector meson, was not important in the EG2 experiment.
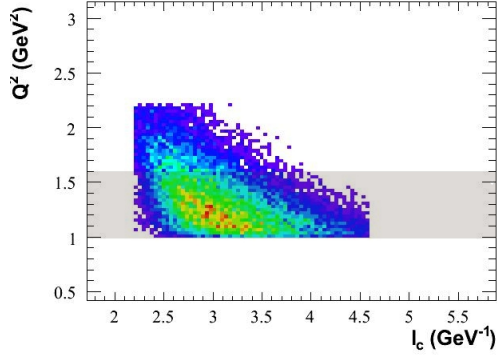
Figure 6-1: The l_c vs Q^2 distribution is shown here for the Iron target. At first we will consider the region in the shadow, characterized by $1.0GeV^2 < Q^2 < 1.6GeV^2$. In this region we will determine the experimental transparency ratio dependence on l_c (see figure 6-2 on the right)
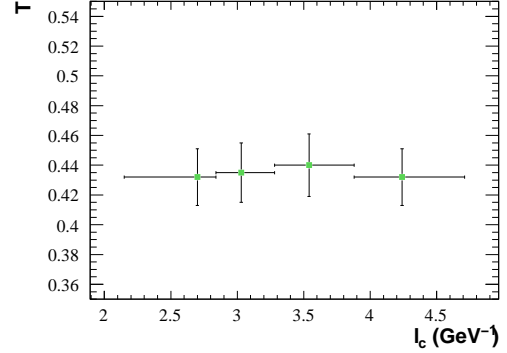
Figure 6-2: Nuclear Transparency ratio as a function of l_c (here expressed in GeV^{-1}, $1GeV^{-1} = 0.193\,fm$). The data-set does present a induced Q^2 dependence in the l_c binning. To avoid it I consider two different Q^2 range. In this plot is shown the data with $1.0GeV^2 < Q^2 < 1.6GeV^2$(see figure 6-1). The data does not show any dependence in l_c, as expected from Glauber theory.

6.3   Nuclear Transparency dependence in Q^2

We can finally determine the Nuclear Transparency ratio in the EG2 experiment. In our data analysis we discover that the correction due to the acceptance/efficiency of the detector/reconstruction/analysis was really important (see figure 5-28 at 101). For this reason we have determined our final result with the two methods as explained in section 5.2.
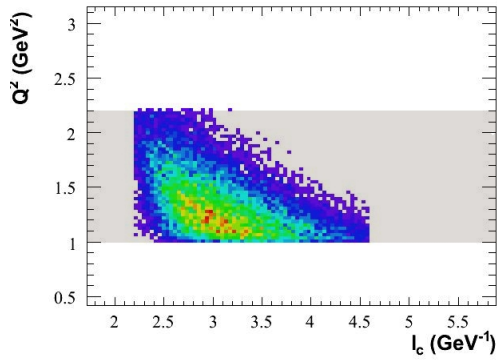
Figure 6-3: The l_c vs Q^2 distribution is shown here for the Iron target. In shadow is selected the region $1.0 GeV^2 < Q^2 < 2.2 GeV^2$. In this region we will determine the experimental transparency ratio dependence on l_c (see figure 6-4 on the right)
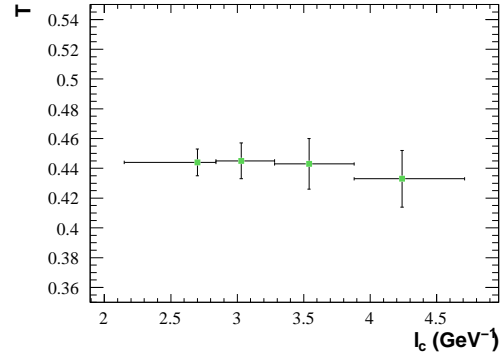
Figure 6-4: Nuclear Transparency ratio as a function of l_c (here expressed in GeV^{-1}, $1 GeV^{-1} = 0.193 \, fm$). In this plot is shown the data with $1.0 GeV^2 < Q^2 < 2.2 GeV^2$(see figure 6-3). The data also in this case does not show any dependence in l_c, as expected from Glauber theory.

6.3.1 Acceptance correction: results with two different methods

The comparison between the two methods are shown in figures 6-5, 6-6, 6-7. The two methods don't present great difference, also if one can notice some common feature in this comparison:

- The error of the correction which use the "bin migration" effect is slightly bigger than the other measurement

- The points with "bin migration" effect have a common shift to higher values of Nuclear Transparency ratio.

This lack of differences between the two methods can be imputed to the fact that, in order to define the Nuclear Transparency, we considered ratios between contemporary measurements on two different targets. Due to the kinematical similarities of the data from the two targets, one can conclude that the migration affects them similarly. It will get then mostly canceled when one determines the ratio.

For these reasons, I have decided to consider the result obtained from the acceptance correction with "bin migration" as an addition to the systematic uncertainties on the Nuclear

Figure 6-5: Comparison of Nuclear Transparency ratio for Carbon data at $5 GeV$ and determined with two different acceptance correction (see section 5.2 of this thesis). In green is shown the result obtained with a "bin by bin" acceptance correction. In red is shown the one obtained considering also the "bin migration" effect. The data is plotted with errors due to statistical and point to point systematical (added in quadrature). The colored bad in the bottom represents the systematical error identified before as normalization (see section 5.5 of this thesis). This last systematical error causes a common shift in all the point of the distribution, and does not contribute to the physical behavior of the Nuclear Transparency ratio (for this reason is not included with the other error).

Transparency. The systematic uncertainties due to the model for the acceptance correction are shown in tables 6.1 and 6.2.

6.3.2   Final results and comparison with the theoretical model

After we compared the results with two different models for the acceptance correction, we have now a good confidence that this correction is well understood. The correspondent systematic error induced by this last correction will not affect too much the error previously obtained. The final results are shown in figures 6-9, 6-8 and 6-12. In these plots we
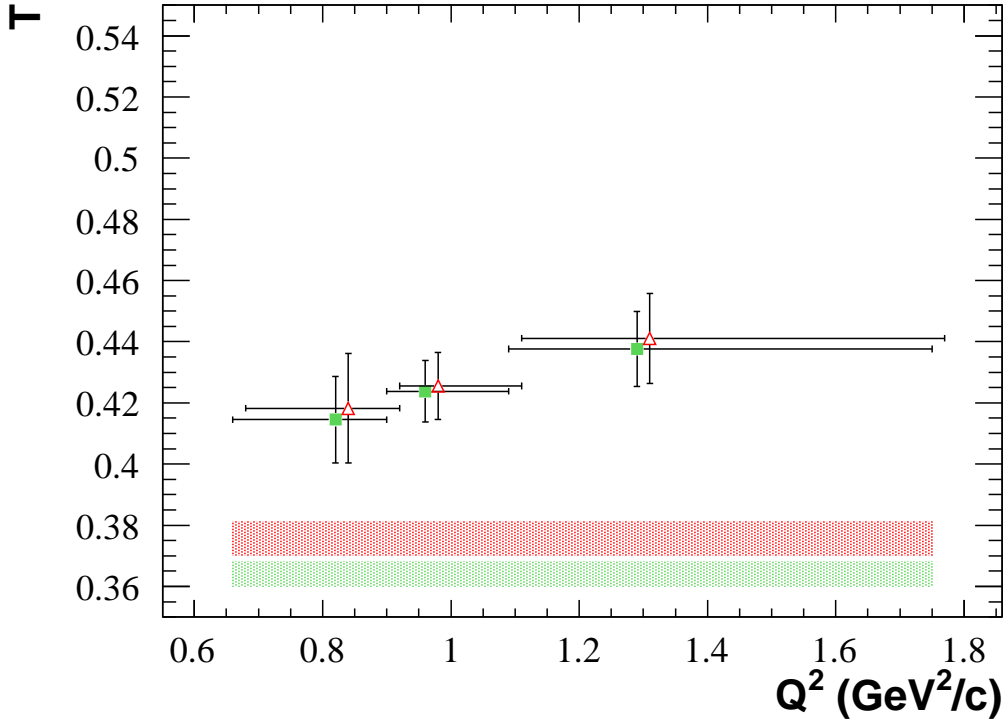
Figure 6-6: Comparison of Nuclear Transparency ratio for Iron data at $4GeV$ and determined with two different acceptance correction (see section 5.2 of this thesis). In green is shown the result obtained with a "bin by bin" acceptance correction. In red is shown the one obtained considering also the "bin migration" effect. The data is plotted with errors due to statistical and point to point systematical (added in quadrature). The colored bad in the bottom represents the systematical error identified before as normalization (see section 5.5 of this thesis). This last systematical error causes a common shift in all the point of the distribution, and does not contribute to the physical behavior of the Nuclear Transparency ratio (for this reason is not included with the other error).

have added the theoretical predictions from the model from L. Frankfurt, G.A. Miller, M. Strikman (FMS, see section 1.3.4). This model corrects its values with the possibility of decay of the ρ^0 inside the nucleus. For this reason we don't need to correct our results for this effect. The analysis of these results can be resumed as follows:

- The result for Iron at $4GeV$ (figure 6-8) shows an increase in Nuclear Transparency with a parallel increase in Q^2. From the FMS model it is not expected a great influence of the Color Transparency effect in this kinematical range. Still, the increase shown with Q^2 cannot be interpret with a Glauber Calculation for the Coherence
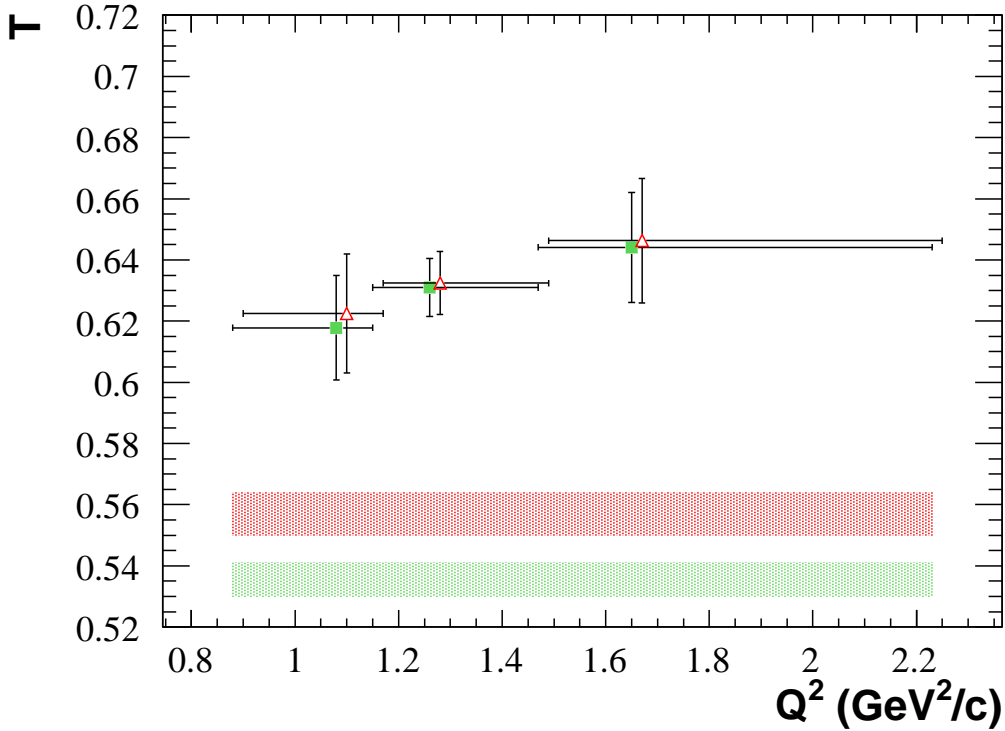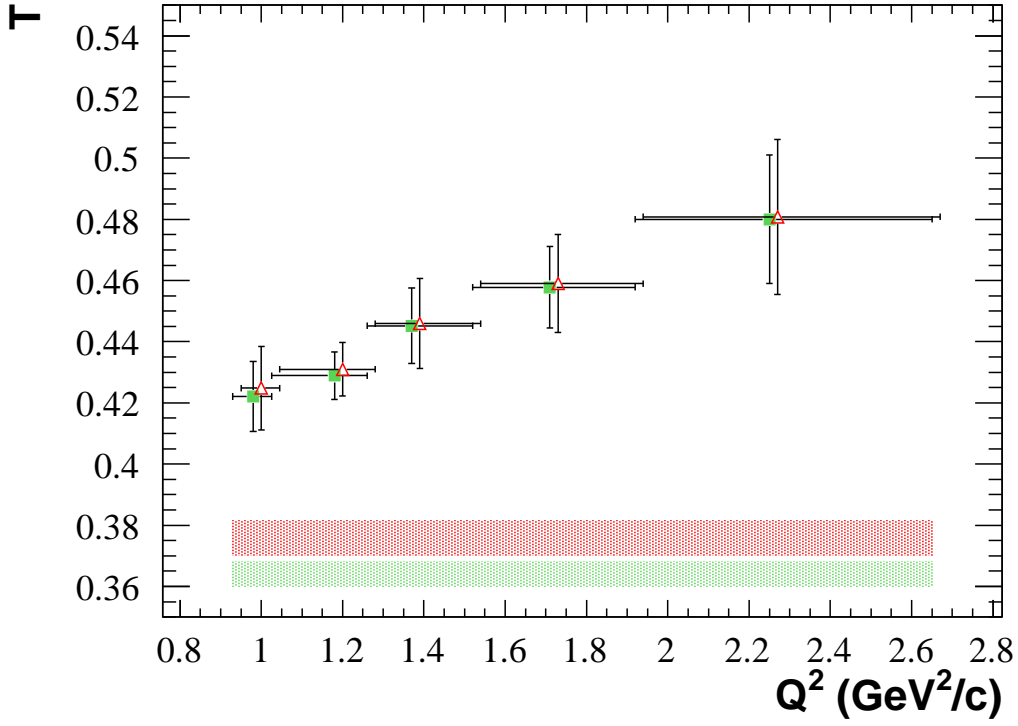
Figure 6-7: Comparison of Nuclear Transparency ratio for Iron data at $5GeV$ and determined with two different acceptance correction (see section 5.2 of this thesis). In green is shown the result obtained with a "bin by bin" acceptance correction. In red is shown the one obtained considering also the "bin migration" effect. The data is plotted with errors due to statistical and point to point systematical (added in quadrature). The colored bad in the bottom represents the systematical error identified before as normalization (see section 5.5 of this thesis). This last systematical error causes a common shift in all the point of the distribution, and does not contribute to the physical behavior of the Nuclear Transparency ratio (for this reason is not included with the other error).

Length range touched by this data-set. A χ^2 study on this result rejects the Glauber model calculation with a confidence level of 42% (Degree Of Freedom = 3). This value has been determined using a one sided confidence level (see equation 6.6). Tha Glauber prediction has been determined using experimental cross section and does not estimates any parameter from the Nuclear Transparency data determined in the EG2 experiment.

$$\chi^2 \text{ probability distribution with } k \text{ DOF} = f(\chi^2, k) = \frac{1}{2^{k/2}\,\Gamma(\frac{k}{2})} x^{\frac{k}{2}-1} \exp{(-\frac{\chi^2}{2})}$$

(6.5)

	Point to Point error (%)		
		Iron	Carbon
Q^2 bin	$5GeV$	$4GeV$	$5GeV$
1	0.5	0.3	0.5
2	0.3	-	-
3	-	0.3	0.1
4	0.1	-	-
5	0.1	-	-

Table 6.1: Acceptance correction ("bin migration" vs "one by one bin") : Point to Point systematic errors for different Q^2 bins, different targets and different beam energies

	Normalization error (%)		
	Iron		Carbon
	$5GeV$	$4GeV$	$5GeV$
All Q^2 bins	0.2	0.3	0.2

Table 6.2: Acceptance correction ("bin migration" vs "one by one bin"): Normalization systematic errors for different targets and different beam energies

$$C_{level} = \frac{\int_0^{\chi^2} f(\chi^2, k) \, d\chi^2}{\int_0^\infty f(\chi^2, k) \, d\chi^2} \tag{6.6}$$

- The result for Carbon at $5GeV$ (figure 6-9) shows also an increase in Nuclear Transparency with a parallel increase in Q^2. The FMS model predicts at this energy a separation between the expected values with a Glauber model and the ones expected with the implementation with Color Transparency. The data follows better the curve representing the FMS model with CT. It is important to enhance again the fact that the increase of the Nuclear Transparency with Q^2 cannot be explained with models with Glauber calculations (in this particular kinematical range). A χ^2 study on this result rejects the Glauber model calculation with a confidence level of 81% (DOF = 3).

Figure 6-8: The Nuclear Transparency ratio for Iron and Deuterium targets with beam energy of $4GeV$ is plotted here as a function of Q^2. Theoretical previsions with a model from L. Frankfurt, G.A. Miller, M. Strikman (FMS, see section 1.3.4 of this thesis) are also plotted to better interpret the data. The blue curve represents the theoretical prevision with a Glauber based model (NO CT). From this theory one is expected to see a more constant behavior with a variation in Q^2. If one adds to this model the properties of Color Transparency one obtains a dependence on the Nuclear Transparency ratio respects to Q^2 (red curve). The data for Iron at $4GeV$ shows an increase in Q^2 which cannot be interpret using a Glauber model. From the FMS model one does not expect in this kinematical region an important signal of Color Transparency. A χ^2 study in this result rejects the Glauber model calculation with a confidence level of 42%.

- The result for Iron at $5GeV$ (figure 6-12) is the one more significant, because it analyzes the target combination with the highest statistic (see table 2.3 at page 47). The difference respect to the expected behavior from a Glauber calculation is important. The curve obtained from the FMS model with Color Transparency effects follows the increase with Q^2 shown by the data. The slope for the higher Q^2 points well describe the behavior of the data, indicating that, in this range, the model well delineate the evolving in Q^2 of the conditions of the Point Like Configuration. The data presents consistently higher values for the part with higher Q^2 respect to the one predicted by
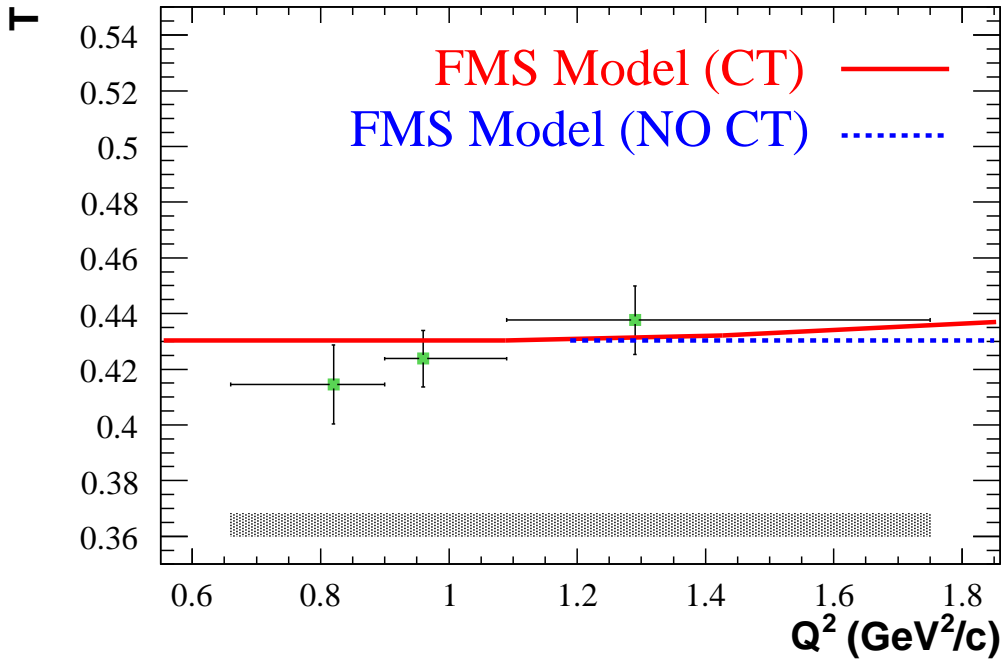
Figure 6-9: The Nuclear Transparency ratio for Carbon and Deuterium targets with beam energy of $5GeV$ is plotted here as a function of Q^2. Theoretical previsions with a model from L. Frankfurt, G.A. Miller, M. Strikman (FMS, see section 1.3.4 of this thesis) are also plotted to better interpret the data. The blue curve represents the theoretical prevision with a Glauber based model (NO CT). From this theory one is expected to see a more constant behavior with a variation in Q^2. If one adds to this model the properties of Color Transparency one obtains a dependence on the Nuclear Transparency ratio respects to Q^2 (red curve). The data for Carbon at $5GeV$ shows an increase in Q^2 which cannot be interpret using a Glauber model. A χ^2 study in this result rejects the Glauber model calculation with a confidence level of 81%.

the FMS model. A χ^2 study on this result rejects the Glauber model calculation with a confidence level of 94% (DOF = 5).

- The result with Carbon at $5GeV$ for the Nuclear Transparency as a function of Q^2 can be compared with the HERMES Nitrogen data (see figure 1-21 at page 29). In order to compare these two different data-sets we still need take into account the fact that the two experiments have different kinematical ranges. The result found for the slope of the Carbon data is $(0.039 \pm 0.017_{stat} \pm 0.034_{syst})GeV^{-2}$ (see figure 6-10) is consistent within the limited statistical precision with the slope found from the HERMES Nitrogen data, $(0.089 \pm 0.046 \pm 0.020)GeV^{-2}$. The result with Iron at
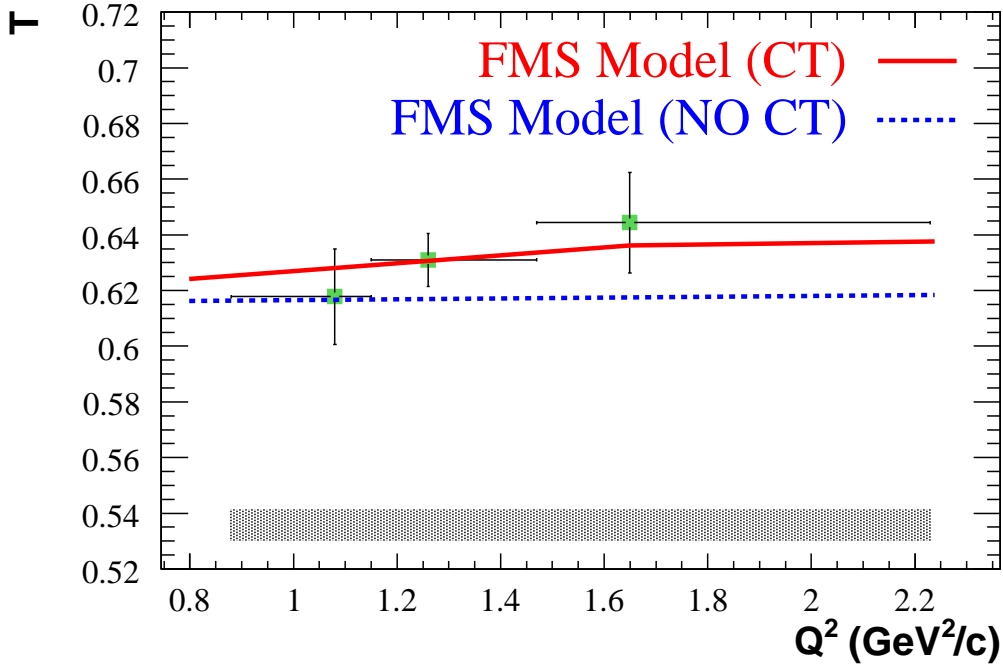
Figure 6-10: The Nuclear Transparency ratio for Carbon and Deuterium targets with beam energy of $5GeV$ is plotted here as a function of Q^2. The error bars in each point show the different contribution from statistical error (black) and systematic point to point error (red). The data is fitted with a linear function (black line). The result of the fit gives for the slope for the Nuclear Transparency as a function of Q^2 a value of $(0.039 \pm 0.017_{stat} \pm 0.034_{syst})GeV^{-2}$

$4GeV$ and $5GeV$ for the Nuclear Transparency dependence on Q^2 is a more precise measurement. This is consequence of the higher statistic obtained in this data-set. The value determined for the slope is $(0.0495 \pm 0.0069_{stat} \pm 0.0124_{syst})GeV^{-2}$ (see figure 6-11).

6.4 Conclusions

In this thesis we studied the onset of Color Transparency in ρ^0 electroproduction through different nuclei. The effects of Color Transparency were observed in the data obtained from different targets configuration. An increase in Q^2 of the measured Nuclear Transparency ratio cannot be interpreted, in the kinematical range of the EG2 experiment, with the hadron's picture of nuclear interaction with matter (Glauber model). To describe this behavior one needs to implement this model with effects from Quantum Chromodynamics.

Figure 6-11: The Nuclear Transparency ratio for Iron and Deuterium targets with beam energy of $4GeV$ (blue) and $5GeV$ (green) is plotted here as a function of Q^2. The error bars in each point show the different contribution from statistical error (black) and systematic point to point error (red). The data is fitted with a linear function (black line). The result of the fit gives for the slope for the Nuclear Transparency as a function of Q^2 a value of $(0.0495 \pm 0.0069_{stat} \pm 0.0124_{syst})GeV^{-2}$

This effects are important in correcting the hadron's picture also for the energies analyzed in this experiment. This was important to see, because the same effects were firstly predicted just at higher energies. At lower energies one cannot rely solely on perturbative Quantum Chromodynamics, but one needs to create models which extrapolate to this kinematical range the properties determined through perturbative QCD. For this reason an existing model [2], which gives good agreement also in similar experiments (see [15] and [14]), was used to test our results. The model well interprets the increase in Q^2 seen in our data.
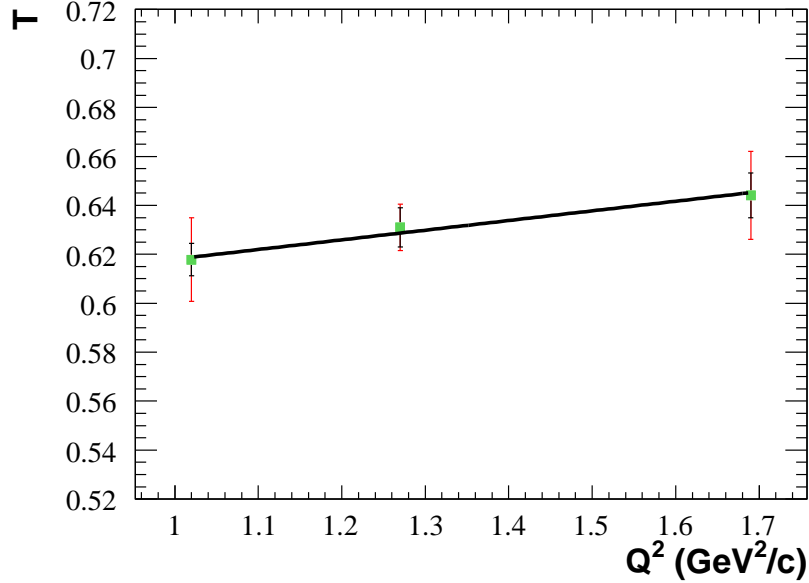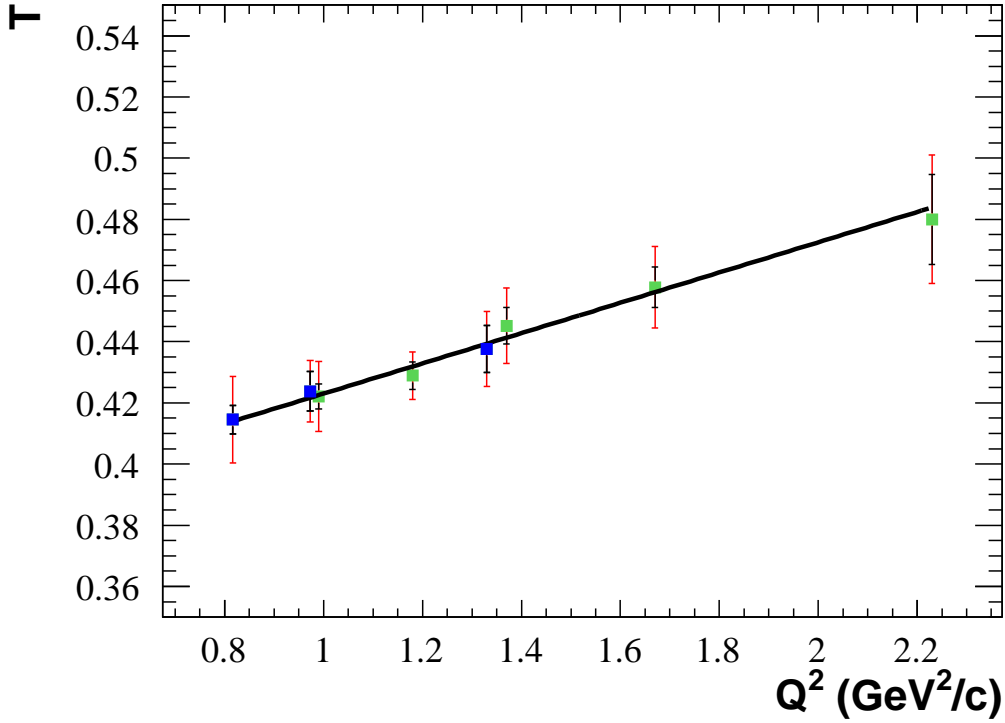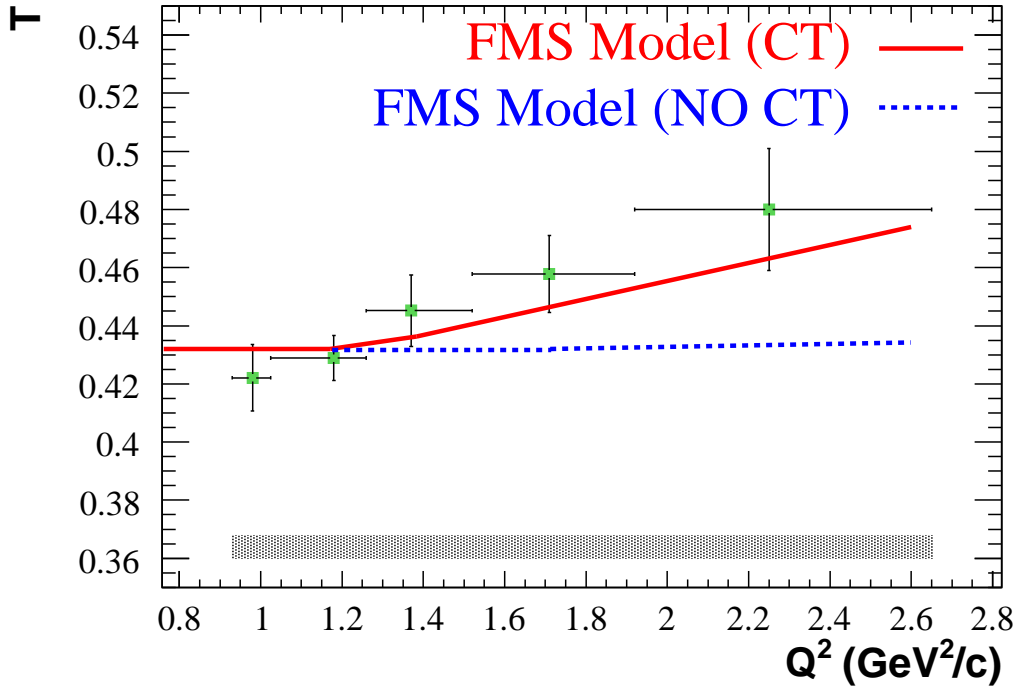
Figure 6-12: The Nuclear Transparency ratio for Iron and Deuterium targets with beam energy of $5GeV$ is plotted here as a function of Q^2. Theoretical previsions with a model from L. Frankfurt, G.A. Miller, M. Strikman (FMS, see section 1.3.4 of this thesis) are also plotted to better interpret the data. The blue curve represents the theoretical prevision with a Glauber based model (NO CT). From this theory one is expected to see a more constant behavior with a variation in Q^2. If one adds to this model the properties of Color Transparency one obtains a dependence on the Nuclear Transparency ratio respects to Q^2 (red curve). The data for Iron at $5GeV$ shows a consistent increase in Q^2 with a better statistical significance respect to the other configurations inspected in this experiment. This is due to the higher statistic available in this particular configuration. The difference respect to the expected behavior from a Glauber calculation is important. The data presents consistently higher values for the part with higher Q^2 respect to the one predicted by the FMS model. A χ^2 study in this result rejects the Glauber model calculation with a confidence level of 94%.

LIST OF REFERENCES

[1] L. ElFassi and al., "Search for the onset of color transparency via ρ^0 electroproduction off nuclei," clas analysis note, Thomas Jefferson Laboratory, December 2009.

[2] L. Frankfurt, G. A. Miller, and M. Strikman, "Color transparency in semi-inclusive electroproduction of ρ mesons," *Phys. Rev. C*, vol. 78, p. 015208, Jul 2008.

[3] A. Carroll, "Nuclear transparency to large-angle pp elastic scattering," *Phys. Rev. Lett.*, vol. 61, no. 15, p. 1698, 1988.

[4] I. Mardor and al., "Nuclear transparency in large momentum transfer quasielastic scattering," *Phys. Rev. Lett.*, vol. 81, no. 23, p. 5085, 1998.

[5] A. Leksanov, "Energy dependence of nuclear transparency in c(p,2p) scattering," *Phys. Rev. Lett.*, vol. 87, no. 21, p. 212301, 2001.

[6] J. Ralston and B. Pire, "Fluctuating proton size and oscillating color transparency," *Phys. Rev. Lett.*, vol. 61, no. 16, p. 1823, 1988.

[7] G. Garino, M. Saber, R. E. Segel, D. F. Geesaman, R. Gilman, M. C. Green, R. J. Holt, J. P. Schiffer, B. Zeidman, E. J. Beise, G. W. Dodson, S. Høibråten, L. D. Pham, R. P. Redwine, W. W. Sapp, C. F. Williamson, S. A. Wood, N. S. Chant, P. G. Roos, J. D. Silk, M. Deady, and X. K. Maruyama, "Proton propagation in nuclei studied in the (e,e'p) reaction," *Phys. Rev. C*, vol. 45, pp. 780–790, Feb 1992.

[8] N. C. R. Makins, R. Ent, M. S. Chapman, J.-O. Hansen, K. Lee, R. G. Milner, J. Nelson, R. G. Arnold, P. E. Bosted, C. E. Keppel, A. Lung, S. E. Rock, M. Spengos, Z. M. Szalata, L. H. Tao, J. L. White, K. P. Coulter, D. F. Geesaman, R. J. Holt, H. E. Jackson, V. Papavassiliou, D. H. Potterveld, B. Zeidman, J. Arrington, E. J. Beise, E. Belz, and B. W. Filippone, "Momentum transfer dependence of nuclear transparency from the quasielastic $c12$(e,e'p) reaction," *Phys. Rev. Lett.*, vol. 72, pp. 1986–1989, Mar 1994.

[9] T. G. O'Neill, W. Lorenzon, P. Anthony, R. G. Arnold, J. Arrington, E. J. Beise, J. E. Belz, P. E. Bosted, H. J. Bulten, M. S. Chapman, K. P. Coulter, F. Dietrich, R. Ent, M. Epstein, B. W. Filippone, H. Gao, R. A. Gearhart, D. F. Geesaman, J. O. Hansen, R. J. Holt, H. E. Jackson, C. E. Jones, C. E. Keppel, E. R. Kinney, S. Kuhn, K. Lee, A. Lung, N. C. R. Makins, D. J. Margaziotis, R. D. McKeown, R. G. Milner, B. Mueller, J. Napolitano, J. Nelson, V. Papavassiliou, G. G. Petratos, D. H. Potterveld, S. E. Rock, M. Spengos, Z. M. Szalata, L. H. Tao, K. van Bibber, J. F. J. van den Brand, J. L. White, and B. Zeidman, "A-dependence of nuclear transparency in quasielastic a(e, ef'p) at high 2," *Physics Lett. B*, vol. 351, no. 1-3, pp. 87–92, 1995.

[10] D. Abbott, A. Ahmidouch, T. A. Amatuni, C. Armstrong, J. Arrington, K. A. Assamagan, K. Bailey, O. K. Baker, S. Barrow, K. Beard, D. Beatty, S. Beedoe, E. Beise, E. Belz, C. Bochna, H. Breuer, E. E. W. Bruins, R. Carlini, J. Cha, N. Chant, C. Cothran, W. J. Cummings, S. Danagoulian, D. Day, D. DeSchepper, J.-E. Ducret, and F. Duncan, "Quasifree $(e, e'p)$ reactions and proton propagation in nuclei," *Phys. Rev. Lett.*, vol. 80, pp. 5072–5076, Jun 1998.

[11] K. Garrow, D. McKee, A. Ahmidouch, C. S. Armstrong, J. Arrington, R. Asaturyan, S. Avery, O. K. Baker, D. H. Beck, H. P. Blok, C. W. Bochna, W. Boeglin, P. Bosted, M. Bouwhuis, H. Breuer, D. S. Brown, A. Bruell, R. D. Carlini, N. S. Chant, A. Cochran, L. Cole, S. Danagoulian, D. B. Day, J. Dunne, D. Dutta, R. Ent, and H. C. Fenker, "Nuclear transparency from quasielastic $a(e, e'p)$ reactions up to $q2 = 8.1(gev/c)2$," *Phys. Rev. C*, vol. 66, p. 044613, Oct 2002.

[12] V. R. Pandharipande and S. C. Pieper, "Nuclear transparency to intermediate-energy nucleons from (e,e'p) reactions," *Phys. Rev. C*, vol. 45, pp. 791–798, Feb 1992.

[13] L. Frankfurt, W. Greenberg, and al., "Color transparency effects in electron deuteron interactions at intermediate q^2," *Z. Phys. A*, vol. 352, no. 1, pp. 97–113, 1995.

[14] D. Dutta, F. Xiong, L. Y. Zhu, J. Arrington, T. Averett, E. Beise, J. Calarco, T. Chang, J. P. Chen, E. Chudakov, M. Coman, B. Clasie, C. Crawford, S. Dieterich, F. Dohrmann, K. Fissum, S. Frullani, H. Gao, R. Gilman, C. Glashausser, J. Gomez, K. Hafidi, J.-O. Hansen, D. W. Higinbotham, R. J. Holt, C. W. de Jager, and X. Jiang, "Nuclear transparency with the $\gamma n \rightarrow \pi - p$ process in $4he$," *Phys. Rev. C*, vol. 68, p. 021001, Aug 2003.

[15] B. Clasie, X. Qian, J. Arrington, R. Asaturyan, F. Benmokhtar, W. Boeglin, P. Bosted, A. Bruell, M. E. Christy, E. Chudakov, W. Cosyn, M. M. Dalton, A. Daniel, D. Day, D. Dutta, L. El Fassi, R. Ent, H. C. Fenker, J. Ferrer, N. Fomin, H. Gao, K. Garrow, D. Gaskell, C. Gray, T. Horn, G. M. Huber, and M. K. Jones, "Measurement of nuclear transparency for the $a(e, e'\pi+)$ reaction," *Phys. Rev. Lett.*, vol. 99, p. 242502, Dec 2007.

[16] M. R. Adams, S. Aïd, P. L. Anthony, D. A. Averill, M. D. Baker, B. R. Baller, A. Banerjee, A. A. Bhatti, U. Bratzler, H. M. Braun, H. Breidung, W. Busza, T. J. Carroll, H. L. Clark, J. M. Conrad, R. Davisson, I. Derado, S. K. Dhawan, F. S. Dietrich, W. Dougherty, T. Dreyer, V. Eckardt, U. Ecker, M. Erdmann, F. Faller, G. Y. Fang, and J. Figiel, "Measurement of nuclear transparencies from exclusive ρ meson production in muon-nucleus scattering at 470 gev," *Phys. Rev. Lett.*, vol. 74, pp. 1525–1529, Feb 1995.

[17] J. Hufner, B. Kopeliovich, and J. Nemchick, "Glauber multiple scattering theory for photoproduction of vector mesons off nuclei and the role of the coherence length," *airXiv:nucl-th/9605007v1*, 1996.

[18] G. McClellan, N. Mistry, P. Mostek, H. Ogren, A. Osborne, A. Silverman, J. Swartz, R. Talman, and G. Diambrini-Palazzi, "Incoherent photoproduction of ρ mesons from complex nuclei and comparison with vector-dominance predictions," *Phys. Rev. Lett.*, vol. 23, pp. 554–556, Sep 1969.

[19] A. Airapetian, N. Akopov, Z. Akopov, M. Amarian, V. V. Ammosov, A. Andrus, E. C. Aschenauer, W. Augustyniak, R. Avakian, A. Avetissian, E. Avetissian, P. Bailey, V. Baturin, C. Baumgarten, M. Beckmann, S. Belostotski, S. Bernreuther, N. Bianchi, H. P. Blok, H. Böttcher, A. Borissov, M. Bouwhuis, J. Brack, A. Brüll, I. Brunn, G. P. Capitani, and H. C. Chiang, "$q2$ dependence of nuclear transparency for exclusive ρ production," *Phys. Rev. Lett.*, vol. 90, p. 052501, Feb 2003.

[20] J. J. Sakurai, "Vector-meson dominance and high-energy electron-proton inelastic scattering," *Phys. Rev. Lett.*, vol. 22, pp. 981–984, May 1969.

[21] T. H. Bauer, R. D. Spital, D. R. Yennie, and F. M. Pipkin, "The hadronic properties of the photon in high-energy interactions," *Rev. Mod. Phys.*, vol. 50, pp. 261–436, Apr 1978.

[22] P. Dirac, "Quantum theory of localizable dynamical systems," *Phys. Rev.*, vol. 73, no. 9, 1948.

[23] J. Kogut and D. Soper, "Quantum electrodynamics in the infinite-momentum frame," *Phys. Rev. D*, vol. 1, no. 10, 1970.

[24] P. Jain, B. Pire, and J. Ralston, "Quantum color transparency and nuclear filtering," tech. rep., Elsevier Science, 1995.

[25] R. Glauber, *High-energy collision theory*, vol. 1 of *Lectures in Theoretical Physics*. Interscience publishers, Inc., New York, 1959. edited by W.E. Brittin, L.G. Dunham.

[26] G. Lepage and S. Brodsky, "Exclusive processes in perturbative quantum chromodynamics," *Phys. Rev. D*, vol. 22, no. 9, p. 2158, 1980.

[27] J. P. Ralston and B. Pire, "Quantum color transparency," *Phys. Rev. Lett.*, vol. 65, pp. 2343–2346, Nov 1990.

[28] E. Feinberg and I. Pomeranchuk, "Suppl. 3," *Nuovo Cimento*, 1956.

[29] M. L. Good and W. D. Walker, "Diffraction dissociation of beam particles," *Phys. Rev.*, vol. 120, pp. 1857–1860, 1960.

[30] B. Kopeliovich and B. Zakharov, "Quantum effects and color transparency in charmonium photoproduction on nuclei," *Phys. Rev. D*, vol. 44, no. 11, 1991.

[31] B. Kopeliovic and J. Nemchick, "Where is the baseline for color transparency studies with moderate energy electron beams," *airXiv:nucl-th/9511018v2*, 1995.

[32] B. Kopeliovich, J. Nemchik, A. Schafer, and A. Tarasov, "Color transparency versus quantum coherence in electroproduction of vector mesons off nuclei," *Phys. Rev. C*, vol. 65, 2002.

[33] B. Kopeliovich, J. Nemchik, and I. Schmidt, "Color transparency at low energies prediction for jlab," *arXiv:hep-ph/0702272v2*, 2007.

[34] R. Feynman and A. Hibbs, *Quantum Mechanics and Path Integrals*. McGraw-Hill, 1965.

[35] P. Landshoff and D. Pritchard *Z. Physik C, Particles and Fields*, vol. 6, p. 69, 1980.

[36] E. M. Aitala, S. Amato, J. C. Anjos, J. A. Appel, D. Ashery, S. Banerjee, I. Bediaga, G. Blaylock, S. B. Bracker, P. R. Burchat, R. A. Burnstein, T. Carter, H. S. Carvalho, N. K. Copty, L. M. Cremaldi, C. Darling, K. Denisenko, S. Devmal, A. Fernandez, G. F. Fox, P. Gagnon, S. Gerzon, C. Gobel, K. Gounder, A. M. Halling, G. Herrera, and G. Hurvits, "Observation of color-transparency in diffractive dissociation of pions," *Phys. Rev. Lett.*, vol. 86, pp. 4773–4777, May 2001.

[37] K. Ackerstaff and H. collaboration, "Oervation of a coherence lenght effect in exclusive ρ^0 electroproduction," *Phys. Rev. Lett.*, vol. 82, no. 15, p. 3025, 1999.

[38] C. Leemann, D. Douglas, and G. Krafft, "The continuous electron beam accelerator facility: Cebaf at the jefferson laboratory," *Annu. Rev. Nucl. Part. Sci.*, 2001.

[39] M. Mestayer and al., "The clas drift chambers system," *Nucl. Instrum. Meth. A*, vol. 449, p. 81, 2000.

[40] M. Mestayer and S. Morrow, "Drift chambers alignemnt. technical report," tech. rep., Thomas Jefferson Laboratory CLAS-NOTE 2002-10, 2002.

[41] M. Amarian and al., "The clas forward electromagnetic calorimeter," *Nucl. Instrum. Meth. A*, vol. 460, p. 239, 2001.

[42] M. Aghinolfi and al., "Response to cosmic rays of the large-angle electromagnetic shower calorimeter of the clas detector," *Nucl. Instrum. Meth. A*, vol. 447, p. 424, 2000.

[43] G. Adams and al., "The clas cherenkov detector," *Nucl. Instrum. Meth. A*, vol. 465, p. 414, 2001.

[44] E. Smith and al., "The time-of-flight system for clas," *Nucl. Instrum. Meth. A*, vol. 432, p. 265, 1999.

[45] K. Hafidi, M. Holtrop, *et al.*, "q^2 dependence of nuclear transparency for incoherent ρ^0 electroproduction." Supported by the CLAS collaboration, May 25, 2002.

[46] W. Brooks, "Quark propagation through cold qcd matter." Supported by the CLAS collaboration, May 25, 2002.

[47] M. Battaglieri, R. Devita, and M. Ripani, "Private communication." INFN Genova, 2003.

[48] D. Cassel, "Exclusive ρ^0, ω, and ϕ electroproduction," *Phys. Rev. D*, vol. 24, no. 11, 1981.

[49] H. Hakobyan, "A double-target system for precision measurements of nuclear medium effects," *Nuclear Instruments and Methods in Physics Research Section A: Accelerators, Spectrometers, Detectors and Associated Equipment*, vol. 592, no. 3, 2008.

[50] H. Hakobyan, "The clas/eg2 target implementation in gsim," Tech. Rep. 002, Thomas Jefferson Laboratory, 2008.

[51] M. Ungaro and J. Li, "Procedure for drift chamber inefficiencies," tech. rep., CLAS-NOTE, April 2003.

[52] K. Schilling, "How to analyze vector-meson production in inelastic lepton scattering," *Nuclear Physics B*, vol. 61, 1973.

[53] L. Mo and Y. Tsai, "Radiative corrections to elastic and inelastic ep and up scattering," *Rev. Mod. Phys.*, vol. 41, pp. 205–235, Jan 1969.

[54] I. Akushevich, "Radiative effects in processes of diffractive vector meson electroproduction," *Eur.Phys.J.*, vol. C8, no. 3, pp. 457–463, 1999.

[55] X. Zheng, "Cryogenic target thickness study for eg2." http://www.jlab.org/~xiaochao/eg2/eg2targ.pdf, 2003.

132